Titre: Title:	Development of a System for the Refactive Index Profiling of Laser Written Waveguides to Better Understand Laser Induced Material Modification
Auteur: Author:	Antoine Drouin
Date:	2019
Type:	Mémoire ou thèse / Dissertation or Thesis
Référence: Citation:	Drouin, A. (2019). Development of a System for the Refactive Index Profiling of Laser Written Waveguides to Better Understand Laser Induced Material Modification [Mémoire de maîtrise, Polytechnique Montréal]. PolyPublie. https://publications.polymtl.ca/3837/

URL de PolyPublie: PolyPublie URL:	https://publications.polymtl.ca/3837/
Directeurs de recherche: Advisors:	Raman Kashyap
Programme: Program:	Génie physique

POLYTECHNIQUE MONTRÉAL
affiliée à l'Université de Montréal

Development of a system for the refactive index profiling of laser written waveguides to better understand laser induced material modification

ANTOINE DROUIN
Département de génie physique

Mémoire présenté en vue de l'obtention du diplôme de *Maîtrise ès sciences appliquées*
Génie physique
Avril 2019

POLYTECHNIQUE MONTRÉAL
affiliée à l'Université de Montréal

Ce mémoire intitulé :

Development of a system for the refactive index profiling of laser written waveguides to better understand laser induced material modification

présenté par **Antoine DROUIN**
en vue de l'obtention du diplôme de *Maîtrise ès sciences appliquées*
a été dûment accepté par le jury d'examen constitué de :

Yves-Alain PETER, président
Raman KASHYAP, membre et directeur de recherche
Xavier DAXHELET, membre externe

ACKNOWLEDGEMENTS

First, I would like to thank Raman Kashyap for giving me the opportunity to work on many projects throughout my master's, discover the world of scientific research and aqcuire a considerable amount of experience and skills in engineering.

I would also like to thank my colleagues: Sébastier Loranger for his constant help and advice; Jean-Sébastien Boisvert for introducing me to the subject of laser writing; Victor Lambin Iezzi for his help with 3D printing; Pierre Lorre and Frédéric Monet.

I also wish to thank our dedicated technicians: Jules Gauthier, Steve Dubé, Jean-Sébastien Décarie and Mikaël Leduc.

RÉSUMÉ

La modification de matériaux transparents par écriture laser a été utilisée au fil des années comme méthode pour produire des guides d'onde dans des matériaux transparents. Plus récemment, l'écriture directe par laser a été utilisée dans la production de dispositifs photoniques et senseurs dans les écrans de téléphones intelligents. Par contre, la caractérisation de la modification matérielle (principalement le changement d'indice de réfraction) produite par écriture laser est restée problématique. Les méthodes typiquement utilisées pour les fibres optiques ne sont pas appliquables directement ou sont très peu pratiques.

Un système pour la mesure de profils d'indice de réfraction de fibres optiques et de modifications matérielles telles que des guides d'onde et réseaux diffractifs est présenté dans ce mémoire. Un interféromètre de type Mach-Zehnder est utilisé pour obtenir le décalage de phase d'un faisceau de lumière se propageant perpendiculairement à la fibre optique ou au guide d'onde. Des algorithmes de PSI (*Phase Shifting Interferometry*) sont utilisés en parallèle à un actionneur piézoélectrique continuellement en mouvement pour déduire le décalage de phase des franges d'interférence, permettant d'obtenir des images de phase quantitatives à un taux de plus de 100 images par seconde avec une résolution inférieure à un micromètre. Différentes techniques sont utilisées pour déduire le profil d'indice de réfraction du décalage de phase mesuré: la transformée d'Abel inverse applicable aux fibres optiques et guides d'onde axiallement symmétriques, l'imagerie tomographique pour les fibres optiques axiallement asymmétriques et une méthode de reconstruction novatrice basée sur un processus d'optimisation par l'utilisation d'un algorithme génétique pour les guides d'onde axiallement asymmétriques écrits dans le verre. La précision de la reconstruction du profil d'indice de réfraction se situe entre $\pm 1 \cdot 10^{-4}$ et $\pm 3 \cdot 10^{-4}$ RIU dépendamment de la méthode utilisée et de l'échantillon étudié. La méthode permet d'effectuer la mesure en quelques secondes avec peu de préparation d'échantillon pour les fibres optiques et aucune préparation pour les guides d'onde écrits par laser. L'intégration des multiples actionneur du système à un logiciel de contrôle permet la mesure rapide d'échantillons contenant des centaines de guides d'onde écrits par laser.

Le sujet de l'écriture directe par laser dans le verre trempé Gorilla fait par Corning est aussi abordé dans ce mémoire. Une étude systématique du rôle de plusieurs paramètres de l'écriture par laser ainsi que les avancements dans la production de guides d'onde intéressants résultant de cette étude sont tout d'abord présentés. Des guides d'onde presque parfaitement circulaires et insensibles en polarisation sont écrits directement dans le verre trempé en utilisant des objectifs à haute ouverture numérique. Le processus d'optimisation du paramètre le plus important en écriture par laser, la vitesse d'écriture, par l'utilisation du système de mesure de profils d'indice de réfraction est aussi présenté. Finalement, l'écriture directe de réseaux diffractifs par l'utilisation de paramètres d'écriture complètement différents basée sur l'intensification de l'effet de défocalisation à l'interface entre l'air et le verre par l'utilisation d'objectifs à basse ouverture numérique et d'un verre à haut indice de réfraction est décrite. Des réseaux diffractifs à période aussi courte que 1 μm et modulation d'indice de réfraction atteignant $3.2 \cdot 10^{-3}$ RIU ont été écrits avec succès. L'utilisation du système de mesure de profils d'indice de réfraction pour la mesure de la modulation d'indice de réfraction des réseaux diffractifs écrits par laser est aussi présentée.

Le travail présenté dans ce mémoire permet l'analyse rapide de modifications matérielles produites par écriture laser dans des matériaux transparents et devrait accélérer le développement de dispositifs et senseurs écrits directement dans des matériaux transparents ainsi qu'approfondir la compréhension des processus d'intéraction entre les impulsions laser ultra brèves et la matière.

ABSTRACT

Laser induced material modification has gathered interest over the years as a method to produce waveguides in solid transparent media. More recently, direct laser writing showed promise in producing photonic devices and sensors in smartphone screens. However, characterizing the material modification — mainly the refractive index change — induced by laser writing has remained problematic. Methods typically used for optical fibers are either not directly applicable or unpractical.

A system for the measurement of the refractive index profile of optical fibers and laser induced material modifications including waveguides and gratings is presented in this thesis. A Mach-Zehnder interferometer is used to obtain the phase shift of light propagating transversely through the optical fiber or waveguide. Phase shifting interferometry algorithms are used in conjunction with a continuously moving piezoelectric actuator to quickly recover phase data from fringe patterns, providing quantitative phase images at a rate of up to over 100 frames per second with sub-micron resolution. Different techniques are used to recover the refractive index profile from the measured phase shift: the inverse Abel transform applicable to axially symmetric optical fibers and waveguides, tomographic imaging for axially asymmetric optical fibers and a novel genetic algorithm based reconstruction method for axially asymmetric waveguides written directly in glass. The precision of the reconstruction process is between $\pm 1 \cdot 10^{-4}$ and $\pm 3 \cdot 10^{-4}$ RIU depending on the method used and sample studied. The method allows for measurements to be done in mere seconds with little sample preparation in the case of optical fibers and without any sample preparation for laser written waveguides. The integration of the system's multiple actuators to a single software allows for the rapid measurement of glass samples containing hundreds of laser written waveguides.

The subject of direct laser writing in Corning's Gorilla toughened glass is also covered in this thesis. A systematic study of the role of many experimental parameters in laser writing and the advancements in producing interesting waveguides resulting from the study are first presented. Almost prefectly circular and polarization insensitive waveguides are written in toughened glass by using objectives with high numerical aperture. The optimization process of the most important parameter in laser writing, the writing speed, using the refractive index profiling system is also presented. Finally, direct laser writing of gratings is achieved using a completely different set of parameters based on the intensification of the defocusing effect at the air-glass interface by writing in high refractive index glass and using objectives with lower numerical apertures. Gratings with periods as short as 1 μm and refractive index modulation of $3.2 \cdot 10^{-3}$ RIU have been successfully written. The use of the refractive index profiling system to measure the refractive index modulation of the laser written gratings is also presented.

The work presented in this thesis allows for the fast analysis of laser induced modification of transparent materials and should accelerate the development of devices and sensors written directly in transparent materials as well as improve the understanding of fs laser writing processes.

TABLE OF CONTENTS

LIST OF TABLES

LIST OF FIGURES

LIST OF APPENDICES

CHAPTER 1 INTRODUCTION

Laser induced material modification has been used increasingly over the last decade to produce waveguides usually part of larger structures such as couplers and interferometers making up various devices and sensors. For example, amplifiers [1,2], laser oscillators [1], liquid's refractive index sensors [3], temperature sensors [4,5], few photon quantum circuits capable of creating entangled photonic states [6] and optical oracles for NP-complete problems resolution [7] have all been directly written in glass. Compared to standard lithography techniques, direct ultrafast laser writing of waveguides is fast, cheap and not limited to 2D structures, allowing for far greater circuit topologies. Another important advantage of the technique is its ability to produce a transparent device. This possibility has gathered interest from scientists and engineers looking at the implementation of devices and sensors directly inside screens, most notably smartphone screens. [4,8]

Although the field of direct laser writing of waveguides has seen quite a lot of advances since its first demonstration in 1996 by Davis et al. [9], little has been done to characterize these laser written waveguides by measuring their refractive index change profile. Given that the resulting material modification depends on a plethora of experimental parameters, finding a viable set of parameters compatible with the glass type used and optimizing has more closely resembled guesswork. Most scientists either resort to measuring only an average refractive index change for the whole modified region, resort to inadequate approximations or infer the refractive index profile from other observations such as cross-sectional imaging or near-field analysis. The lack of a method to rapidly measure a refractive index profile has been of no help in trying to better understand the nature of these laser induced material modifications. The subject of this thesis is the development of a system that allows the measurement of refractive index profiles of ultrafast laser written waveguides.

1.1 Objectives

The main objective of the thesis is to develop a system incorporating current methods for refractive index profiling of optical fibers and a new approach for the measurement on laser written waveguides. The compatibility of the system to optical fibers should allow the study of laser induced modifications of optical fibers such as fiber Bragg gratings. A side goal to this objective is to streamline the measurement process to allow for a fast and systematic measurement of most laser induced material modifications.

Another objective to the thesis is to use the refractive index profiling system to better understand and optimize the waveguide writing process in toughened glass, a glass type often seen in smartphone screens. The enhancement to the characteristics of these waveguides should enhance the ability to write functional devices in smartphone screens.

1.2 Organisation of the thesis

A detailed literature review is first presented to cover the theoritical background necessary for the understanding of the thesis. The basis of guided optics describing the behaviour of light inside waveguides and interferometry which plays a central role in refractive index profiling are explained, followed by a review of the standard methods to measure refractive index profiles of optical fibers as well as current ways to estimate the laser induced refractive index change of laser written waveguides. Finally, the state of the art regarding the ultrafast laser writing techniques is detailed.

After this literature review, the system for measurements of refractive index profiles developed during my master's is described. The experimental method and results for optical fibers are presented. The applicability of the system to laser written waveguides by a new approach is presented in the following chapter as an article published in *Optics Express* in 2019.

The next chapter covers an exhaustive summary of the study of direct laser writing in toughened glasses made throughout my master's. The effects of many experimental parameters on the resulting material modification are described. The optimization of some experimental parameters using the system for refractive index profiling to produce an optimized waveguide is also presented.

As a conclusion, a review of the main results is presented as well as various recommendation for the improvement of the presented system.

CHAPTER 2 LITERATURE REVIEW

In this chapter, a comprehensive literature review on the topics essential to the understanding of the thesis is presented. The subject of guided wave optics describing the propagation of light in optical structures is first presented, followed by a review of the methods for producing these guided optical structures using laser writing. Because of its widespread use in refractive index profiling, the basic principles of interferometry are then presented. Since the main subject of this thesis is refractive index profiling, the literature review focuses on the state of the art of this subject in the last section, both for optical fibers and laser written waveguides.

2.1 Theory of guided optics

No discussion on the theory of guided optics can avoid starting by a review of the total internal reflection phenomenon, which in turn cannot be described without understanding of the refraction of a wave at the interface between two media with different propagation speeds. Refraction occurs for all types of waves such as water waves, sound pressure waves or electromagnetic waves. Figure 2.1 illustrates the phenomenon. As the wavefront propagates more slowly in the bottom material, the wavelength gets shorter. Since the material — or field — in which the wave propagates cannot be discontinuous, even at the interface, the wavefront must be deviated.

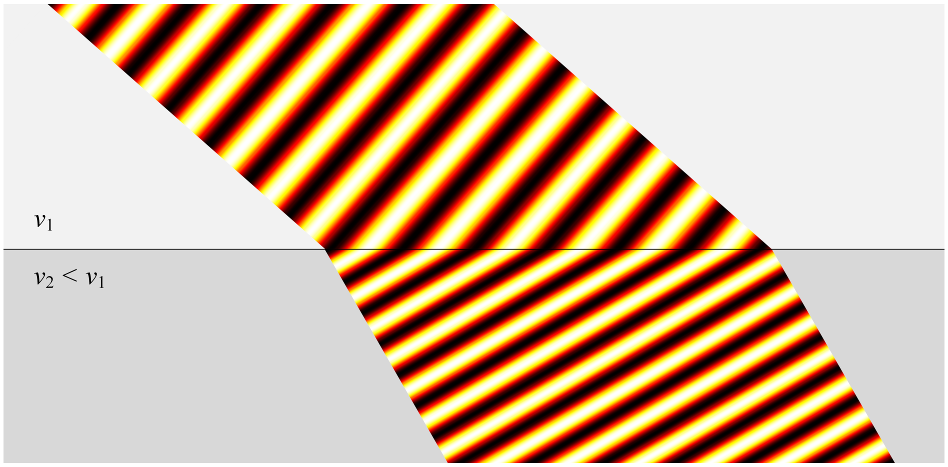

Figure 2.1 Illustration of the deviation of a wavefront at the interface between two materials with different propagation speeds (refraction).

In its simplest form, refraction of a light beam is described by Snell's law:

$$n_1 \sin\theta_1 = n_2 \sin\theta_2 \tag{2.1}$$

where n_i are the refactive indices and θ_i the entry and exit angles relative to the interface's normal. It basically states that a beam of light is refracted away from the interface's normal as it goes into a material of lower refractive index, and vice versa (see Figure 2.2(a)). The phenomenon of total internal reflection occurs when light traveling inside a medium of refractive index n_2 reaches the interface to another medium of refractive index $n_1 < n_2$ at an angle such that the refraction angle is greater than 90°. In this case, light is simply reflected (see Figures 2.2(b) and (c)). One can define a critical angle θ_c at which total internal reflection starts to occur:

$$\theta_c = \arcsin\left(\frac{n_2}{n_1}\right). \tag{2.2}$$

Now, imagine a cylinder of refractive index n_2 surrounded by a vast region of refractive index n_1 such as depicted in Figure 2.3. If a beam of light is sent along the cylinder such that the angles it makes at the interface between the materials of refractive indices n_1 and n_2 is larger than the critical angle, then the beam is reflected indefinetely and is thus confined inside the cylinder or as one might say, guided by the cylinder of refractive index n_2. This is the basic working principle of optical fibers. The beams for which the critical angle condition is respected — and thus for which guiding will occur — form a cone, usually called acceptance cone, of half-angle θ_a. The numerical aperture defined as $\mathrm{NA} = \sin\theta_a$ quantifies the extent

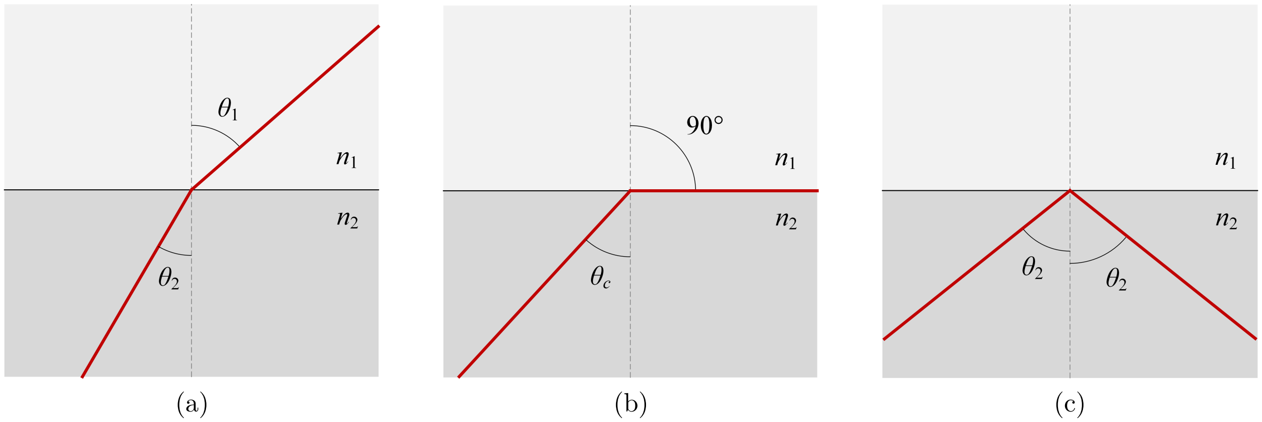

Figure 2.2 (a) Refracted ray. (b) Critical angle above which total internal reflection occurs. (c) Total internal reflection. Ray trajectories are valid regardless of propagation direction.

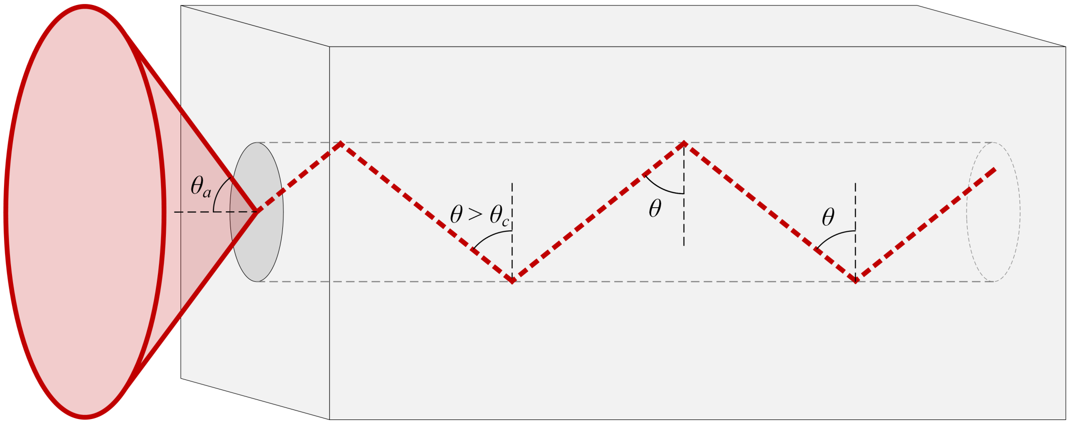

Figure 2.3 Schematic of a waveguide.

of the acceptance cone. By simple geometric considerations, one can show that

$$\mathrm{NA} = \sqrt{n_2^2 - n_1^2} \tag{2.3}$$

and thus that the angular extent of the acceptance cone is solely determined by the difference in refractive indices of the two materials. The refractive index profile of an optical fiber made up of two refractive index levels such as the one described so far is said to be step-index. The central region where light is guided is called the core with refractive index n_{core} while the surrounding region is called the cladding with refractive index n_{clad}. Although such fibers are very common, many other fibers make use of more exotic refractive index profiles to achieve different characteristics out of the scope of this text. Figure 2.4 shows a few refractive index profiles used in optical fibers.

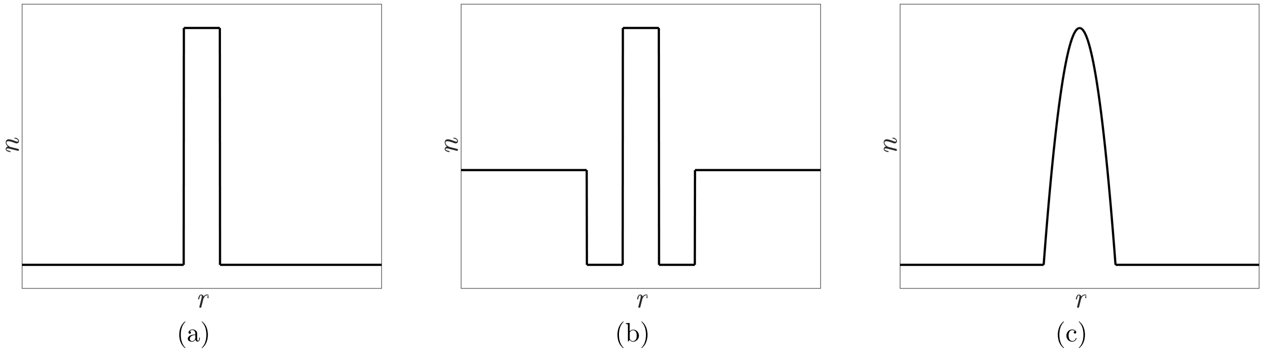

(a)

(b)

(c)

Figure 2.4 (a) Step-index profile. (b) Double-clad profile of dispersion-compensating fibers. (c) Graded-index profile.

To truly understand what dictates the characteristics of a waveguide other than its numerical aperture, one must consider the wave nature of light. As the electric field at the waveguide's entry is arbitrarily excited by, for example, injecting a beam at an angle and off-center, it will propagate in a complicated way and the light intensity distribution inside the waveguide will change along its propagation axis. For any type of waveguide, there exist specific electric field distributions that will propagate through it without changing. These are called the waveguide modes. Under the condition that the waveguide has an axially symmetric step-index profile with a small refractive index difference, then the resolution of Maxwell's equation is greatly simplified and analytical solutions for the linearly polarized (LP) modes supported by the waveguide can be found. A few of these LP modes are shown in Figure 2.5. The number of modes an optical fiber supports is dictated by its V-parameter calculated from

$$V = \frac{2\pi a}{\lambda}\mathrm{NA} \tag{2.4}$$

where a is the radius of the fiber's core and λ the excitation wavelength. The higher the value for V, the more modes the fiber supports. As long as $V < 2.405$, only the fundamental LP_{01} mode is supported and the fiber is said to be single-mode. Table 2.1 presents the cutoff value for some LP modes, under which the mode is not supported. There are reasons to design an optical fiber to be multi-mode such as requiring a higher bandwidth but there are also drawbacks to using such a fiber, mainly modal dispersion caused by the different propagation speeds of different modes.

In the general case where the step-index and small index difference conditions are not respected, the wave equation cannot be simplified in the same way and analytical solutions cannot be found. Still, whether a waveguide supports one, two or many modes, exactly what those modes are and how the power is distributed amongst them depends entirely on its refractive index profile, highlighting again that it is a quantity of high interest. Predicting the behaviour of light inside a waveguide with a complex refactive index profile — and thus its characteristics — goes far beyond the simple geometric and modal approach presented here. It requires the resolution of complex differential equations and is usually approached numerically using dedicated software. Figure 2.6 shows the computed mode profiles of a rib waveguide. Although these solutions to the wave equation are more complex than for step-index optical fibers, the same physical principles apply. For example, the waveguide with the larger refractive index difference (Figures 2.6(a) and (b)) confines light more tightly whereas a smaller refractive index difference (Figures 2.6(c) and (d)) allows more light to leak.

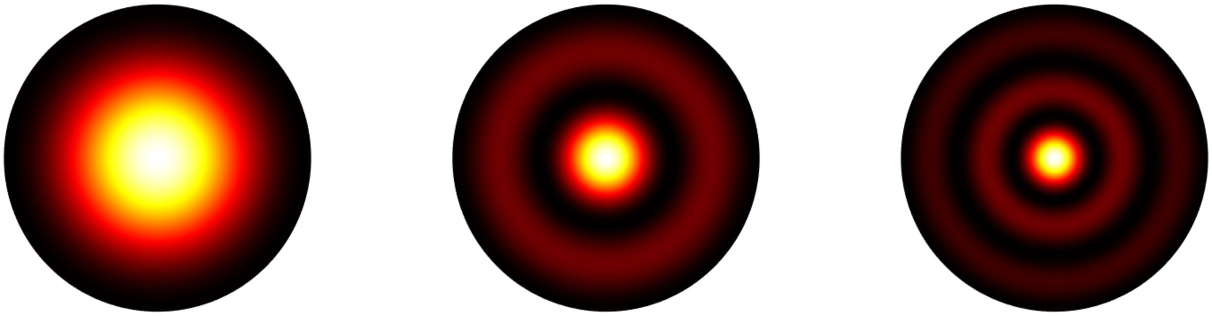

(a) LP_{01} (b) LP_{02} (c) LP_{03}

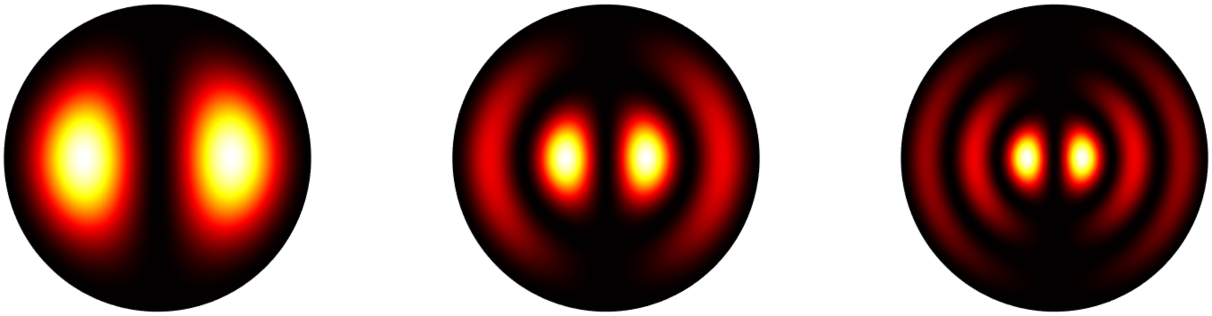

(d) LP_{11} (e) LP_{12} (f) LP_{13}

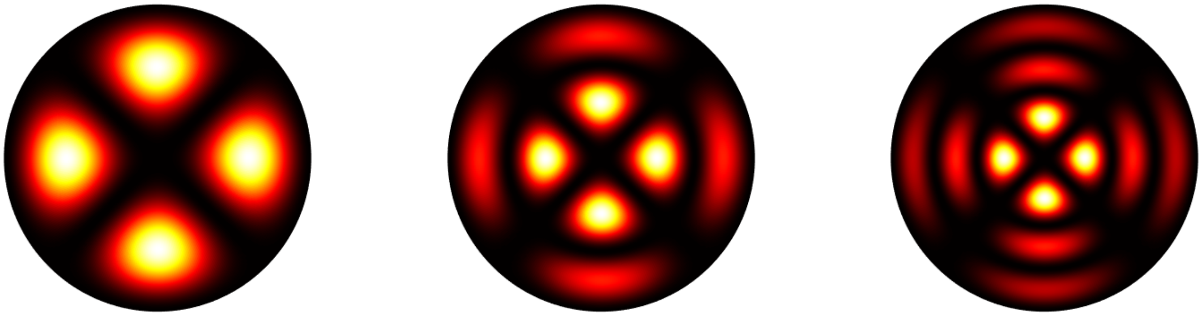

(g) LP_{21} (h) LP_{22} (i) LP_{23}

Figure 2.5 Light intensity of some LP_{lm} modes of step-index optical fibers.

Table 2.1 V-parameter cutoff values for some LP modes.

	LP_{01}	LP_{11}	LP_{21}	LP_{02}	LP_{31}	LP_{12}	LP_{41}	LP_{22}	LP_{03}	LP_{51}
V	-	2.405	3.832	3.832	5.136	5.520	6.380	7.016	7.016	7.558

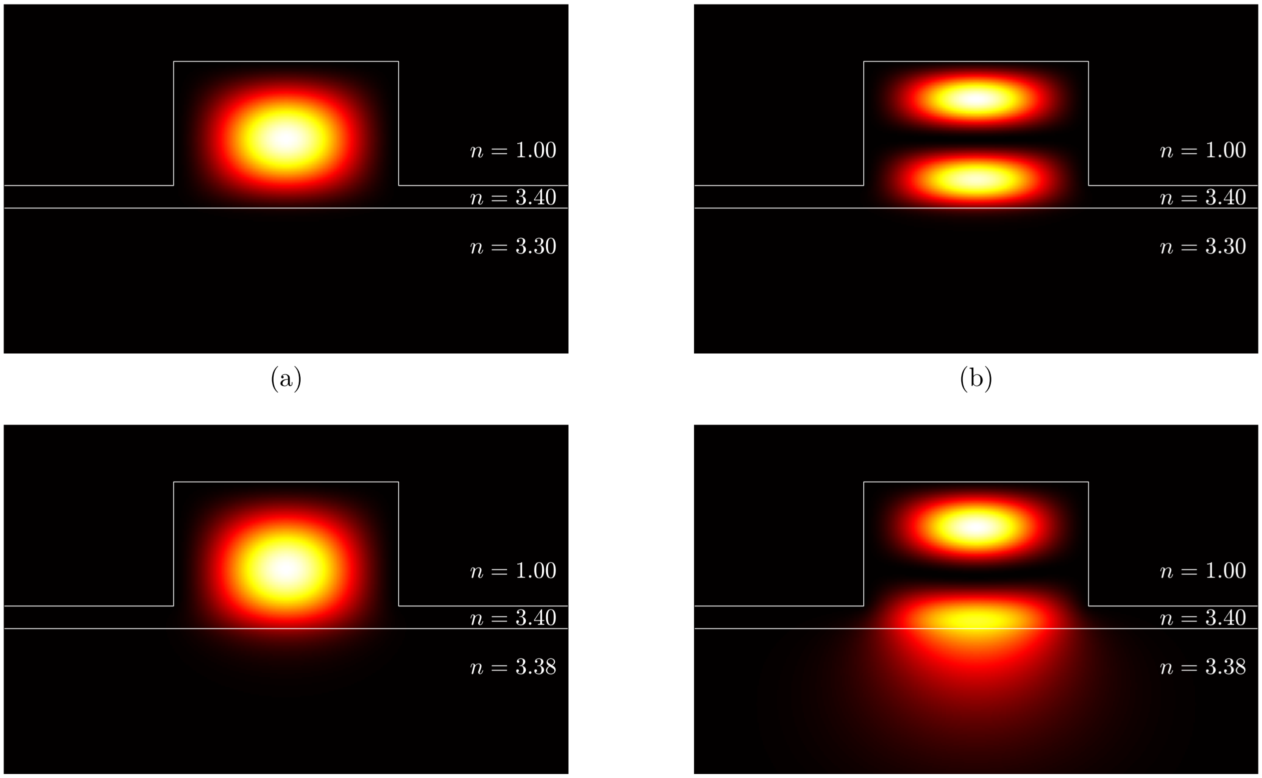

(a) (b) (c) (d)

Figure 2.6 (a) Fundemental mode of a rib waveguide with $\Delta n = 0.1$. (b) Second mode of a rib waveguide with $\Delta n = 0.1$. (c) Fundamental mode of a rib waveguide with $\Delta n = 0.02$. (d) Second mode of a rib waveguide with $\Delta n = 0.02$.

2.2 Direct laser writing of waveguides

Laser written waveguides are produced by focusing a high intensity pulsed laser beam inside a moving sample such as depicted in Figure 2.7(a). While the material is usually transparent at the laser's wavelength, the extreme intensity at the focal spot is such that nonlinear light-matter interactions occur, resulting in absorption and thus in a localized modification of the material. Ideally, the material modification would result in a smooth positive index change and the cylindrical modified region would act as a waveguide. In practice, only a limited set of experimental parameters results in a useful refractive index change profile. Figure 2.7(b) shows a few examples of laser induced material modifications. The nonlinear mechanisms resulting in absorption will first be presented, followed by a review of the writing parameters dictating the resulting material modification.

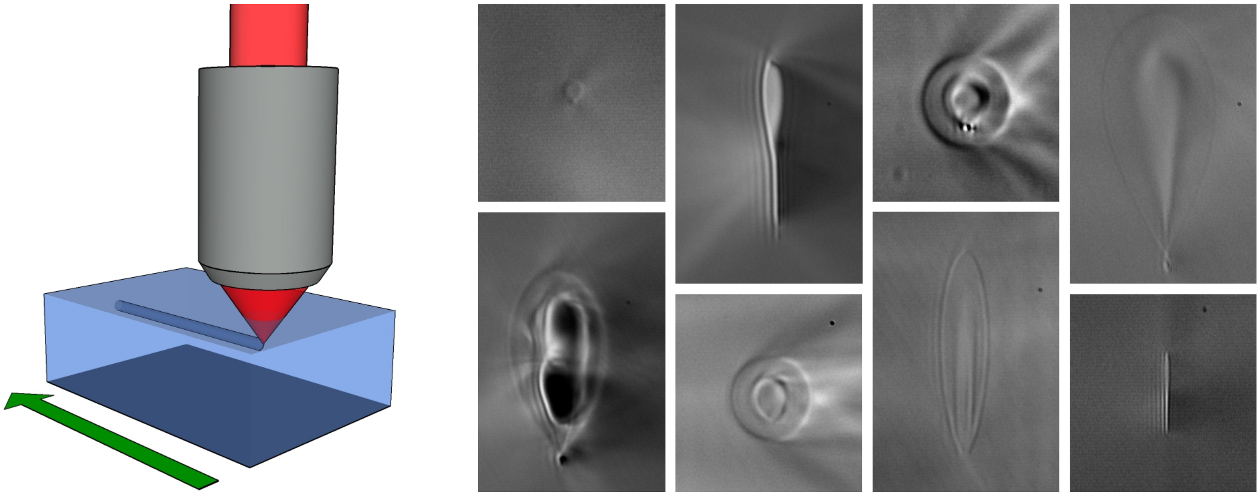

(a) (b)

Figure 2.7 (a) Representation of direct laser writing. (b) A few examples of laser induced material modifications.

2.2.1 Nonlinear electronic ionization

There are three main nonlinear processes by which a material can absorb light to which it is usually transparent: multiphoton ionization, tunnel ionization and avalanche ionization. The three processes are all usually occuring in laser writing albeit in different proportions depending on experimental parameters and more importantly, on the type of glass used. Plenty of theoritical physicists have developed physical models of these processes over the years, mainly to evaluate the free electron density from the wavelength, the electric field amplitude, the material band gap, etc. As there are no model accurately describing the change in refractive index caused by the material modification from the free electron density, these models are of no particular interest for the thesis. This section offers an overview of the nonlinear mechanisms resulting in absorption rather than a detailed theoritical description of the physics at play.

Multiphoton ionization

At lower power, a material is transparent to wavelength λ because its band gap E_g is larger than a photon's energy $E_p = hc/\lambda$ where h is Planck's constant and c the speed of light in vacuum. Electrons in the valance band can thus not acquire enough energy from a photon to reach the conduction band (to ionize). Figure 2.8(a) illustrates the multiphoton ionization process. There is always a non-zero probability that an electron receives the energy of many photons simultaneously and thus acquire enough energy to overcome the band gap. However, given the short interaction time between the photon and the electron, the probability that another photon interacts with the same electron during this time is so low at usual intensities that the process can be considered as never occuring. At very high intensities, the photon density is such that it is likely that an electron interacts with many photons simultaneously, resulting in its excitation to the conduction band.

Tunnel ionization

The high amplitude of the oscillating eletric field at the focal spot heavily distorts the band structure of the material. As the distortion gets more important, the potential barrier preventing electrons from reaching the conduction band disappears as illustrated in Figure 2.8(b). This allows the electrons to tunnel through. Tunnel ionization usually occurs along multiphoton ionization by simply reducing the band gap slightly, thus allowing an electron to reach the conduction band by simultaneously absorbing fewer photons than would be necessary without tunneling.

Avalanche ionization

Avalanche ionization (illustrated in Figure 2.8(c)) can only occur once electrons have already been ionized by another nonlinear mechanism. These free electrons are accelerated by the incoming photons and eventually acquire a kinetic energy larger than the band gap E_g. As they collide with the neighboring atoms, they impart their energy to another electron, exciting it to the conduction band.

2.2.2 Experimental parameters in laser writing

The material modification induced by laser writing is dependant on a wide array of parameters. The aim of this section is to describe qualitatively the role of each parameter rather than list every set of parameters and their resulting material modification available in the literature.

Wavelength

The laser's wavelength is a very important parameter in laser writing. First, if the photon energy at the corresponding wavelength is higher than the material's band gap, light will be absorbed at the material's surface by standard linear processes, not at the focal spot. Similarly, if the photon energy is too low, the number of photons required for multiphoton

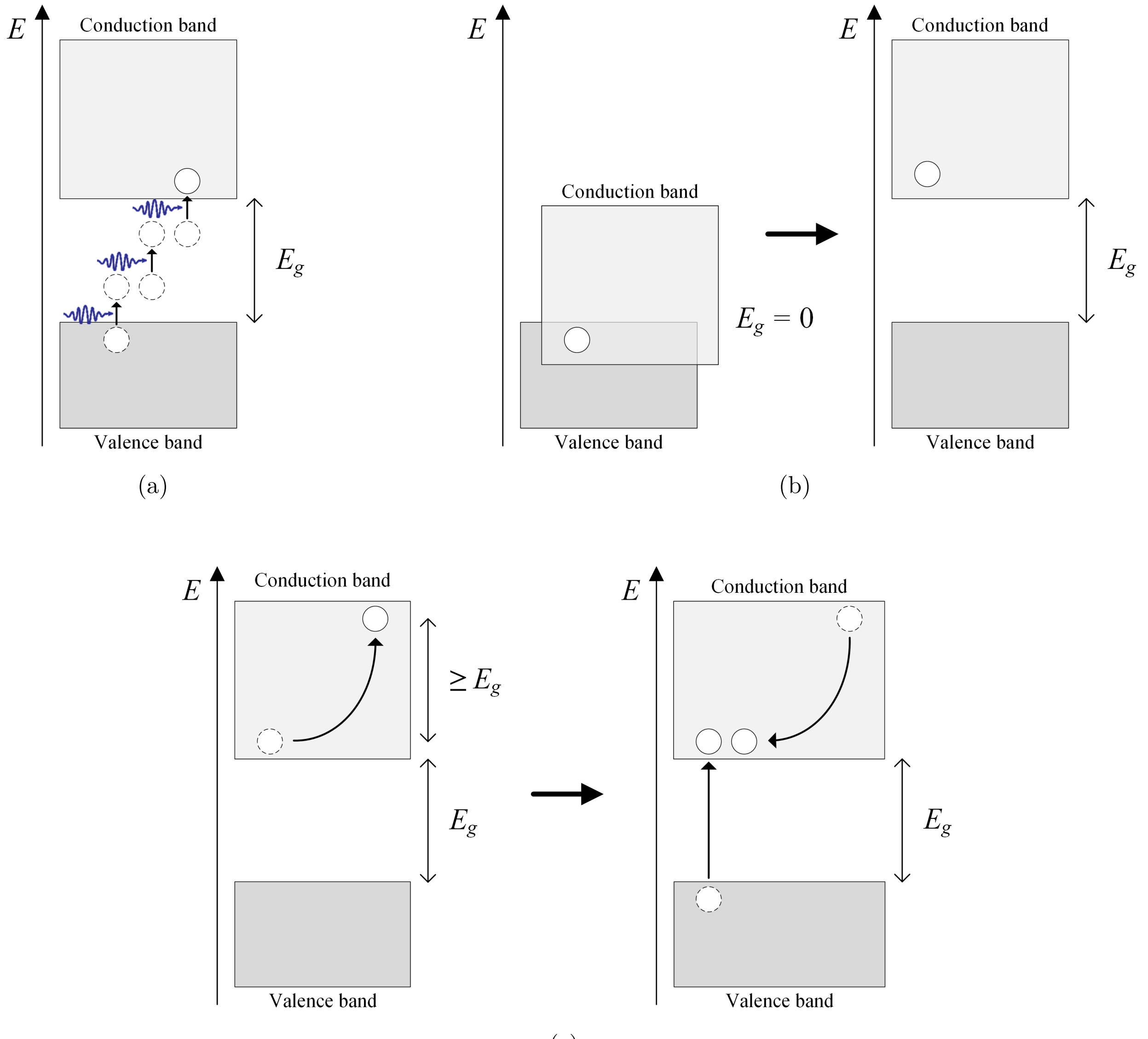

(a) (b)

(c)

Figure 2.8 Visual representation of nonlinear absorption mechanisms. (a) Multiphoton ionization. (b) Tunnel ionization. (c) Avalanche ionization.

ionization to occur will be too large. It has also been shown that the photon energy relative to the material's band gap has a direct effect on the relative contributions of multiphoton ionization and tunnel ionization. [10]

Power

The laser's power has a direct impact on the total energy deposited in the material. Figure 2.9 shows the intensity of each pulse reaching a given point in the material over time (as the sample is translated). As the focal spot gets closer to the given point, the intensity of each pulse gets higher until the focal spot reaches that point, after which the intensity received by each pulse gets lower as the focal spot gets further. The power of the laser simply changes the intensity — or energy — of each pulse.

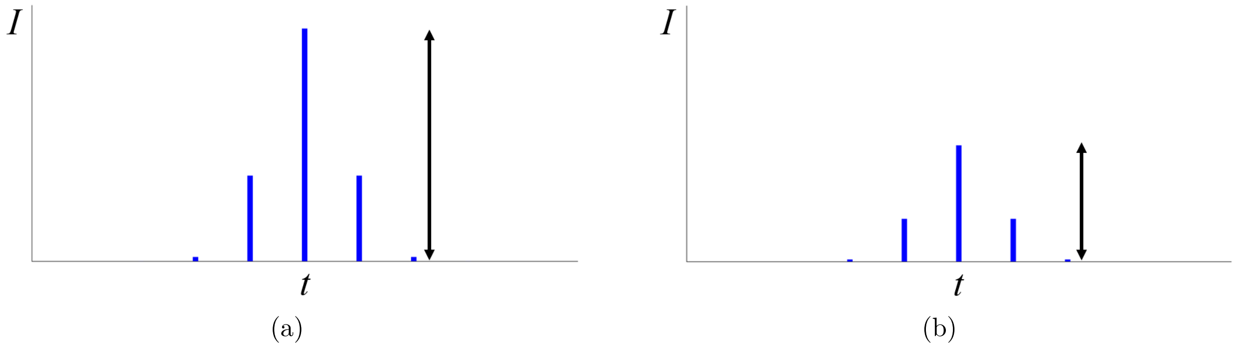

(a) (b)

Figure 2.9 Irradiating intensity at a given point in the material over time for (a) an arbitrary power and (b) half that power. The energy of each pulse irradiating the material is directly proportional to the laser power.

Translation speed

The translation speed of the sample relative to the focal spot has a very important effect on the resulting material modification. Figure 2.10 shows how it impacts the energy deposition profile. The temporal spacing between each incoming pulse is unchanged, but the number of incoming pulses or total exposition time at a single point is directly dependent on the translation speed.

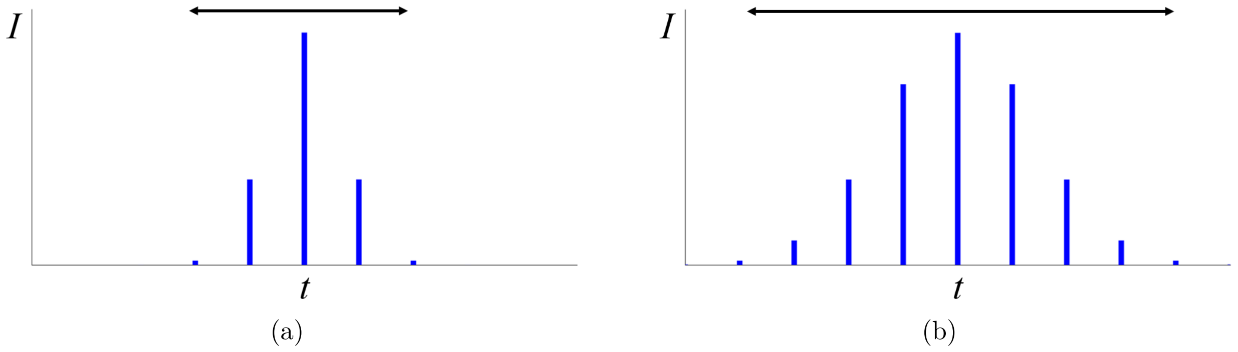

(a) (b)

Figure 2.10 Irradiating intensity at a given point in the material over time for (a) an arbitrary translation speed and (b) half that translation speed. The exposition time and thus the number of pulses affecting the given point is dependent on the translation speed.

Repetition rate

Figure 5.3 shows how the repetition rate of the laser impacts the energy deposition profile. The repetition rate changes the temporal spacing between pulses and thus has an effect on the number of pulses received at a given point in the material along with the translation speed.

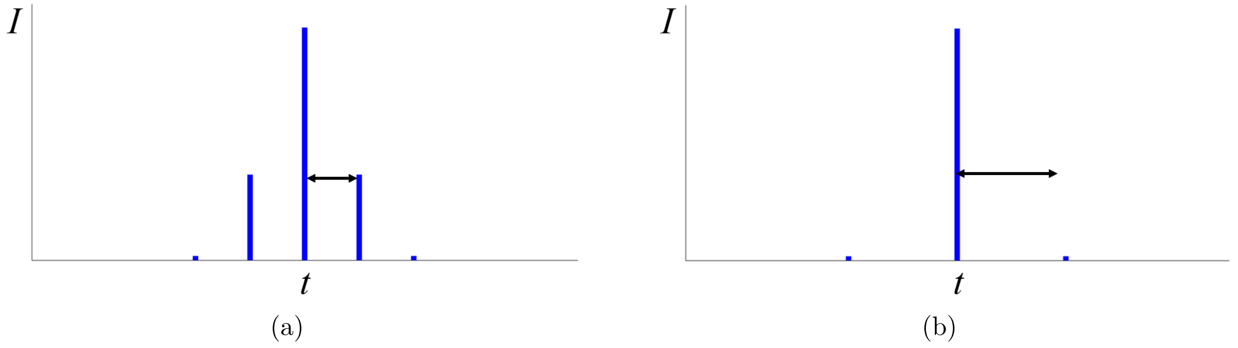

(a) (b)

Figure 2.11 Irradiating intensity at a given point in the material over time for (a) an arbitrary repetition rate and (b) half that repetition rate.The temporal separation between pulses and thus the number of pulses for a given exposition time (translation speed) are dependent on the repetition rate of the laser.

Focusing objective

The focusing objective has a direct effect on the shape of the focal spot and hence on the material modification. Figure 2.12 shows a few focal spots from the use of objectives with different numerical apertures. It can be seen that a lower NA produces a focal spot stretched laterally and even more so along its propagation axis. The use of an objective with higher NA focuses the beam much tighter and produces a focal spot of a more circular shape. For a similar laser power, the resulting intensity is much higher given the lower spatial spread.

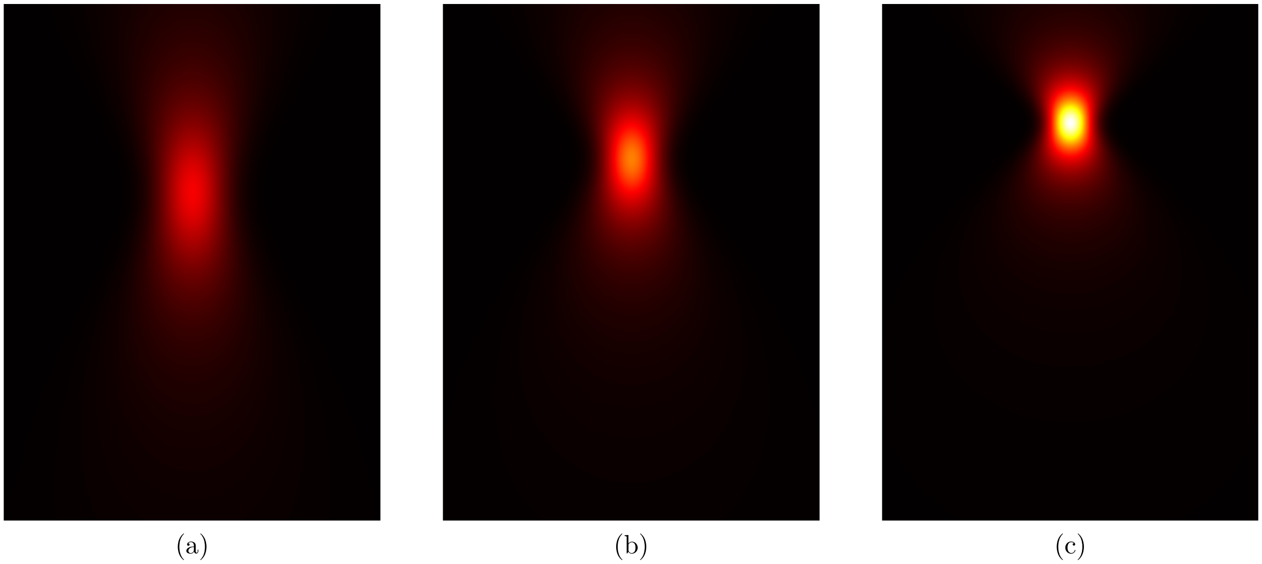
(a) (b) (c)

Figure 2.12 Focal spot obtained from the use of (a) a low NA objective, (b) a medium NA objective and (c) a high NA objective.

Glass type

Direct laser writing is highly dependent on the type of glass used. First, its band gap relative to the wavelength used dictates the relative importance of multiphoton and tunnel ionization. Secondly, different glasses display different susceptibilities to nonlinear effects. Some glasses are also doped and thus display different photosensitivities. Finally, glasses generally differ in refractive index. The interface between air and glass that the beam must cross produces a defocusing effect, best explained using Figure 2.13. The rays coming from a larger angle are refracted further from the original focal point than those coming from a lower angle, causing a stretching of the focal spot along the propagation axis. Writing in glasses with higher refractive indices exacerbates this effect. Writing deeper in the material causes a larger defocusing due to a longer propagation in the material. The use of a high NA objective is also more subject to this effect because of the corresponding higher angular spread.

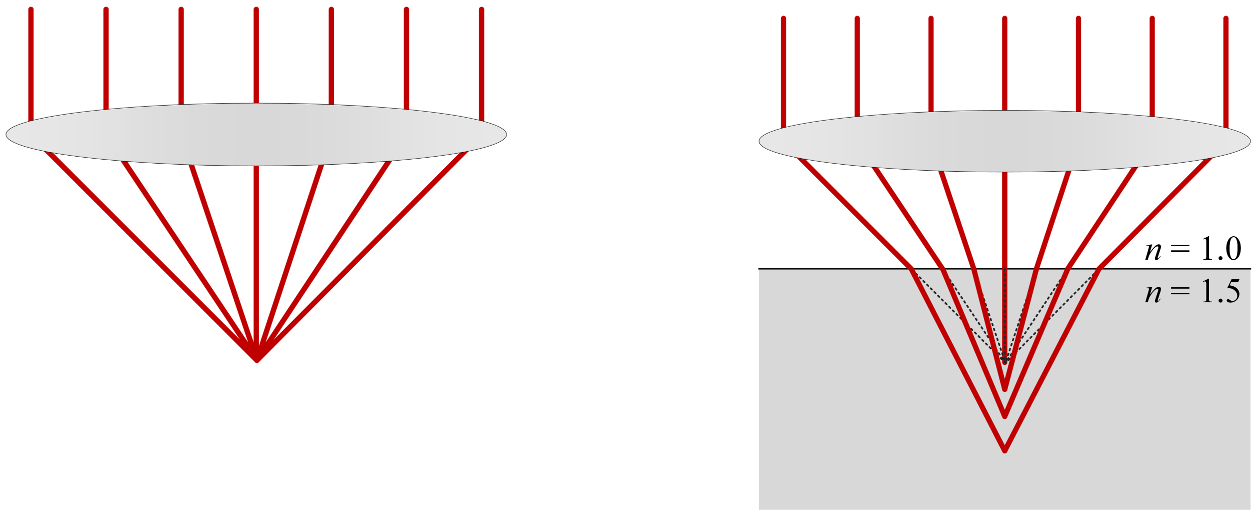

(a)

(b)

Figure 2.13 (a) Standard focusing with all rays meeting at the focal spot. (b) Defocusing effect caused by refraction at the air-glass interface. Rays coming from a larger angle are focused deeper in the material, spreading the focal spot.

2.3 Interferometry

Due to its importance in refractive index profiling, the subject of interferometry is covered in this section. Interference is the result of the interaction of two or more waves. Whether the waves are sound waves, water surface waves, an oscillating string or an electromagnetic wave is irrelevent, all are subject to interference. As waves meet, the resulting amplitude is simply the sum of each wave's amplitude. Figure 2.14 illustrates the phenomenon. A monochromatic beam of light can be considered in its most simple form as a propagating sinusoidal oscillation of the local electric and magnetic fields. As beams coincide, their respective contribution to the electric field combine to produce a resulting electric field. If two meeting electromagnetic waves of the same frequency happen to be in phase as in Figure 2.14(a), the crests of both waves coincide, as do their troughs. The result is an oscillation of the electric field of twice the amplitude (constructive interference). Similarly, if two electromagnetic waves of the same frequency but in antiphase meet as in Figure 2.14(b), the crests coincide perfectly with the troughs, resulting in a constant zero electric field (destructive interference). Figure 2.14(c) shows the same two waves but with arbitrary phase difference. As light intensity is proportional to the electric field squared, the interference of the two beams results in dark and bright fringes whose location depends on the phase difference between the two beams. Of course, the electric field in which light waves propagate is actually three dimensional. Figure 2.16(a) shows a typical fringe pattern across two colinear beams.

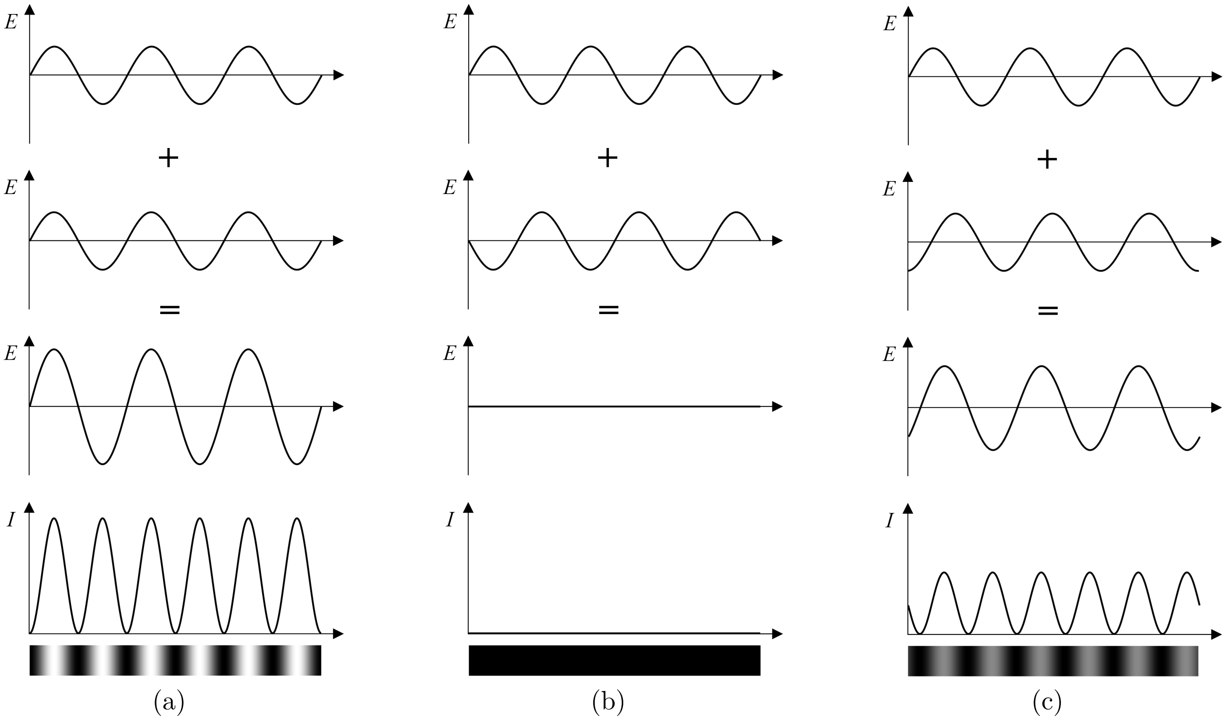

(a) (b) (c)

Figure 2.14 (a) Constructive interference ($\Delta\varphi = 0$). (b) Destructive interference ($\Delta\varphi = \pi$). (c) Interference of two waves with $\Delta\varphi = 1.5$.

2.3.1 Interferometers

Interferometers are optical setups that allow for interferometric measurements by capturing the fringe pattern and its deformation produced by the studied sample. Interferometers usually split a light beam coming from a single light source in two beams traveling different paths, one of which goes through the studied sample. The beams are later recombined and the fringe pattern imaged by a camera. Figure 2.15 shows a few examples of different optical setups used in interferometry, each achieving the beam split and recombination in different ways. Figure 2.15(a) shows a Michelson interferometer where the collimated beam is first split by a beamsplitter, then reflected using mirrors before being recombined by the same beamsplitter and forming an image on a camera. The major inconvenience in this setup is the fact that light goes through the sample twice. In Figure 2.15(b) is a Mach-Zehnder. In this configuration, the beam goes through the sample only once. However, two beamsplitters are necessary and adjusting the phase delay in the reference arm cannot be done by moving a single mirror as with the Michelson interferometer. Figure 2.15(c) shows a ring interferometer. Such an interferometer cannot be used to image a sample since the two beams each travel the same path in reverse direction. However, due to the ring configuration, the phase shift between the two beams is proportional to the angular velocity of the interferometer, making gyroscopes one of its main application.

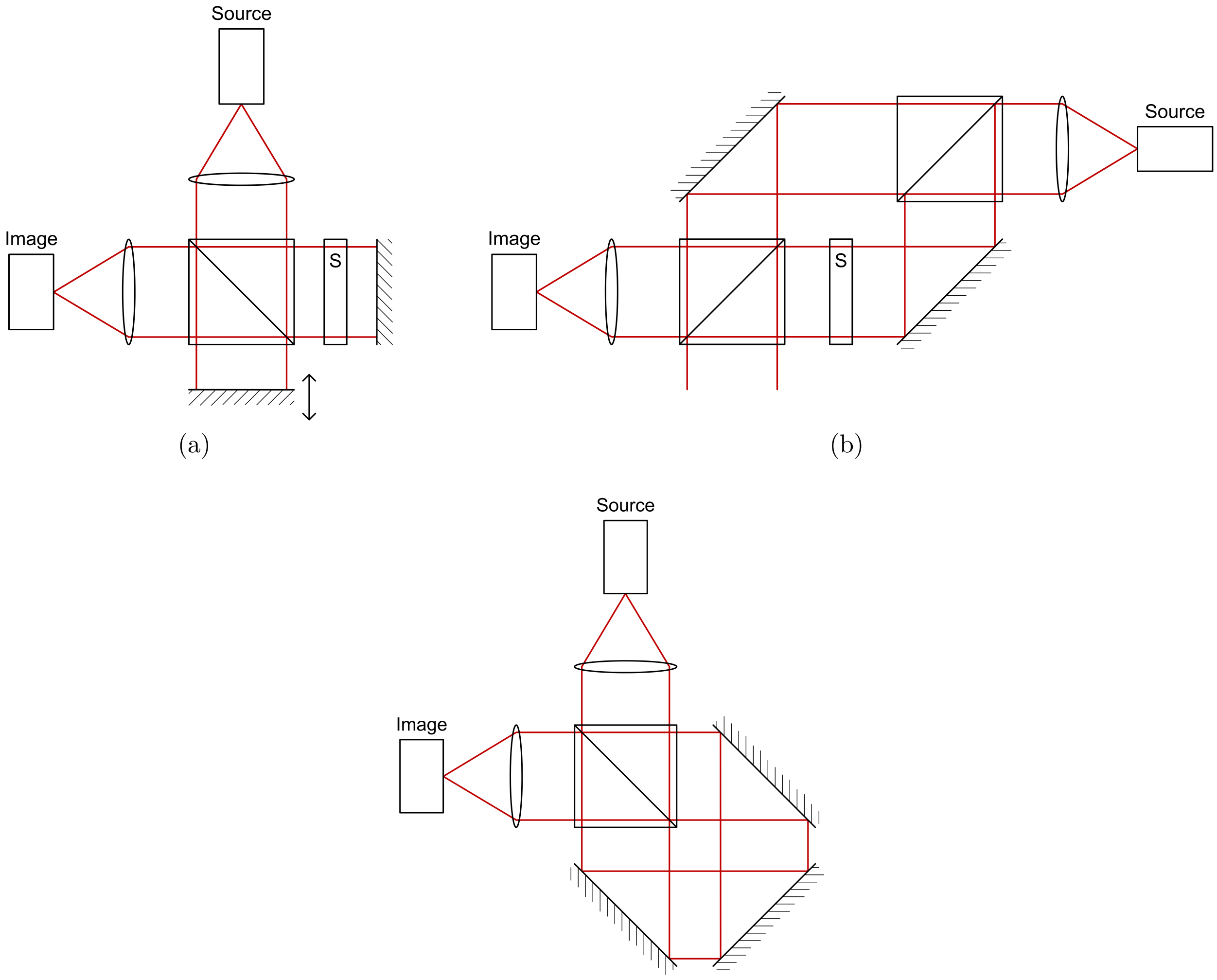

(a)

(b)

(c)

Figure 2.15 (a) Michelson interferometer. (b) Mach-Zehnder interferometer. (c) Ring interferometer.

2.3.2 Phase recovery

The main application of interferometry is the use of the interference phenomenon to measure differences in optical path length — or phase — which can in turn give information on surface irregularity, surface flatness or refractive index changes. For example, in the absence of sample in the interferometer, the fringe pattern might look something like Figure 2.16(a). As a hypothetical sample is introduced in the interferometer, the fringe pattern is deformed by a defect in the sample (Figure 2.16(b)). Before the sample was introduced, the difference in optical path length at this specific position on the camera was such that destructive interference occured. The sample's defect introduced a change in optical path length meaning the destructive interference does not occur anymore. By taking the difference between the fringe pattern before and after the sample was introduced, one can obtain the optical path length change produced by the sample as shown in Figure 2.16(c). This type of image is

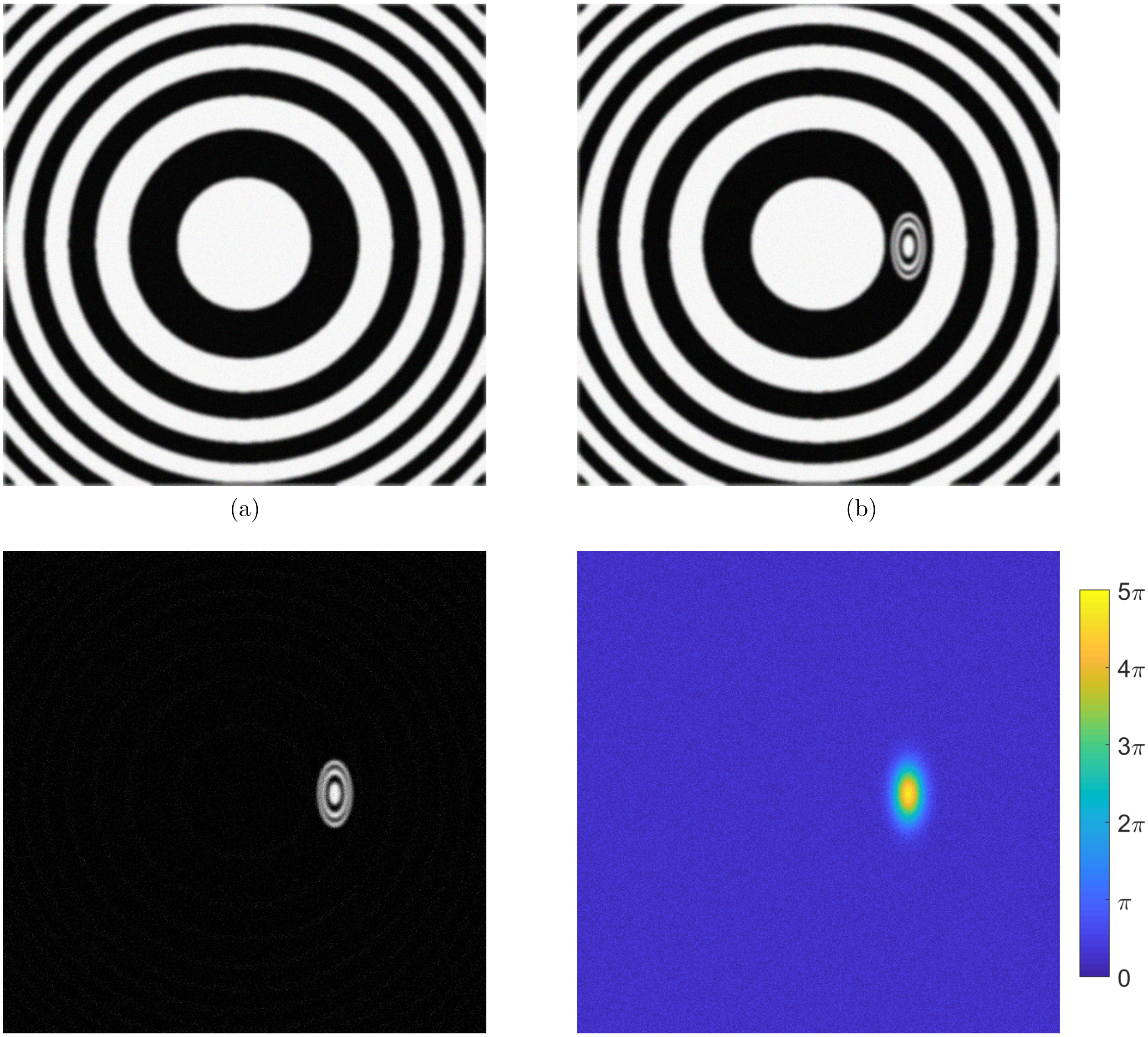

(a) (b)

(c) (d)

Figure 2.16 Fringe analysis. (a) Fringe pattern without sample. (b) Fringe pattern with a flat sample with a small defect. (c) Difference in the fringe pattern produced by the sample. (d) Phase recovered from fringe deformation using a phase recovery algorithm.

very much like a topographic map where alternating colors indicates a phase change of π. In this example, the center of the defect would thus have introduced a phase change of 5π. The way the fringes move when adjusting the phase delay in the reference arm (by moving the reference mirror for example), either towards the inside of the circular pattern or towards the outside gives an indication on if the phase shift of 5π is positive or negative relative to the reference. There are many ways to automatically analyze fringe deformation and recover the two-dimensional phase shift produced by the sample instead of counting fringes. The main methods are explained in this section.

Fringe center measurement

The first and most simple method to analyze fringes relies on acquiring a single interferogram and finding the fringe centers (the fringe maximum and minimum). The values between the fringes centers are interpolated and a phase image can be reconstructed as in Figure 2.16(d). This method is limited by the ability to automatically identify the fringe centers with precision and by intensity fluctuations which are then interpreted as phase variations, leading to errors. Furthermore, the fringes must be moved to remove some ambiguities regarding the sign of the phase shift as in the fringe counting method previously described.

Fourier transform

Another method overcomes these limitations by acquiring interferograms continuously while fringes are moved at a constant speed. The intensity at each pixel of the camera then follows a sine function of stable frequency ω_0 with phase φ different for each pixel. The phase can be retrieved by taking the Fourier transform of each sine function for each pixel:

$$\mathcal{F}\Big\{ \cos\left(\omega_0 t - \varphi\right) \Big\} = \delta\left(\omega - \omega_0\right) e^{i\varphi} \tag{2.5}$$

and simply taking the phase of the dominant frequency ω_0. This method is easy to implement and does not rely on manually analyzing fringe patterns. However, even with fast Fourier transform algorithms, it is slow due to the large amount of data required.

Phase shifting interferometry

A better method, usually called phase shifting interferometry, achieves a similar result at much greater speed by acquiring only a few interferograms, each with a precise phase delay in the reference arm. The fundamental equation of phase shifting interferometry is

$$\tan\varphi = \frac{\displaystyle\sum_{m=1}^{M} I_m \sin\left(\frac{2\pi(m-1)}{M}\right)}{\displaystyle\sum_{m=1}^{M} I_m \cos\left(\frac{2\pi(m-1)}{M}\right)} \tag{2.6}$$

where I_m is the m^{th} image frame (interferogram) and M the total number of frames. For the typical 4-frame method where the phase step between each frame is $\pi/2$, the equation becomes

$$\tan\varphi = -\frac{I_2 - I_4}{I_1 - I_3}. \tag{2.7}$$

To reduce the error in using such an algorithm for phase recovery, it is possible to average two phase images by aqcuiring 8 frames. However, as some of these frames overlap, it is best to calculate one phase image from two sets of data: one for frames 1-4, and another for frames 2-5. Equation 2.6 can then be written

$$\tan\varphi_1 = \frac{N_1}{D_1} = -\frac{I_2 - I_4}{I_1 - I_3} \tag{2.8}$$

$$\tan\varphi_2 = \frac{N_2}{D_2} = -\frac{I_2 - I_4}{I_5 - I_3} \tag{2.9}$$

for each set of data since I_5 and I_1 are equivalent (phase step of 0). Schwider showed in 1983 that for this type of averaging,

$$\tan\varphi = \frac{N_1 + N_2}{D_1 + D_2} = -\frac{2(I_2 - I_4)}{I_1 - 2I_3 + I_5} \tag{2.10}$$

which is the well known 5 frame algorithm which is far less sensitive to phase step miscalibration. [11] Algorithms using more frames were developped in 1995 by Schmit and Creath [12] by extending the same averaging method. They also present algorithms derived from averaging multiple 3-frame sets which are even less sensitive to phase step miscalibration for the same number of acquired frames but are more sensitive to detector nonlinearity and require slightly more arithmetics. Detector nonlinearity is however negligible for most detectors. Table 2.2 offers a summary of a few of these algorithms and their corresponding noise levels due to phase step miscalibration and detector nonlinearity. Since then, many other algorithms allowing for arbitrary phase steps between frames have been developped and can be used if consistant $\pi/2$ phase stepping is not achievable in a specific application. [11,13]

Table 2.2 Phase shifting interferometry algorithms and corresponding error due to phase step miscalibration and detector 2$^{\text{nd}}$ order nonlinearity. [12]

Number of frame	$-\tan(\varphi)$	Error from 20% phase step miscalibration (rad)	Error from 20% detector nonlinearity (rad)
4	$\dfrac{I_2 - I_4}{I_1 - I_3}$	0.151	0.000
4	$\dfrac{2(I_2 - I_3)}{I_1 - I_2 - I_3 + I_4}$	0.049	0.097
5	$\dfrac{2(I_2 - I_4)}{I_1 - 2I_3 + I_5}$	0.049	0.000
5	$\dfrac{3I_2 - 3I_3 - I_4 + I_5)}{I_1 - I_2 - 3I_3 + 3I_4}$	0.008	0.082
6	$\dfrac{3I_2 - 4I_4 + I_6}{I_1 - 4I_3 + 3I_5}$	0.008	0.000
6	$\dfrac{4(I_2 - I_3 - I_4 + I_5)}{I_1 - I_2 - 6I_3 + 6I_4 + I_5 - I_6}$	0.003	0.049

Transport of intensity equation

All techniques presented thus far rely on interferometric setups using highly coherent light sources such as lasers. In some applications — most often related to biology — where a high quality image is required, coherent light sources and interferometers are not suitable due to inherent speckle and undesirable fringe patterns from various surface reflections. Although this method is described in the *Interferometry* section for conveniance, it is most definetly not an interferometric method. Teague derived in 1983 [14] an equation — which he named the transport of intensity equation — relating the phase shift produced by a phase object to the intensity distribution:

$$-k\frac{\partial I(x,y,z)}{\partial z} = \nabla_\perp \cdot \Big[I(x,y,z)\nabla_\perp\varphi(x,y,z)\Big] \tag{2.11}$$

where k is the wavenumber and $\nabla_\perp$ is the gradient operator transverse to light propagation. The right part of Equation 2.11 can be simplified by assuming that the illumination field is constant over the illumination region:

$$\begin{aligned} \nabla_\perp \cdot \Big[I(x,y,z) \nabla_\perp \varphi(x,y,z) \Big] &= \nabla_\perp I(x,y,z) \nabla_\perp \varphi(x,y,z) + I(x,y,z) \nabla_\perp^2 \varphi(x,y,z) \\ &= I(x,y,z) \nabla_\perp^2 \varphi(x,y,z). \end{aligned} \tag{2.12}$$

The derivative on the left part of Equation 2.11 is usually approximated by measuring the intensity distribution at two defocused positions:

$$\frac{\partial I(x,y,z)}{\partial z} \approx \frac{I(x,y,z+\Delta z) - I(x,y,z-\Delta z)}{2\Delta z} \tag{2.13}$$

such that Equation 2.11 can be written

$$\nabla_\perp^2 \varphi(x,y,z) = -k \frac{I(x,y,z+\Delta z) - I(x,y,z-\Delta z)}{2\Delta z I(x,y,z)}. \tag{2.14}$$

The phase can thus be recovered from three intensity images, each at different focal positions, by inverting the transverse Laplacian operator $\nabla_\perp^2$. Fortunately, many different algorithms have been developed, each with different limitations regarding the boundary conditions. Most algorithms rely on Fourier transforms or discrete cosine transforms. [15–17]

2.4 Refractive index profiling

Most methods for measuring refractive index profiles were developed decades ago for the characterization of optical fibers. This sections offers a review of today's most widely used methods as well as a discussion on the techniques used to estimate the refractive index profile of laser written waveguides.

2.4.1 Refracted near-field

The refracted near-field (RNF) method is probably the most widely used method to measure the refractive index of optical fibers. First demonstrated by Stewart in 1977 [18], it was further developed by White in 1979 [19] and Young in 1981 [20]. Its working principles are illustrated in Figure 2.17. An optical fiber is first immersed in an index matching liquid. A beam is focused on the end-facet of the optical fiber at a numerical aperture much greater than that of the fiber. The method consists in measuring the power of light refracted from the fiber, hence a stop is put on the fiber's end to prevent guided light from reaching the photodetector. Light reaching the photodetector is shaped as a hollow cone of angle $\theta(n)$ and angular thickness $\theta(n) - \theta_s$ where θ_s is the smallest angle for which a ray will hit the photodetector and n is the refractive index at the focal spot. Since the angle $\theta(n)$ varies depending on n while θ_s is fixed, the amount of power reaching the photodetector varies with n. White showed that under the assumption that the light source is Lambertian, the measured power is proportional to n. Young later showed that even if the source is not Lambertian, the power is still suffiently linear with n if the refractive index difference of the fiber is small, as is usually the case. By scanning the light source over the whole end-face of the fiber, one can obtain the power for each scanned point $P(x, y)$ and thus deduce the refractive index profile $n(x, y)$ of the end-face.

The method has gained popularity through the years due to its simple optical setup and little sample preparation requirement. Indeed, the fiber need only to be cleaved before the measurement is done. However, acquiring a complete refractive index profile requires two-dimensional scanning of the fiber and is thus a lengthy process. Furthermore, since the measurement is done only on the end-facet of the fiber, it is impossible to verify if the fiber is constant along its propagation axis without cleaving further along the fiber and thus destroying the sample.

The RNF method has been used on laser written waveguides but some drawbacks of the method are more pronounced than for optical fibers. First, it is a lot more complicated and time consuming to make a flat and polished entry to the focused beam than to cleave a fiber. For this reason, it is not generally conceivable to measure the waveguide at multiple positions along its propagation axis.

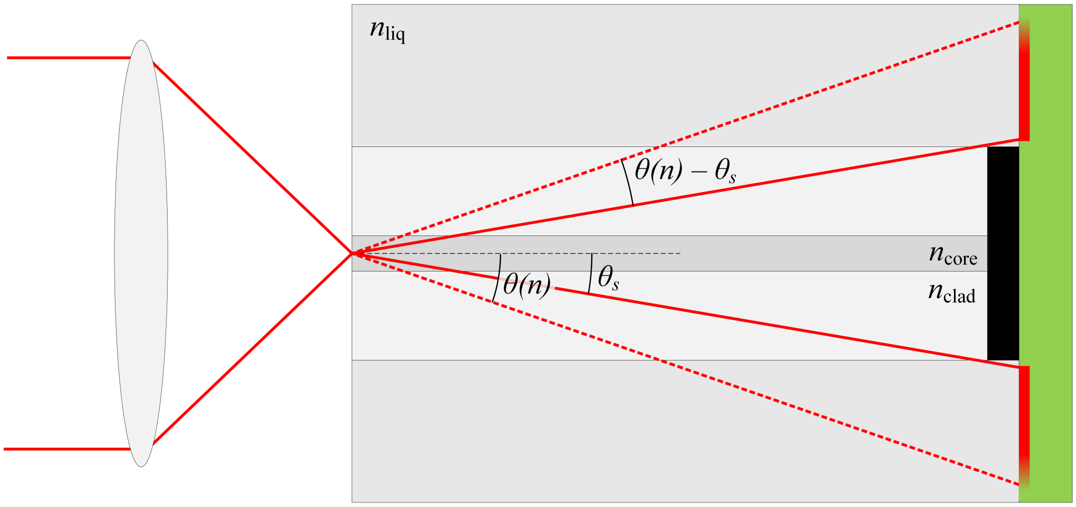

Figure 2.17 Schematic of a typical setup for refracted near-field (RNF) measurements.

2.4.2 Quantitative phase imaging

Another widely used technique to measure refractive index profiles is by measuring the phase shift produced by the optical fiber. The phase shift is usually measured using an interferometric setup or using the transport of intensity equation. The method is most often done as illustrated in Figure 2.18, that is with the beam perpendicular to the fiber's propagation axis. The phase shift produced by the fiber is related to its refractive index profile by the following equation:

$$\varphi\left(x,z\right)=\frac{2\pi}{\lambda}\int\Delta n\left(x,y,z\right)\mathrm{dy}. \tag{2.15}$$

The delicate part of profiling waveguides using a quantitative phase imaging approach is solving Equation 2.15 for $\Delta n(x,y,z)$. Indeed, regardless of what $\varphi(x,z)$ is, there is always an infinite number of refractive index profiles $\Delta n(x,y,z)$ for which Equation 2.15 holds. However, from this infinite set of functions, only a small fraction also agree with other observables. First methods for optical fibers relied on assuming the step-index nature of the fiber and analyzing its transversal phase shift. For example, taking the fiber illustrated in Figure 2.18, the cladding and core diameters are easily identifiable from the measured $\varphi(x)$. By assuming circular symmetry and a step-index profile, the refractive index of the core can be calculated from the height of the central crest.

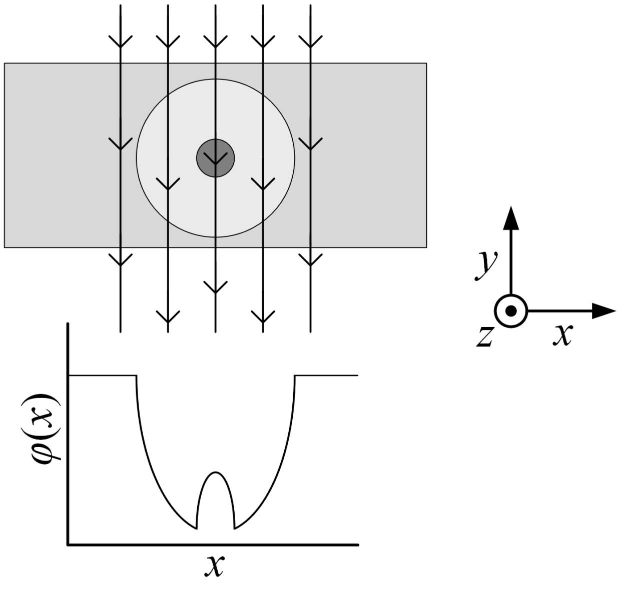

Figure 2.18 Optical fiber arrangement used in most quantitative phase imaging methods. The light beam crosses the fiber perpendicularly to its propagation axis.

Inverse Abel transform

A more exact method relies on assuming axial symmetry of the optical fiber's refractive index profile. In this case, Equation 2.15 is known to mathematicians as an Abel transform. Solving for $\Delta n(x, y, z)$ — or $\Delta n(r, z)$ in this case — requires the use of an inverse Abel transform:

$$\Delta n(r, z) = \mathcal{A}^{-1}\Big\{\varphi(r, z)\Big\}. \tag{2.16}$$

Many different implementations using different algorithms have been presented over the years, each bringing improvement regarding susceptibility to noise in the initial signal. [21,22]

Tomography (inverse Radon transform)

If $\Delta n(x, y, z)$ is not axially symmetric, Equation 2.15 cannot be solved uniquely. One must then resort to tomography techniques by measuring the phase shift induced by the waveguide for different illumination angles as shown in Figure 3.7(a) for a hypothetical fiber. The resulting $\varphi(d, \alpha)$ where d is the distance from the center of the fiber and α is the illumination angle is called a tomogram and is shown in Figure 3.7(b). The inverse Radon transform

$$\Delta n(x, y, z) = \mathcal{R}^{-1}\Big\{\varphi(d, z, \alpha)\Big\} \tag{2.17}$$

allows for the refractive index profile reconstruction. Much like the inverse Abel transform, many algorithms have been developed over the years with the filtered back projection algorithm being the most commonly used. [23,24] Figures 3.7(c) and (d) shows the resulting refractive index profile of a hypothetical optical fiber for a reconstruction based on 20 and 180 illumination angles respectively. Artifacts due to the discretization of the inverse Radon transform used in the algorithm are noticeable for step angles larger than 1 degree. Although most implementations of the inverse Radon transform require the illumination angles to cover 180° (the other 180° being redundant since the propagation direction is simply reversed), many other methods have been developped to approximate the reconstruction from a limited set of illumination angles. [25,26] The precision of these reconstruction techniques vary wildly depending on the studied sample and in general do not reach the same level of quality as a full 180° tomography.

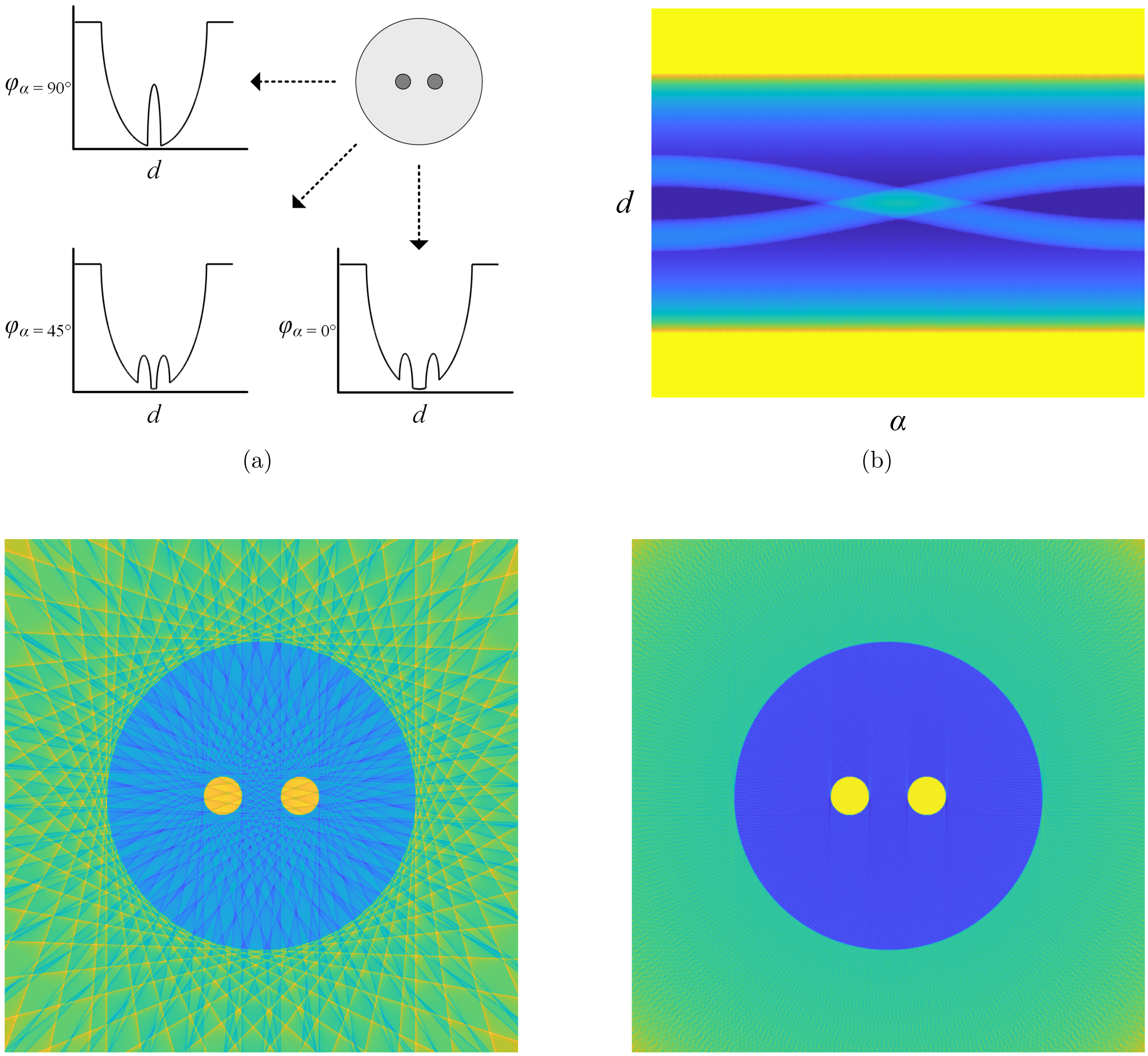

(a) (b)

(c) (d)

Figure 2.19 (a) Measurement of phase shifts for multiple illumination angles. (b) Tomogram ($\varphi(d,\alpha)$) of the hypothetical optical fiber. (c) Refractive index profile reconstructed by an inverse Radon transform using 20 illumination angles. (d) Refractive index profile reconstructed by an inverse Radon transform using 180 illumination angles.

2.4.3 Profiling laser written waveguides

The refractive index profiling methods presented thus far have major problems when applied to the measurement of laser written waveguides. The commonly used RNF technique is destructive and time-consuming since it requires the polishing of both faces before a measurement can be made and a lengthy scanning process. Furthermore, it only gives information on the exposed face while the refractive index profile of laser written waveguides may change along their propagation axis under some experimental conditions since it is based on the absorption of discrete laser pulses.

Some rely on measuring the sample's top surface reflectivity where a waveguide has been inscribed and assuming a step-index to recover a value for the average refractive index change produced by laser writing. [27]

Others have tried to adapt the tomography technique to glass samples by rotating the beam around the sample instead of rotating the sample. [28] Angles up to only 36° were achieved, after which the induced distortion in the image becomes significant. Given the lack of rotation angle and image distortion produced by the angled air-glass interface, only the optical path length (OPL) for a given angle is obtained, from which the ellipticity of the waveguide is deduced by again assuming a step-index refractive index profile.

The only true two-dimensional refractive index profiling technique for waveguides available in the literature is based on quantitative phase imaging and has been presented by Osellame in 2005. [29] In this method, light is sent along the waveguide's propagation axis instead of tranversly to measure the OPL difference across its face. However, the main drawback of the technique is the necessity to use a very thin sample to keep the OPL difference between neighboring camera pixels low enough for phase unwrapping to be feasible, meaning that the method is destructive, assumes that the waveguide is constant along its propagation axis and requires a very lengthy sample preparation process.

CHAPTER 3 REFRACTIVE INDEX PROFILING SYSTEM

This chapter describes the system for refractive index profiling of optical fibers and laser written waveguides developed during my master's. The experimental method is first presented followed by results and a discussion for various refractive index profile reconstruction techniques and sample types.

3.1 Experimental method

The refractive index profiling system is based on a quantitative phase imaging approach. Optical and mechanical systems as well as their integration to a LabVIEW control program allows the system to behave as a quantitative phase microscope at a fraction of the cost. Reconstruction of the refractive index profiles using various methods is also fully integrated to the LabVIEW progam allowing for fast measurements.

3.1.1 Quantitative phase imaging

The Mach-Zehnder interferometer (MZI) setup used for the phase measurement is shown in Figure 3.1. A HeNe laser at a wavelength of 632.8 nm is launched into an optical fiber. The light is split into the two arms of the interferometer using a 50:50 fiber coupler (C' in Figure 3.1). One arm features a piezoelectric actuator (A) to stretch the fiber and induce a phase delay. Each arm includes a fiber collimator (C1,2), a half-wave plate (HW1,2) and a polarizer (P1,2). Polarizers and wave plates are adjusted to maximize interference fringes visibility. The sample (S) is placed just before the objective with the beam of the interferometer passing through the sample transversally (i.e. the waveguide's propagation axis is orthogonal to the beam). The reference arm features an identical objective to match the sample arm to produce a flat phase reference. The beams are recombined by a beam-splitter and an image — the interferogram (as shown in Figure 3.2(a)) — is formed on the CMOS camera using the final lens (L).

The quantitative phase image is obtained from the interferogram using phase shifting interferometry algorithms such as those previously introduced in section 2.4.2 of Chapter 2. The software supports algorithms with an arbitrary number of frames depending on the wanted speed and precision. The use of these algorithms makes phase retrieval calculations very fast. Other techniques such as identifying fringe centers and the one used in the published article of Chapter 4 (Fourier transform based) lead to a similar result but are far from being

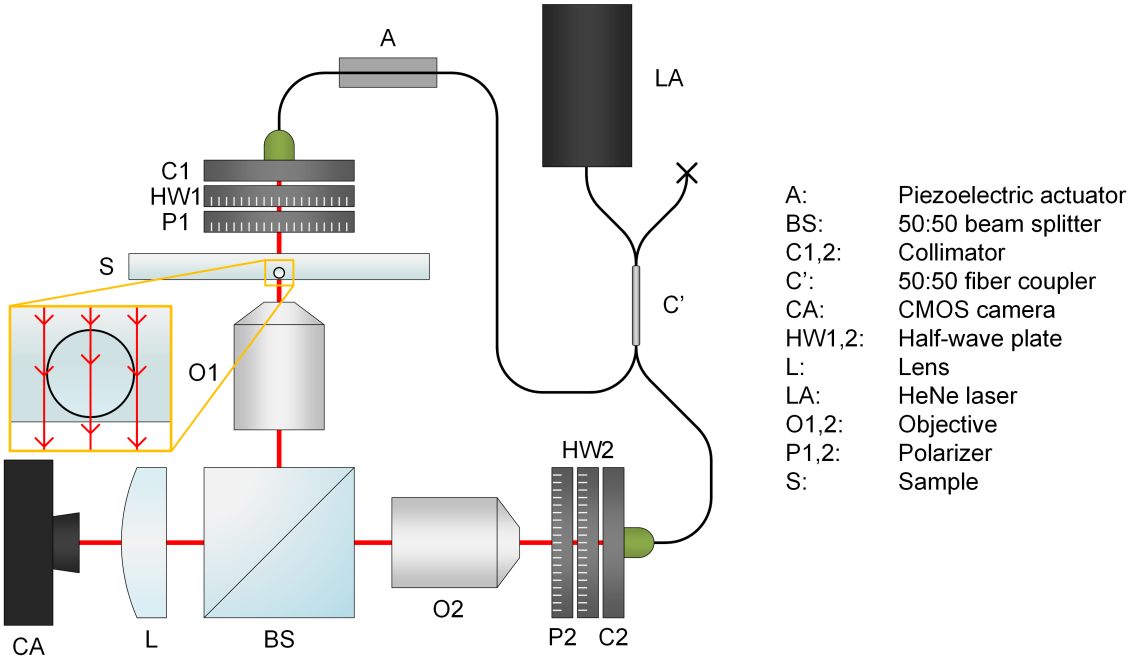

Figure 3.1 Mach-Zehnder interferometer setup used to measure the phase shift produced by the waveguide. A piezoelectric actuator is used to induce a phase delay in one arm. The polarizers and wave plates are adjusted to maximize the fringe visibility. An image of the sample is formed at the camera by the objective and lens.

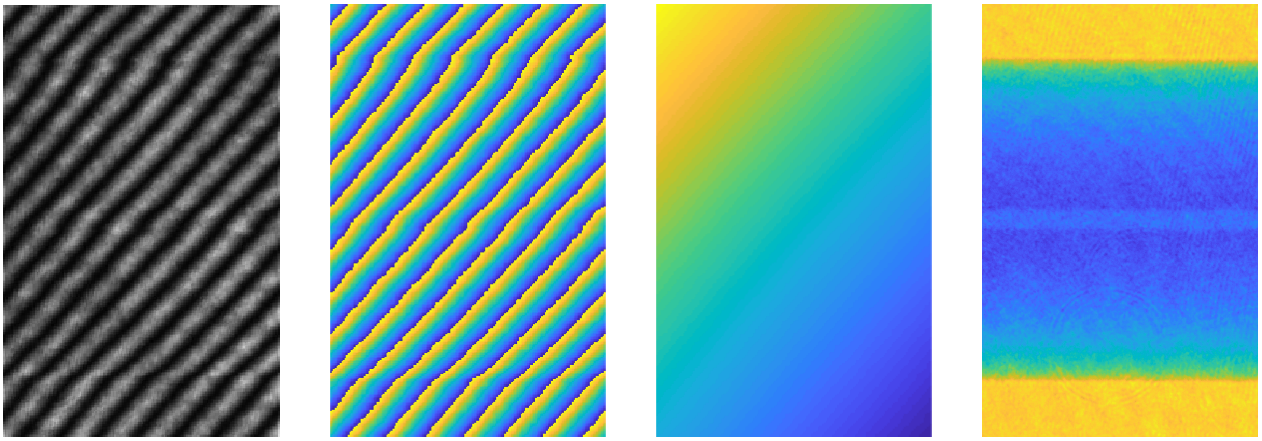

(a) (b) (c) (d)

Figure 3.2 (a) Interferogram obtained on the camera. (b) Phase image resulting from the use of an N-step algorithm. (c) Result of the unwrapping featuring the high amplitude quasi linear background. (d) Typical phase image of an SMF-28 optical fiber once the background pattern has been removed.

as fast. The $\pi/2$ phase stepping is done using the piezoelectric actuator A of figure 3.1. The use of strain gauge reader allows for linear movement of the piezoelectric actuator without hysteresis. As with most interferometric methods, the phase image must be unwrapped since the output of the phase retrieval algorithms is confined to the range $0-2\pi$ (see Figure 3.2). The obtained phase image features an almost linear background pattern of high amplitude that must be removed to resolve the fine phase variation due to the presence of the sample. The background is usually removed by subtracting a flat phase reference measurement, either further away from the waveguide in the sample or simply without any sample under the objective. A typical resulting phase image is shown in Figure 3.2(d). Depending on the studied sample and noise level required for a valid refractive index profile reconstruction, the phase image is typically averaged along the waveguide's propagation axis to obtain a one-dimensional phase shift.

3.1.2 Mecanical system and LabVIEW integration

Since an important goal of the project is to allow measurements to be done as quickly as possible, special care was given to the integration of the various components and to the streamlining of the measurement process. A render of the system is shown in Figure 3.3. All components are integrated in a single LabVIEW control program. The program continuously moves the piezoelectric actuator, acquires images from the camera between each steps and runs the calculations (N-step algorithms, phase unwrapping, background removal) to retrieve the phase data from the latest acquired pictures. The fast processing allows the user to obtain a real-time phase image of the sample. A screenshot of the graphical user interface and an overview of the software's functionalities are presented in Appendix A.

A 3-axis motorized translation stage with 30 nm resolution allows for precise positioning and focusing of the sample without perturbating the sensitive interferometer setup. It also allows for fast, automatic and simple cycling through the many waveguides inscribed in a glass slab, usually separated by a few hundreds of microns.

When measuring optical fibers, the fiber is held in place under the microscope objective using a 3D printed holder featuring V-grooves on two sides of a transparent cell to minimize lateral displacement during fiber rotation. The cell is made from two glass windows filled with refractive index matching liquid. For the measurement of hollow optical fibers, the fiber is introduced slowly in the cell to allow for liquid to fill the hollow regions. For tomographic imaging of optical fibers, a 0.9° step angle stepper motor is fixed to the translation stage. The fiber is firmly held on one end by a PhotoNova fiber clamp which is fixed to the stepper motor using a 3D printed adaptor that puts the center of rotation precisely at the center of

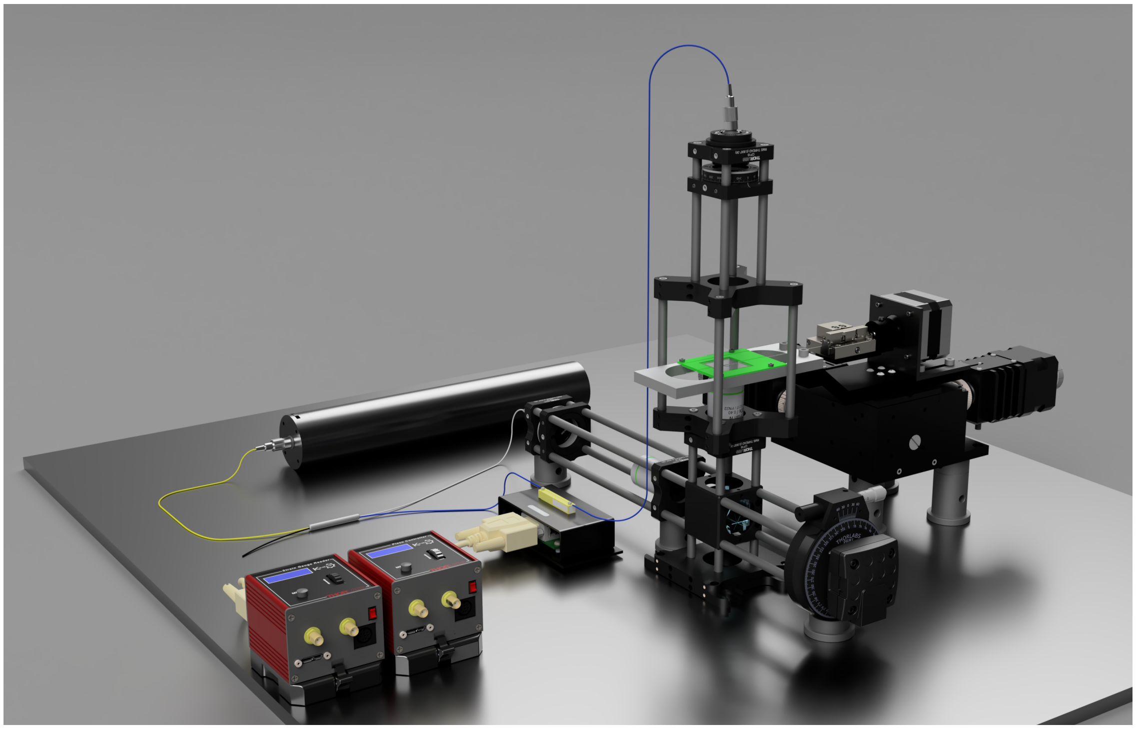

Figure 3.3 3D render of the refractive index profile system.

the fiber to minimize precession of the fiber. The LabVIEW program controls the automatic rotation of the stepper motor between phase measurements for tomographic images. It also automatically aligns the multiple phase projections since the fiber's lateral movement can never be eleminated completely.

A plastic box covers the whole assembly to prevent the sensitive fibered parts of the interferometers from being disturbed by the environment.

3.1.3 Refractive index profile reconstruction

Once a quantitative phase image of the waveguide has been obtained, its refractive index profile must be reconstructed by solving for $\Delta n(x, y, z)$ in Equation 2.15. The dependance in z — the waveguide's propagation axis — can be omitted by looking at a single slice of the waveguide or by averaging a constant portion of the waveguide, greatly simplifying and speeding up some refractive index reconstruction techniques. The system includes the two main reconstruction methods typically used for optical fibers: the inverse Abel transform and tomographic imaging. The inverse Abel transform reconstruction is done using a three-point method such as described by Kasim in [22] while the inverse Radon transform of tomographic imaging is processed using the common filtered back projection algorithm. The profiling system also supports a genetic algorithm based optimization method where the refractive index profile is modeled. The details of this reconstruction method are presented on their own in Chapter 4.

3.2 Results and discussion

This sections shows the main performance characteristics of the quantitative phase imaging method and the results of different refractive index reconstruction techniques. A discussion on each technique's performance is also made.

3.2.1 Quantitative phase imaging

Phase images as the one shown in Figure 3.2(d) typically have a noise level of about 0.2 radian when using phase recovery algorithms of at least 4 frames. The most important component of this noise comes from undesired interference fringes caused by the highly coherent light source and from the presence of fine dust particles in the cell when measuring optical fibers. As the measure of interest is most often a one-dimensional phase shift across the waveguide, the phase image is usually averaged along the waveguide's propagation axis to lower the noise level to under 0.01 radian.

To evaluate the spatial resolution, a sample with resolution targets made of sharp ∼0.75 μm deep square grooves of various widths was fabricated by applying photoresist to a 1 mm thick glass slab followed by exposure with an e-beam before etching. Another sample with identical patterns was also made with a chromium coating allowing the comparison between the phase measurement's spatial resolution to regular transmission microscopy (without the interference of the reference arm). Figure 3.4 shows the picture of the smallest 1 μm wide groove pattern for both transmission microscopy and the measured phase shift. It is clear from these pictures that the spatial resolution is slightly better than 1 μm (0.92 μm by the 10-90 criteria).

Depending on chosen parameters such as the resolution of the camera and the number of steps per phase image, acquisition of phase images at up to over 100 frames per second (fps) can be achieved. The high framerate allows the experimenter to rapidly scan his sample as if it was under a quantitative phase microscope. This is of particular interest for samples with nonuniform refractive index profiles (along their propagation axis) such as couplers and for samples whose uniformity has not been confirmed as is often the case with laser written waveguides.

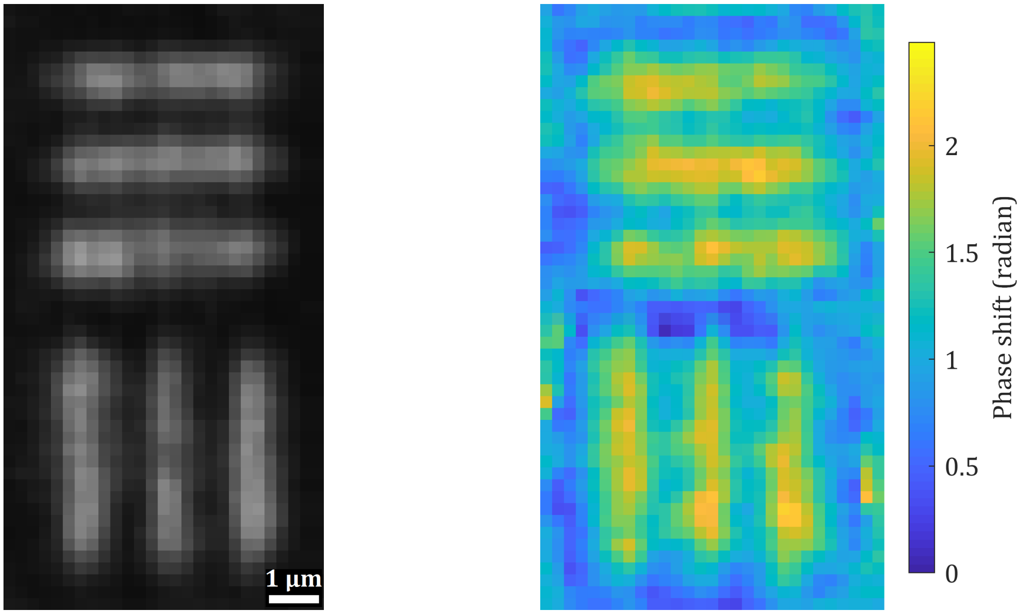

(a) (b)

Figure 3.4 Resulting image of the 1 µm resolution target for (a) transmitted light amplitude without interference and (b) the calculated phase shift. The pattern is clearly resolved, indicating a sub-micron spatial resolution.

3.2.2 Inverse Abel transform

This section presents the results for the refractive index profiling of axially symmetric optical fibers using the inverse Abel transform reconstruction method. Figure 3.5 shows the resulting refractive index profile of an SMF-28 fiber as well as a comparison to the well established RNF measurement technique on the fiber's core. Both methods are in very close agreement. Figure 3.6 shows the result of the inverse Abel transform reconstruction on double-clad fibers. The inverse Abel transform reconstruction process is unaffected by the more complex structure of these fibers. From these measurements, it is apparent that the noise level induced by the reconstruction process is around $1 \cdot 10^{-4}$ RIU. The noise is more important next to discontinuities such as at the core-cladding and cladding-liquid interfaces but is lower in regions of constant refractive index. The most important potential issue with the inverse Abel transform technique is its sensitivity to the identification of the fiber's center. Indeed, a slight offset between the fiber's center and the one identified by the algorithm produces a much different profile for the central region.

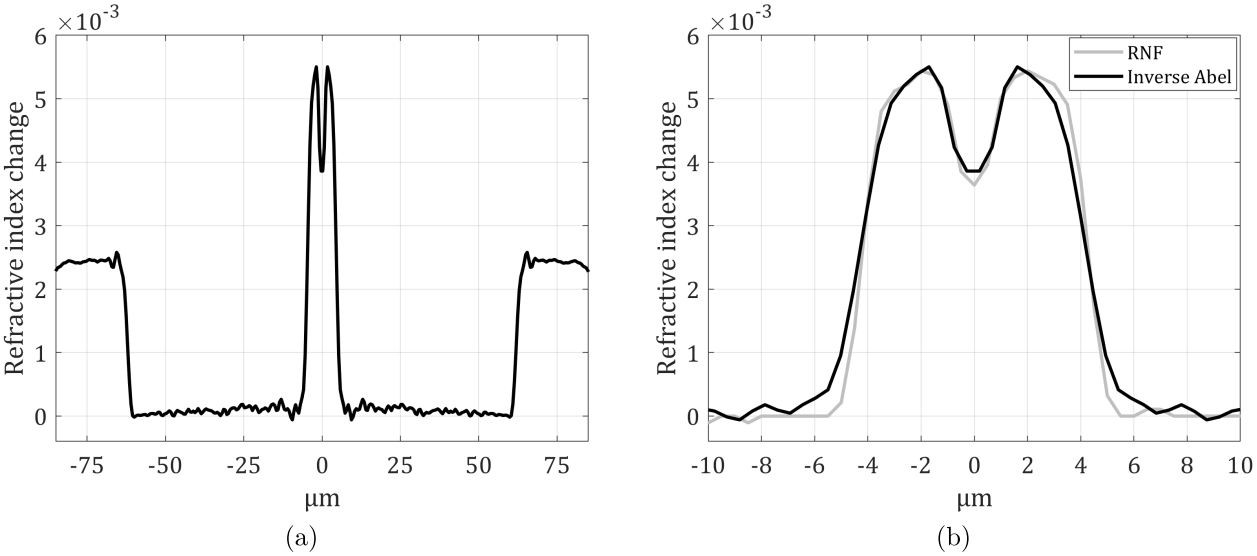

Figure 3.5 (a) Refractive index profile of an SMF-28 optical fiber measured using the inverse Abel transform reconstruction technique. (b) Comparison to the RNF method on the core region.

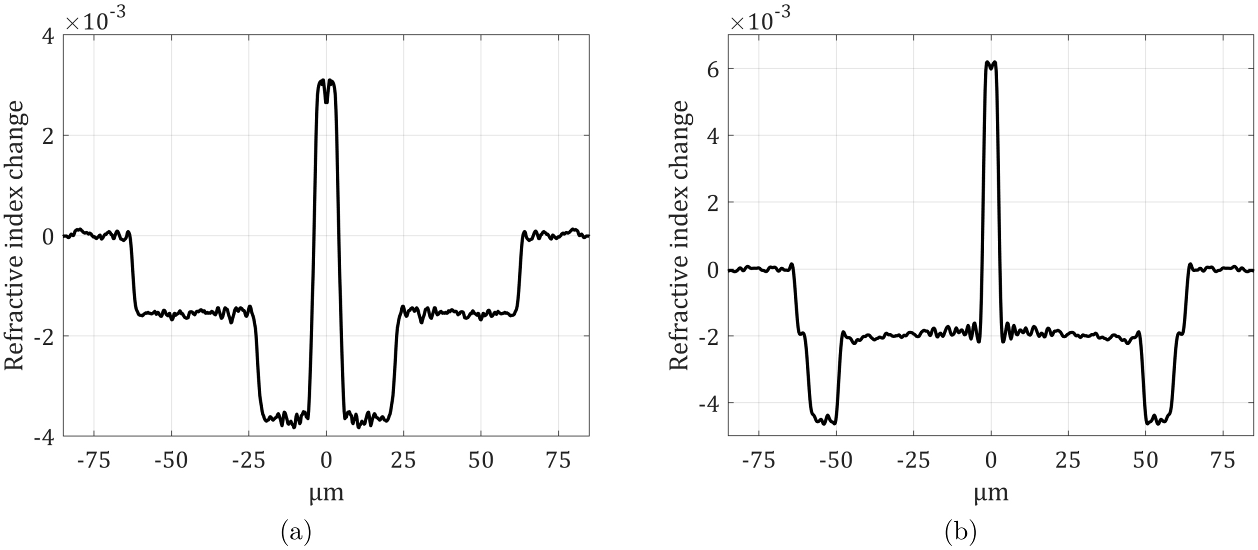

Figure 3.6 (a) Refractive index profile of a custom made double-clad optical fiber measured using the inverse Abel transform reconstruction technique. (b) Refractive index profile of a Fiberlogix double-clad optical fiber measured using the inverse Abel transform reconstruction technique.

3.2.3 Tomography (inverse Radon transform)

This section presents the results for the refractive index profiling of axially asymmetric optical fibers using tomography. Figure 3.7 shows the reconstructed refractive index profile of various fibers along with reflection microscopy of their end-face for comparison purposes. The measurement on the SMF-28 fiber results in a profile very similar to the inverse Abel transform method, albeit a bit noisier with noise level nearing $2 \cdot 10^{-4}$. This is mostly due to the imperfect alignement of the 200 projections forming the tomogram. Still, the tomographic measurement gives much more information such as core excentricity and core ellipticity, something the inverse Abel transform cannot do.

Figures 3.7(c)-(f) show that the method is unaffected by slightly more complex fiber structures. The fiber of Figure 3.7(e) featuring five hollow regions around the core is well resolved both spatially and in refractive index. Figures 3.7(g)-(l) show measurements nearing the limits of the system. Indeed, while the 36 hollow regions of 1.4 µm in diameter of figure 3.7(g) are spatially resolved (except for the much smaller hole on one corner), their measured refractive index does not fully match that of the liquid which is the same as the fiber's surrounding. Figure 3.7(j) also shows that measurements on a very complexe fiber structure (200-odd hollow regions) leads to artifacts in the fiber's surrounding.

The tomographic imagine system was also tested on its ability to characterize the refractive index profile of fibered couplers by measuring a 2x2 coupler and a 3x3 coupler. The results are shown in Figure 3.8. Due to complications in the setup not being optimized for such samples, the noise level is slightly higher at $3 \cdot 10^{-4}$. There is no doubt that it could be lower if one used a dedicated sample holder. Overall, the system shows promise in fast, nondestructive characterization of couplers prior to packaging.

The tomographic imaging method is very sensitive to the alignment of the multiple projections forming the tomogram and again to the identification of the sample's center on the tomogram. The current system uses a very simple automated projection alignment algorithm. Finer alignment by interpolation of the projections on a finer grid would surely reduce the noise level to that of the inverse Abel transform method ($1 \cdot 10^{-4}$) and get rid of artifacts such as those surrounding the cores of the couplers.

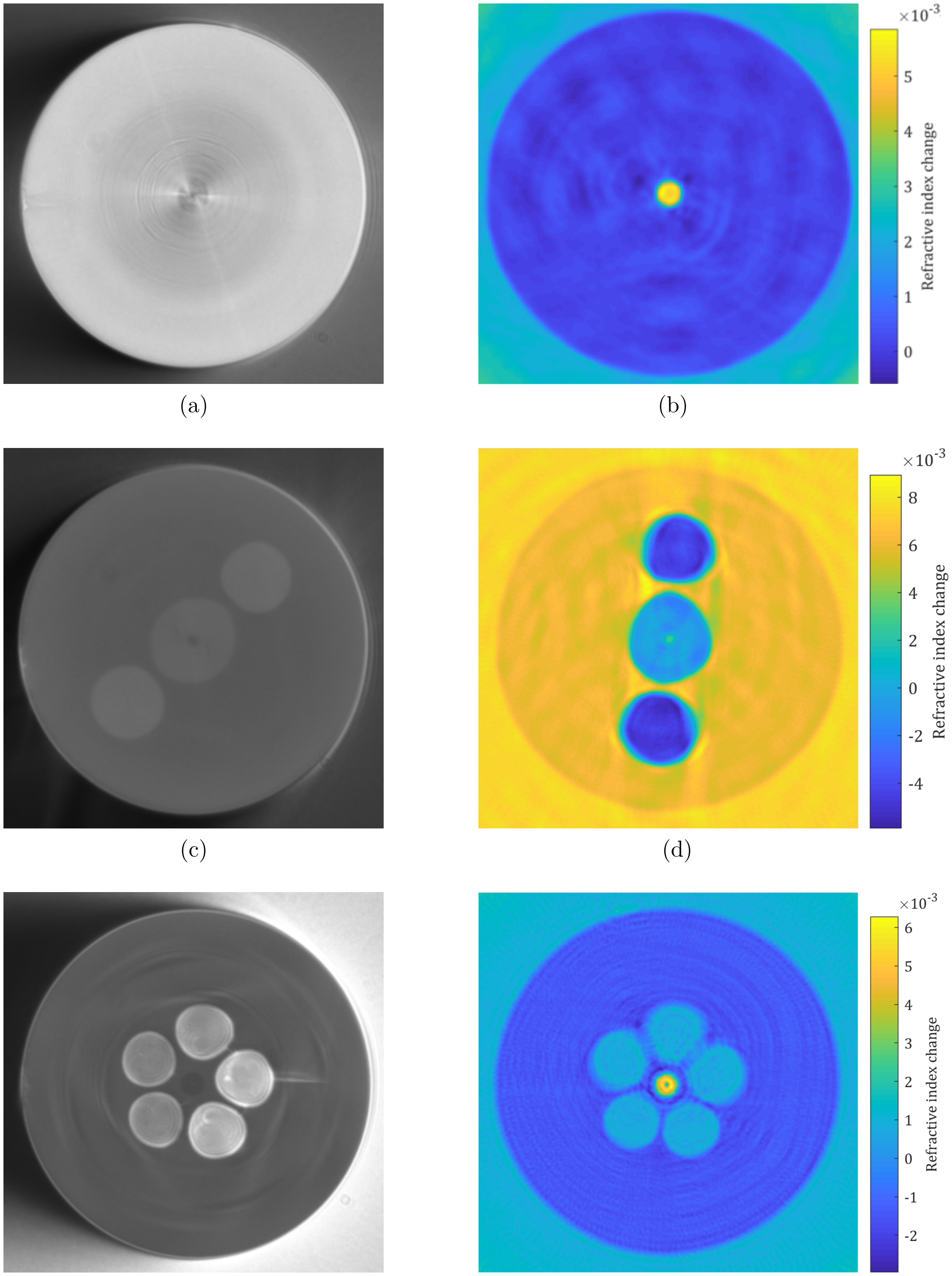

(a) (b)

(c) (d)

(e) (f)

Figure 3.7 (a) Reflection microscopy of an SMF-28 fiber and (b) its refractive index profile. (c) Reflection microscopy of a polarization maintaining PM5630 fiber and (d) its refractive index profile. (e) Reflection microscopy of a microstructured fiber with five hollow regions surrounding a solid core and (f) its refractive index profile.

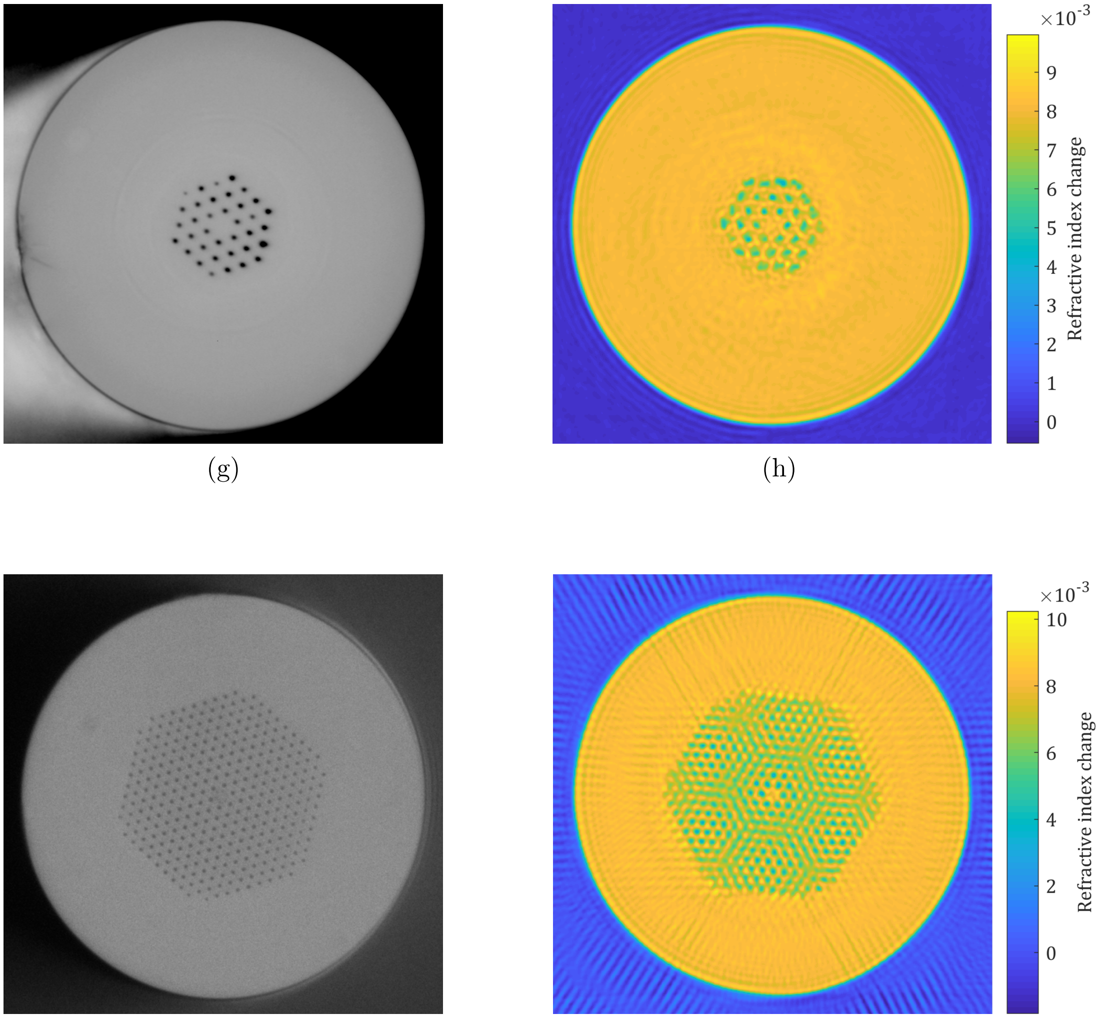

(g) (h)

(i) (j)

Figure 3.7 (cont.) (g) Reflection microscopy of a microstructured solid core fiber surrounded by 36 holes of 1.4 μm in diameter and (h) its refractive index profile. (i) Reflection microscopy of a microstructured solid core fiber surrounded by over 200 holes of 1.4 μm in diameter and (j) its refractive index profile.

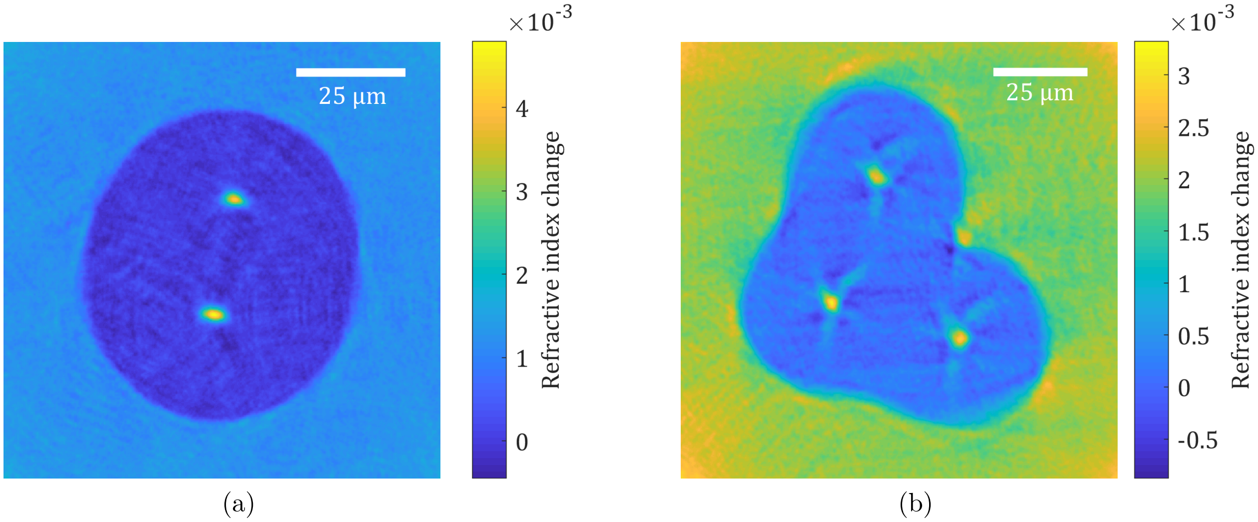

(a) (b)

Figure 3.8 (a) Refractive index profile of a 2x2 coupler. (b) Refractive index profile of a 3x3 coupler.

3.2.4 Refractive index profiling of laser written waveguides

The results regarding the use of the system for the measurement of laser written waveguides made the object of an article published in *Optics Express* in 2019. The novel method and the corresponding results and discussion are presented in Chapter 4.

Many measurements on laser written waveguides and gratings are also shown in Chapter 5, chapter dedicated to the subject of direct laser writing.

CHAPTER 4 ARTICLE 1: SPATIALLY RESOLVED CROSS-SECTIONAL REFRACTIVE INDEX PROFILE OF FS LASER WRITTEN WAVEGUIDES USING A GENETIC ALGORITHM

The novel method for the measurement of the refractive index profile of laser written waveguides made the object of an article published in *Optics Express* in 2019. The author's contribution constituted mainly in the development of the refractive index profile reconstruction algorithm, the experimentation, the data analysis and the redaction.

SPATIALLY RESOLVED CROSS-SECTIONAL REFRACTIVE INDEX PROFILE OF FS LASER WRITTEN WAVEGUIDES USING A GENETIC ALGORITHM

Antoine Drouin[1,*], Pierre Lorre[1], Jean-Sébastien Boisvert[1], Sébastien Loranger[1], Victor Lambin Iezzi[1] and Raman Kashyap[1,2]

[1] Dept. of Engineering Physics, Polytechnique Montreal, 2900 Edouard-Montpetit Blvd, Montreal, QC H3T 1J4, Canada

[2] Dept. of Electrical Engineering, Polytechnique Montreal, 2900 Edouard-Montpetit Blvd, Montreal, QC H3T 1J4, Canada

*Corresponding author: antoine.drouin@polymtl.ca

Laser written waveguides in glass have many potential applications as photonic devices. However, there is little knowledge of the actual profile of the usually asymmetric refractive index (RI) change across the fs laser written waveguides. We show, here, a new non-destructive method to measure any symmetric or asymmetric two-dimensional RI profile of fs laser written waveguides in transparent materials. The method is also suitable for the measurement of the RI profile of any other type of waveguide. A Mach-Zehnder interferometer is used to obtain the phase shift of light propagating transversely through the RI modified region. A genetic algorithm is then used to determine the matching cross-sectional RI profile based on the known waveguide shape and dimensions. A validation of the method with the comparison to a RNF measurement of the industry standard SMF-28 is presented as well as a demonstration of its versatility with measurements on femtosecond laser written waveguides.

4.1 Introduction

Laser written waveguide-based devices and sensors are being engineered for a growing number of applications. [1–7] To properly design such devices, knowledge of the refractive index change resulting from the laser interaction in glass is critical. The RI profile can be measured by techniques that have been developed for optical fibers but those are often inaccurate, unsuitable or unpractical for use with laser written waveguides. For instance, the commonly used RNF (refracted near-field) technique [19,20,30] is destructive since it requires the waveguide's face to be exposed by a cleave. Acquiring the RI profile of fibers or waveguides which are non-uniform along their propagation axis requires making multiple cleaves at different position, making the method time consuming and impractical. It is also known that cleaving the fiber can release mechanical stresses or induce defects such as cracks, effectively modifying the RI profile at the surface. [31] In the context of laser written waveguides where perfect perpendicular cleaves are very difficult to make, the surface must be polished. The polishing process induces mechanical stresses in the material, effectively altering a RNF measurement. Other RI profiling methods mainly demonstrated for optical fibers involve measuring the phase shift across the waveguide either by analyzing the fringe deformation on an interferogram produced by the sample [32–35], using the transport of intensity equation [36,37], using an N-step phase-shifting interferometry algorithm [38,39] or using deconvolution phase microscopy [40]. Optical fiber-based RI profiling techniques already described in the literature either suppose a very specific RI profile [32], an axial symmetry [35–37,39,41] or require the fiber to be rotated around its propagation axis to acquire many-angle tomographic images [33,34,38,40,42] to reconstruct the RI profile from the phase shift. However, laser written waveguides rarely possess axial symmetry, making the profile reconstruction very inaccurate at best. Turning the glass slab around the waveguide axis for tomographic analysis is either not possible or not practical for laser written waveguides. A widely used technique to estimate the RI change profile of a laser written waveguide is to measure its numerical aperture (NA) and use the following equation, derived from the case of a step-index fiber: $\mathrm{NA} = (n_{\mathrm{core}}^2 - n_{\mathrm{clad}}^2)^{1/2}$. [4] Although it gives an idea of a waveguide's ability to guide light, the use of this equation is in no way justified given the complex profile of laser written waveguides, not even remotely close to a step-index profile and lacking axial symmetry. Another technique is to measure the reflectivity of the sample's top surface where a waveguide has been inscribed. [27] A step-index profile is again assumed and the result is thus only an approximate value for the average RI, not a true two-dimensional RI profile. Others have tried to adapt the tomography technique to glass samples by rotating the beam around it. [28] Angles up to only 36° were achieved, after which the induced distortion in the image becomes significant. Given the lack of rotation angle and distortion, only the optical path length (OPL) for a given angle is obtained, from which the ellipticity of the waveguide is deduced by again assuming a step-index RI profile. A true two-dimensional RI profiling technique is described in [29]. DHM is done on the waveguide's end-face (light is sent along the waveguide) to measure the OPL difference, and thus the RI, at every point on the end-face. However, the main drawback of the technique is the necessity to use a very thin sample to keep the OPL difference below 2π, meaning that the method is destructive, assumes that the waveguide is constant along its propagation axis and requires a very lengthy sample preparation process.

We present here a new, straightforward, non-destructive method for RI profile measurements applicable to waveguides of arbitrary shapes. The method is divided into two steps. First, an interferogram of the sample is obtained from which it is possible to calculate the phase shift induced by the presence of the waveguide. Since angular tomography is not possible, information on the waveguide's shape and dimensions are required and can be obtained from reflection microscopy of the waveguide's end-facet. Although a cleaved and (at least roughly) polished end-facet is needed, the problems this brings to the RNF technique are not applicable here since the measurement is not done on the end-facet, but anywhere further along the waveguide. As a second step, using the shape and dimensions as well as the measured phase image, a genetic algorithm is used to reconstruct the RI profile that matches the measured phase shift with no restriction regarding axial symmetry.

The main limitation of our technique, which arises from the absence of tomography, is the indiscernibility of two identical features at different depths in the measurement. The individual contributions to the phase shift of two features cannot be separated if both have the same width in the direction perpendicular to the light beam. Given the very specific conditions necessary for this limitation to manifest itself, it is not an issue for the overwhelming majority of laser written waveguides.

4.2 Experimental method

4.2.1 Measurement method

The Mach-Zehnder interferometer (MZI) setup used for the phase measurement is shown in Figure 4.1(a). A HeNe laser at a wavelength of 632.8 nm is launched into an SMF-28 optical fiber. The light is split into the two arms of the interferometer using a 50:50 fiber coupler (C' in Figure 4.1(a)). One arm features a piezoelectric actuator (A) to stretch the fiber and induce a phase delay. Each arm includes a fiber collimator (C1,2), a half-wave plate (HW1,2) and a polarizer (P1,2). Polarizers and wave plates are adjusted to maximize interference fringes visibility. The sample (S) is placed just before the objective with the beam of the interferometer passing through the sample transversally (i.e. the waveguide's propagation axis is orthogonal to the beam). The reference arm features an identical objective to match the sample arm to produce a flat phase reference. The beams are recombined by a beam-splitter and an image (the interferogram) is formed on the CMOS camera using the final lens (L).

The focal plane of the objective in the sample arm (O1) is placed just under the waveguide sample so that the light going through it is collimated. Also, the focal plane is close to the waveguide to avoid any long-range deformation of the wavefront caused by the waveguide. Given the very small RI change of typical laser written waveguides ($\sim 10^{-3}$), the lens effect caused by the waveguide is negligible in near field. Test measurements have shown that the resulting phase image is independent of the exact focal plane position if the said plane is close enough to the waveguide (within ~10 µm).

As the light propagates through the waveguide perpendicularly, its phase is more or less shifted depending on the position relative to the waveguide (see Figure 4.2(b)):

$$\varphi\left(x,z\right)=\frac{2\pi}{\lambda}\int\Delta n\left(x,y,z\right)\mathrm{d}y. \tag{4.1}$$

In practice, $\varphi\left(x,z\right)$ is measured using the interferometric setup of Figure 4.1(a). The image seen on the camera is the intensity fringe pattern determined as the cosine of the phase of Equation 4.1 plus any reference phase variation due to misalignment and lens imperfections. To precisely measure the phase shift, the phase delay is scanned using the piezoelectric actuator and a video of fringe displacement is acquired. As the phase delay is increased, the intensity at each pixel of the camera follows a sine function (see Figure 4.3). A simple Fourier transform of the cosine function

$$\mathcal{F}\Big\{\cos\left(\omega_0 t-\varphi\right)\Big\}=\delta\left(\omega-\omega_0\right)e^{i\varphi} \tag{4.2}$$

allows the relative phase φ for each pixel to be calculated by taking the phase of the dominant frequency of the very narrow spectrum.

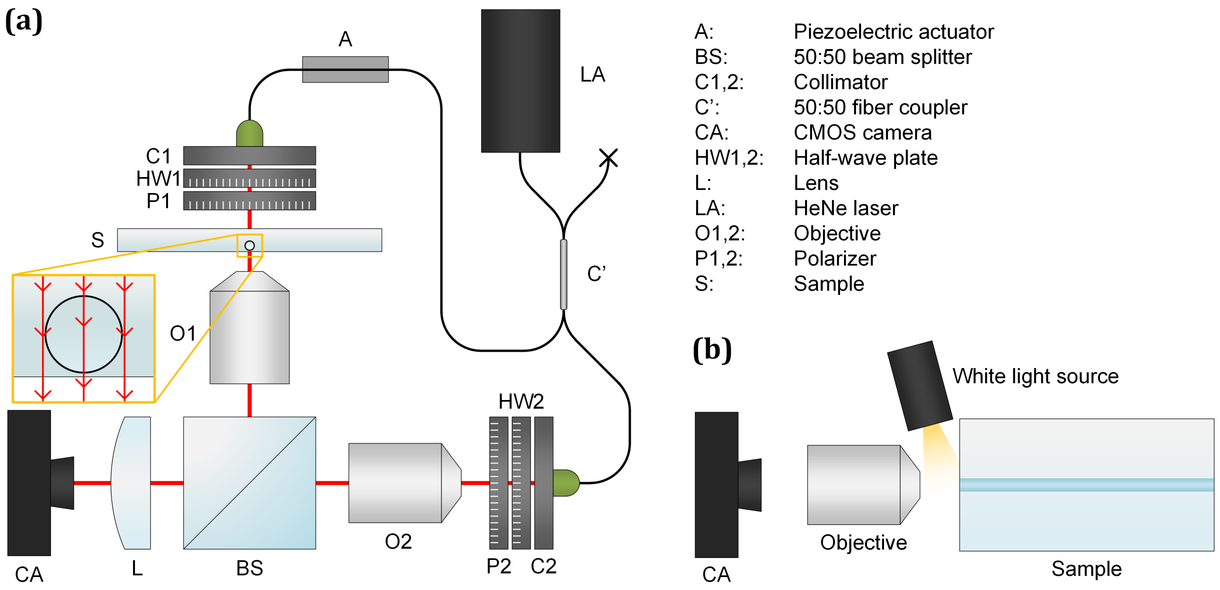

Figure 4.1 (a) Mach-Zehnder interferometer setup used to measure the phase shift produced by the waveguide. A piezoelectric actuator is used to induce a phase delay in one arm. The polarizers and wave plates are adjusted to maximize the fringe visibility. An image of the sample is formed at the camera by the objective and lens. (b) Setup used to obtain an image of the waveguide's cross-section. The polished end-facet of the sample is illuminated by a white light source coming from an angle.

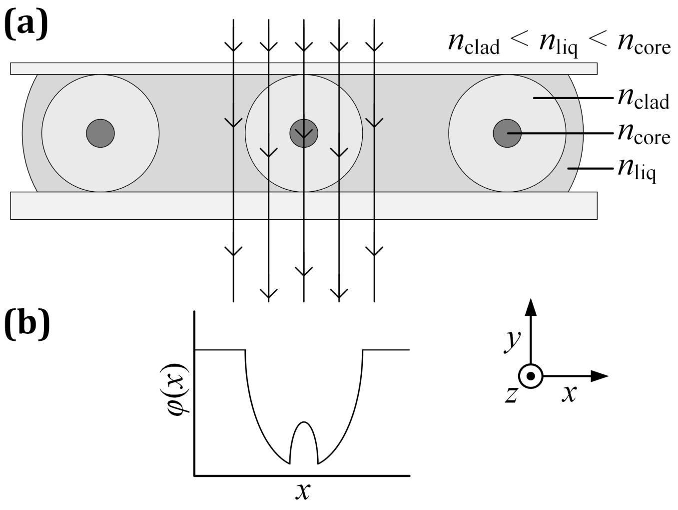

Figure 4.2 (a) Schematic cross-section of the sample used for the validation of the method and (b) the expected phase shift of light propagating downwards through the sample from the top. The fiber is immersed in index-matching liquid and placed between glass plates. Secondary fibers are used for support. The phase shifts more or less, depending on the optical path length for light at a given x position.

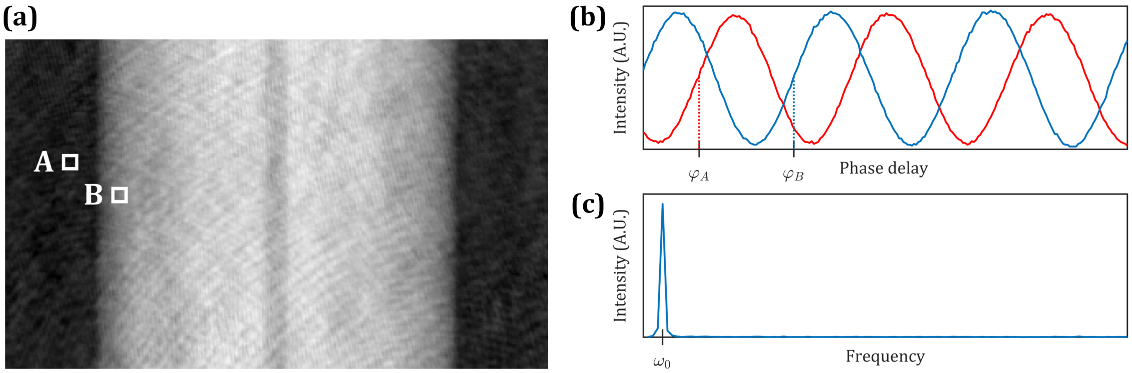

Figure 4.3 (a) Phase image after reconstruction for an SMF-28 fiber. (b) Measured light intensities at camera pixels A and B versus phase delay. (c) Result of the FFT at pixel A. The measured phase for the given pixel is the phase of the dominant frequency.

4.2.2 Genetic algorithm

To recover the RI information from the transverse phase image, a general knowledge of the waveguide's shape and dimensions is required. A cross-section image is thus acquired by simple camera inspection with angled illumination of the waveguide's end-facet, as shown in Figure 4.1(b). Such an image shows the relevant RI structures, but cannot resolve the actual value for the RI change profile. A genetic algorithm programmed in Matlab is used to find the RI distribution that matches the measured phase shift. The genetic algorithm takes as an input a two-dimensional model of the profile based on the cross-section microscopy as well as starting values and bounds for the parameters (see Equations 4.3 and 4.4 in the next section for a list of parameters). The model's various parameters dictating the different features' dimensions and RI change are then optimized by the algorithm as to minimize the difference between the phase shift produced by the modeled RI profile (calculated using Equation 4.1) and the one measured. The fitness function used in the genetic algorithm to compare the different solutions is simply the sum of squared differences.

The optimization process follows a standard method for genetic algorithms. First, random variations of the parameters of a random starting initial solution (within specified bounds) are generated (first generation "children" in the genetic analogy). The solutions with the best fitness scores as well as their parameters (or "DNA") are stored and will act as "parents" on which further variations are generated to form the subsequent generation.

The variation of the parameters is performed by two means: crossovers and random mutations. In the case of crossovers, children share some unchanged portion of each parent's DNA, thus preventing important genes from disappearing from the gene pool. Random mutations (small random variations of single parameters) are also used to improve diversity in the gene pool. The amplitude of these mutations is reduced progressively as newer generations stop showing improvements. The algorithm is stopped when all parameters have converged, with the solution thus not evolving anymore. Calculations are split on multiple CPU cores and high-end GPUs to allow for fast iterations, producing a solution (the two-dimensional RI profile) within seconds.

An example of the evolution of the DNA of the best solution of each generation when modeling the SMF-28 fiber's RI profile is shown in Figure 4.4 as well as its fitness score and its resulting RI profile (see next section for parameter descriptions and explanations). The parameters dictating the geometry of the fiber quickly converge because of their narrow bounds (given the information obtained from microscopy of the cross-section) and their importance on the resulting phase shift (and hence fitness score) whereas the RI levels need more time to converge to the correct value given their wider bounds.

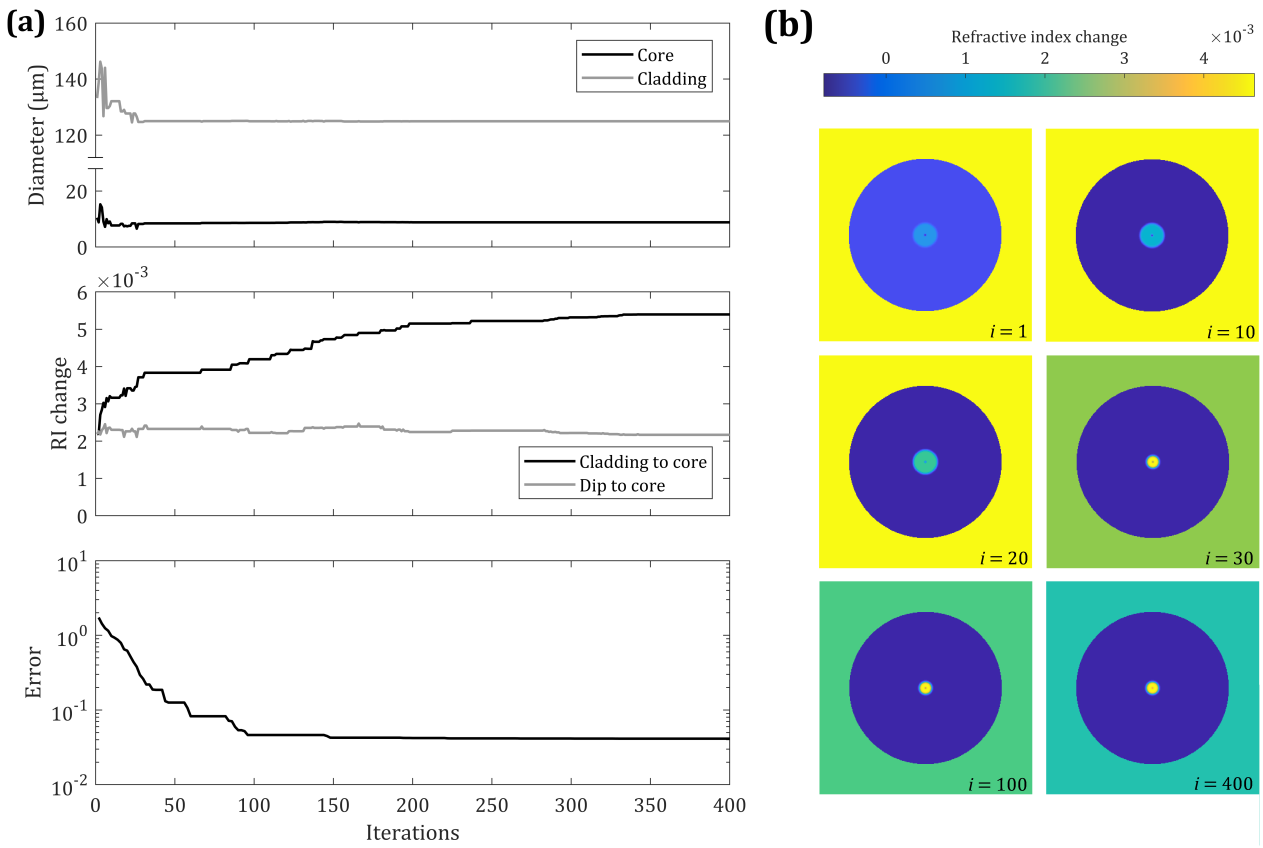

Figure 4.4 (a) Evolution of some of the parameters used to model the SMF-28 fiber using the genetic algorithm and the corresponding error. Parameters dictating the geometry converge very fast while fine-tuning of the RI levels takes more iterations. (b) Evolution of the RI profile calculated by the genetic algorithm.

4.3 Results

4.3.1 SMF-28 optical fiber

The method was validated by performing the measurement on an SMF-28 optical fiber, a waveguide for which the parameters are well known. Figure 4.2(a) shows a cross-section of the sample setup used for the validation of the method. The fiber is surrounded by an index-matching liquid and placed between a microscope slide and a cover slip. Other fibers are used as supports for the cover slip to ensure the entry surface is not tilted. The model based on the cross-section shown in Figure 4.5(a) and used to find the RI distribution is the following function of the fiber radius r:

$$\Delta n(r) = \frac{\Delta n_{\text{core}}}{2}\text{erfc}\left(\frac{r - r_{\text{core}}}{w_{\text{core}}}\right) + \Delta n_{\text{liq}}\text{H}(r - r_{\text{clad}}) + \Delta n_{\text{dip}}e^{-r^2/w_{\text{dip}}^2} \tag{4.3}$$

where H is the Heaviside function and Δn_i, r_i, and w_i are the parameters to optimize using the algorithm, namely, the RI differences of the core, cladding and central dip, the radii of the core and cladding, and the width of the transition from the core to the cladding and of the central dip, respectively. A complementary error function is used to model the core to cladding transition since the step-index nature of the SMF-28 fiber is unknown *a priori*, unlike the cladding-liquid interface, hence the Heaviside function for this region.

The reconstructed profile resulting from the genetic algorithm is shown in Figures 4.5(b) and 4.5(d). Figure 4.5(c) shows how closely the phase shift produced by the reconstructed profile matches the measurement. Given the RI of pure silica at 632.8 nm of 1.45702 [43], the RI change of $5.4 \cdot 10^{-3}$ at the core corresponds to 0.37 % which is close to the value of 0.36 % given by Corning. [44] The values for the core and clad diameters are also a very close match at 8.6 μm (full width at half maximum) and 124.6 μm versus the values of 8.2 μm and 125.0 ± 0.7 μm given by Corning. [44] To validate the method, the RI profile of the SMF-28 was also measured using the RNF method. The result is shown in Figure 4.5(d). Both measurements are in close agreement. The tests performed on the SMF-28 fiber let us confirm that the method is indeed valid and quite precise, at least for simple waveguides.

4.3.2 Weakly asymmetric waveguide

Let us now focus our attention on laser written waveguides. The first waveguide on which the method is demonstrated was written with a femtosecond laser (250 fs pulse length) operating at a wavelength of 515 nm, an average power of 200 mW, a repetition rate of 606 kHz, focused by an oil-immersion objective of 1.25 NA and by translating the sample at

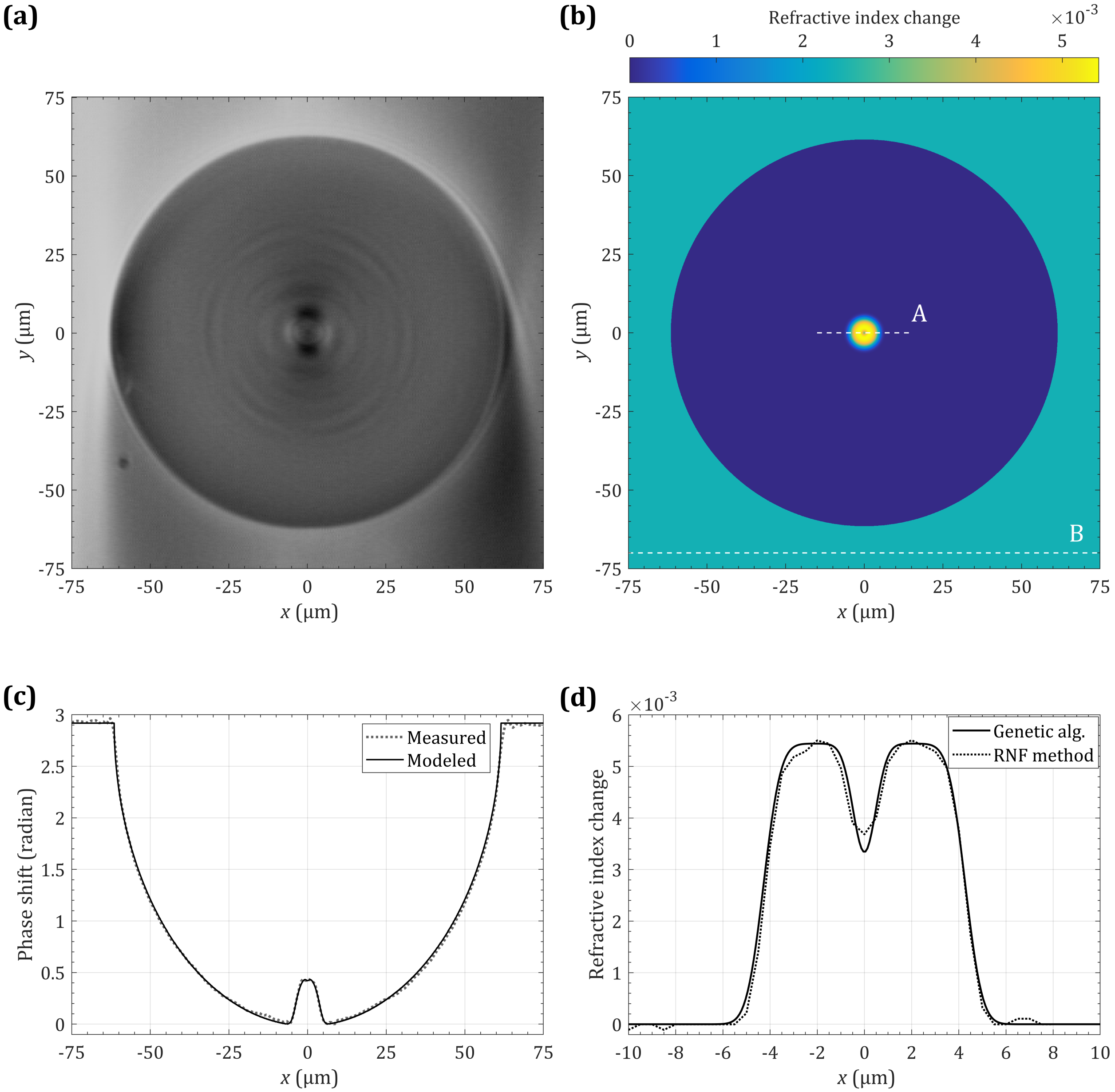

Figure 4.5 (a) Cross-section of the SMF-28 fiber obtained with the setup of Figure 4.1(b). (b) RI change profile reconstructed by the genetic algorithm for the SMF-28 fiber based on the measured phase shift and the known shape and dimensions from Figure 4.5(a). (c) Measured and modeled phase shifts along cross-section B of Figure 4.5(a). (d) Reconstructed RI change profile and result of the RNF measurement along cross-section A of Figure 4.5(b).

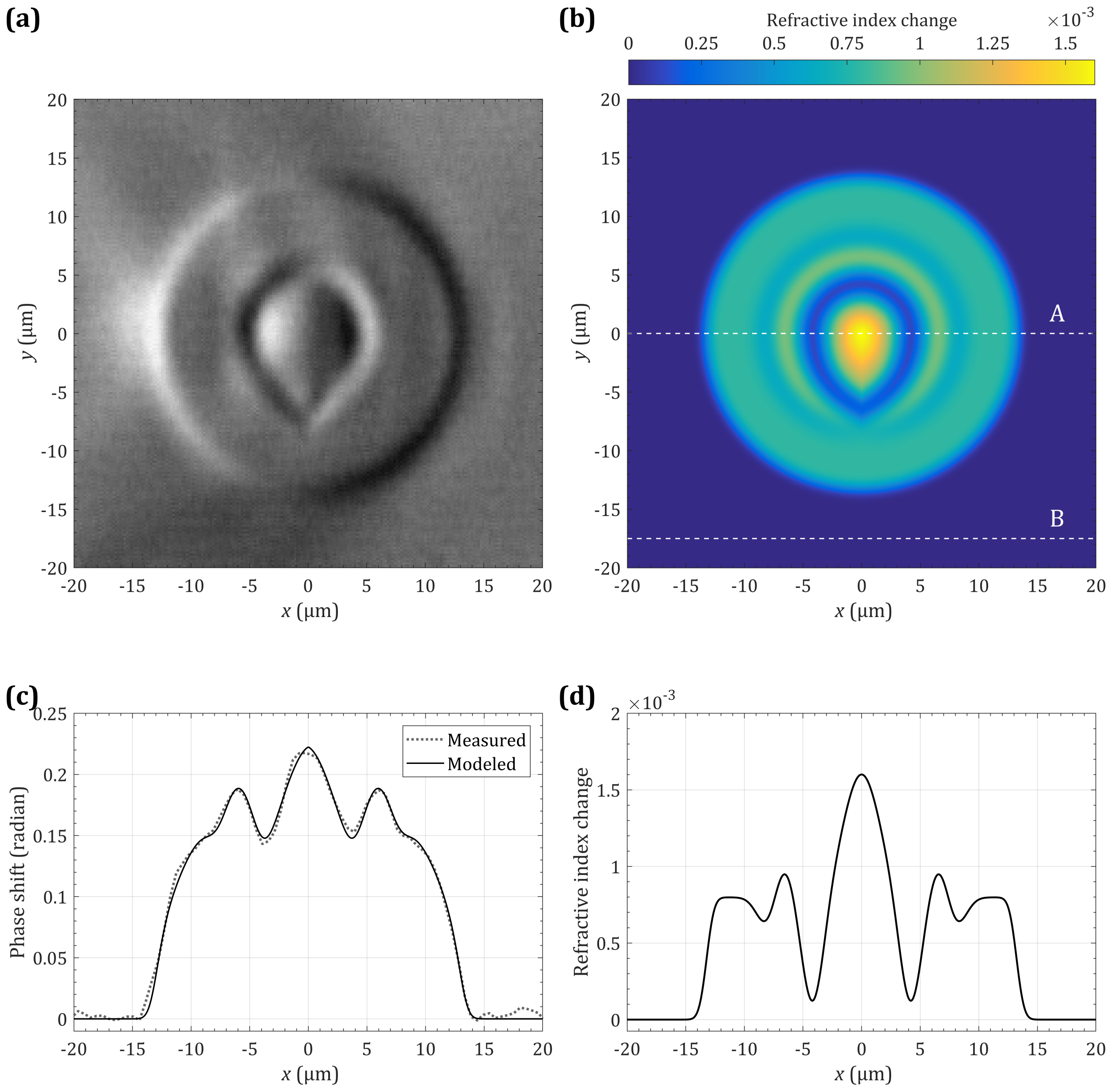

Figure 4.6 (a) Cross-section of the weakly asymmetric laser written waveguide obtained with the setup of Figure 4.1(b). (b) RI change profile reconstructed by the genetic algorithm for the weakly asymmetric laser written waveguide based on the measured phase image and the known shape and dimensions from Figure 4.6(a). (c) Measured and modeled phase shifts along cross-section B of Figure 4.6(b). (d) Reconstructed RI change along cross-section A of Figure 4.6(b).

a speed of 7 mm/s. The waveguide was written in Corning's Gorilla Glass 3 ($n = 1.5127$ at 532.8 nm [45]). Figure 4.6(a) shows a cross-section of the resulting waveguide. Although it is nearly circularly symmetric, not considering the loss of symmetry for $y < 0$ would yield other methods to produce an erroneous RI profile. The discrepancy would be even more obvious for most typical waveguides which show a stronger asymmetry.

The model of the waveguide used in the algorithm is, of course, fairly more complicated than for the case of the step-index fiber presented earlier. Given the asymmetry, the model is now a function of both the radius and the angle, as stated by Equation 4.4:

$$\Delta n(r, \theta) = \frac{\Delta n_{\text{out}}}{2} \text{erfc}\left(\frac{r - r_{\text{out}}}{w_{\text{out}}}\right) + \sum_{i=1}^{4} \Delta n_i e^{-(r - r_i(\theta))^2 / w_i^2(\theta)} \tag{4.4}$$

The complementary error function of amplitude Δn_{out} is again used to model the outer region while Gaussians of amplitude Δn_i and width w_i are added (or subtracted) at radial positions r_i to represent the structures observed by reflected light microscopy. Most radii and widths are now function of the angle θ to represent correctly the stretching along the y axis for some of the structures.

The results for the measurement on the laser written waveguide are shown in Figure 4.6. The measured and modeled phase shifts are again in very close agreement, as are the reconstructed RI profile and the cross-section microscopy.

4.3.3 Strongly asymmetric waveguide

The method is also demonstrated on a strongly asymmetric waveguide written in the same glass material. This waveguide (shown in Figure 4.7(a)) was written with the same femtosecond laser (250 fs pulse length, operating at a wavelength of 515 nm and a repetition rate of 606 kHz) but at a higher average power of 400 mW, focused by an objective of 0.65 NA and with a translation speed of only 0.5 mm/s, resulting in a much higher fluence. The outer region has an aspect ratio of about 1.25 while the region closer to center has an aspect ratio of $\sim$2.5 (in addition to being shaped closer to a droplet than an ellipse). Assuming axial symmetry would yield a RI profile nowhere near reality.

The waveguide's model used in the algorithm is very similar to the one used for the previous waveguide (see Equation 4.4). The only difference is that the parameter dictating the radius of the outer region r_{out} is now a function the angle ($r_{\text{out}}(\theta)$) since the outer region is not circularly symmetric anymore. The strong asymmetry is not a problem for this method as the results shown in Figure 4.7 indicate. The modeled phase shift is again a near perfect match to the measured phase shift.

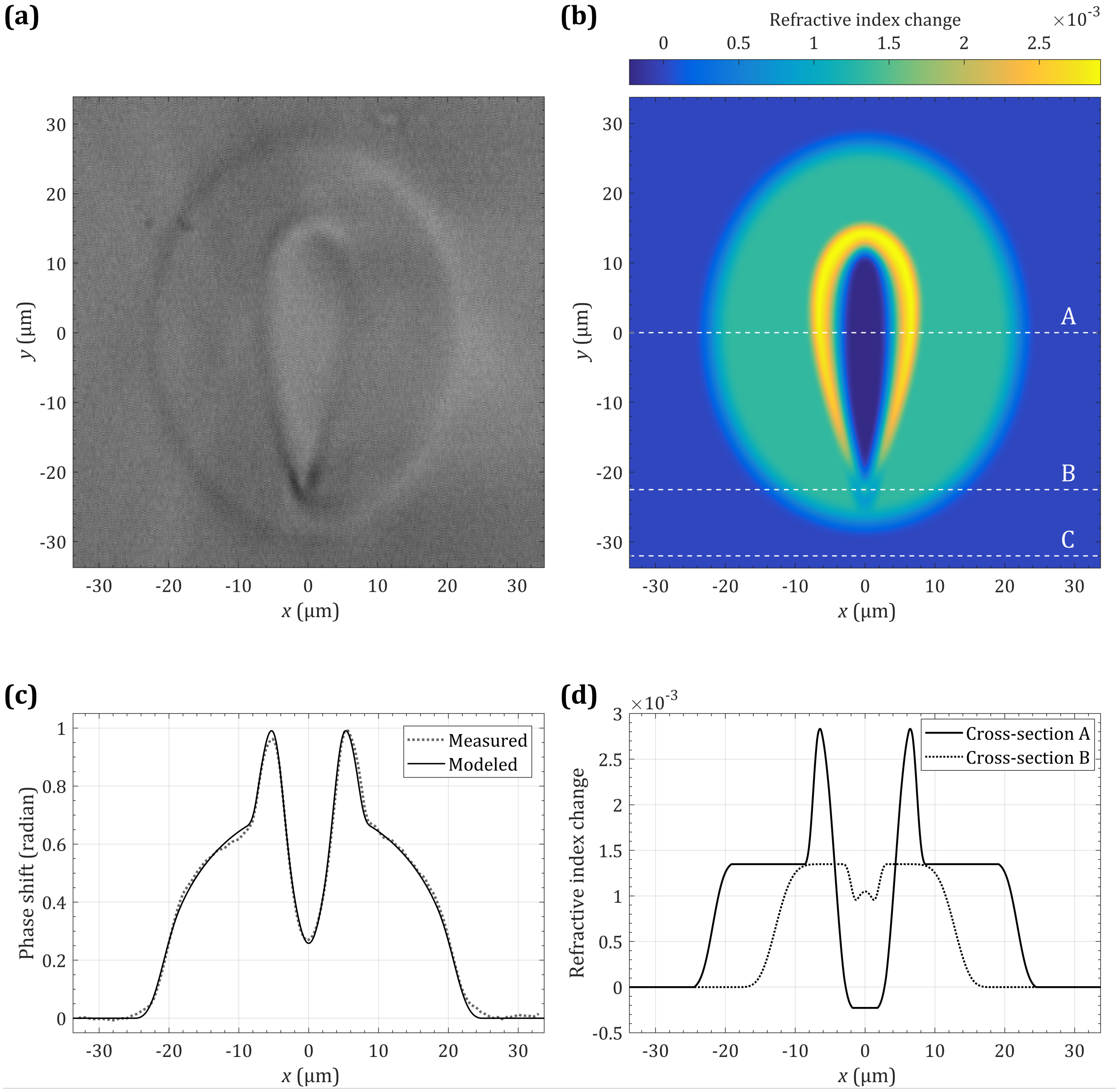

Figure 4.7 (a) Cross-section of the strongly asymmetric laser written waveguide obtained with the setup of Figure 4.1(b). (b) RI change profile reconstructed by the genetic algorithm for the strongly asymmetric laser written waveguide based on the measured phase image and the known shape and dimensions from Figure 4.7(a). (c) Measured and modeled phase shifts along cross-section C of Figure 4.7(b). (d) Reconstructed RI change along cross-sections A and B of Figure 4.7(b).

4.4 Discussion

The three tests presented show how well the method works for optical fibers and asymmetric waveguides. The limitations of the method are, however, not entirely clear from these tests. To evaluate the spatial resolution, a sample with resolution targets made of sharp ∼0.75 μm deep square grooves of various widths was fabricated by applying photoresist to a 1 mm thick glass slab followed by exposure with an e-beam before etching. Another sample with identical patterns was also made with a chromium coating allowing us to compare the phase measurement's spatial resolution to regular transmission microscopy (without the interference of the reference arm). Figure 8 shows the picture of the smallest 1 μm wide groove pattern for both transmission microscopy and the measured phase shift. It is clear from these pictures that the spatial resolution is slightly better than 1 μm (0.92 μm by the 10–90 criteria).

Typical phase measurements show a noise level of 0.01 radian. How this translates to noise in the RI profile reconstruction depends on the structure studied, more specifically its size and RI change, as stated by Equation 4.1. For a typical laser written waveguide with a diameter of about 30 μm, this phase noise corresponds to an uncertainty of $\pm 10^{-4}$ in the RI. Of course, for a waveguide with twice the diameter, the noise in the RI reconstruction is halved.

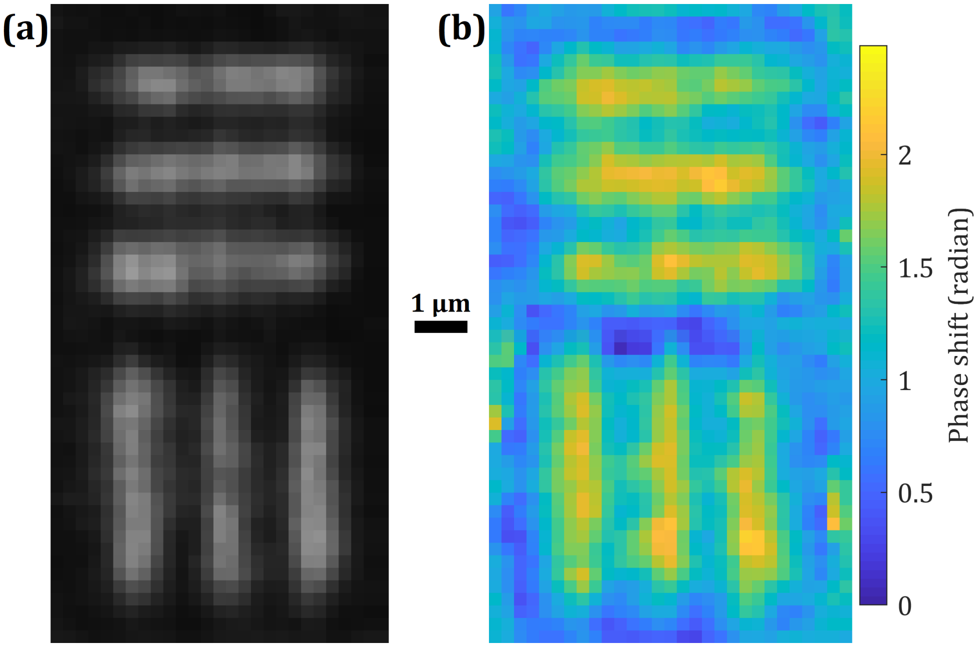

Figure 4.8 Resulting image of the 1 μm resolution target for (a) transmitted light amplitude without interference and (b) the calculated phase shift. The pattern is clearly resolved, indicating a sub-micron spatial resolution.

At a wavelength of 632.8 nm, the phase noise of 0.01 radian corresponds to an optical path difference of 1 nm. As such, for a feature to be distinguishable on the phase measurement, its optical path difference must be greater than this value. For example, the dip in RI at the center of the SMF-28 optical fiber can barely be observed on the phase measurement since its optical path difference is only of about 2.6 nm.

Due to the nature of the method, providing a value for the precision in the RI profile reconstruction proves to be rather difficult. Still, multiple solutions for the same waveguide were found using the algorithm and all agree within 10^{-4} refractive index units (RIU). Of course, this does not include errors in the modeling, which are negligible for waveguides of simple geometry such as those presented. Small differences in the geometry between the front-facet and location of measurement can be accounted by the genetic algorithm. However, if those differences are significant such that the model used cannot properly represent the evolving structure within its acceptance bounds, then this method is limited. Either the measurement should be repeated closer to the end-facet or the sample should be recut closer to the desired measurement position. Nonetheless, we believe that our technique compares favorably with the different measurement methods for RI profiling [21], in that it allows for measurement of waveguides within seconds with little preparation of the sample and with the added advantage of being able to measure asymmetric waveguides, unlike previously documented methods.

4.5 Conclusion

A new non-destructive interferometric method is presented to quickly measure the two-dimensional RI profile of laser written waveguides for which the shape is known. The phase shift of a cross-propagating wavefront is first measured. Then, the use of a genetic algorithm allows for the reconstruction of the RI profile of any arbitrarily asymmetric waveguide without the need for tomography, a first to our knowledge. The method was validated by comparison to RNF measurements on the SMF-28 optical fiber and demonstrated for asymmetric fs laser written waveguides. Its repeatability was shown to be within $\pm 10^{-4}$ RIU while its spatial resolution was shown to be sub-micron, making the method comparable to expensive commercially available optical fiber profilers based either on the RNF method or an interferometric method. This method's versatility and ease of use makes it an invaluable tool to better understand laser induced modification of transparent materials.

Funding

Natural Sciences and Engineering Research Council of Canada (NSERC).

Acknowledgment

We thank Nvidia for their donation of two Pascal Titan X GPUs used in the calculations. The authors also thank Mr. Jules Gauthier for the fabrication of the resolution targets as well as Mikaël Leduc and Simon Bolduc-Beaudoin for their help with the RNF measurements.

CHAPTER 5 DIRECT LASER WRITING

Direct laser writing has gathered interest over the last few years as a method to functionalize smartphone screens. The inscription of devices and sensors directly inside the screen has potential to replace conventional electronic components and thus allow for tighter packaging while keeping the screen transparent to the human eye.

The overwhelming majority of smartphone screens are made of toughened glass. These types of glasses show much different mechanical and chemical properties compared to more traditional glasses such as soda-lime. Due to the abundance of soda-lime glasses in a vast range of applications, research has focused most on laser modification of these glasses. As such, the material modification resulting from high powered laser exposition in toughened glass is not well documented.

An objective of the thesis is the study of laser writing in toughened glass and the use of the refractive index profiling system to optimize the writing parameters for producing waveguides, the basis for any integrated optics device. The results of a systematic study of the experimental parameters and their impact on material modification is first presented. A description of the waveguide writing parameters optimization follows. The chapter concludes on the use of direct laser writing for the making of another integrated optics component, the grating.

5.1 Laser writing parameters assessment

The material modification resulting from laser writing depends on a high number of parameters. This section presents a systematic study on the role of the most important parameters in laser writing. Some parameters were nonetheless kept constant over all test due to their lesser importance or to apparatus constraints. As such, the wavelength was kept at 515 nm for all tests; the repetition rate at 606 kHz (except for a dedicated section); the pulse length at 250 fs and the polarization linear and perpendicular to the writing direction. Furthermore, except for a section dedicated to direct laser writing of gatings, all tests presented were done in Corning's Gorilla Glass 3, a typical toughened glass for smartphone screens.

5.1.1 Translation speed

The speed at which the sample is translated is found to be the main parameter dictating the shape of the material modification. Figure 5.1 shows the resulting near-field of many waveguides obtained by white light illumination. At high translation speeds (> 50 mm/s) and thus low fluence, no guiding is possible since the refractive index change is too weak. For speeds of 4-32 mm/s, the material modification is ideal (given the other writing parameters) and an elliptical guiding region appears, although a central nonguiding region is present for lower speeds. At even lower translation speeds, the high fluence is such that the refractive index change goes back toward 0 and even slightly negative in that central region, making the material modification unsuitable for wave guiding applications.

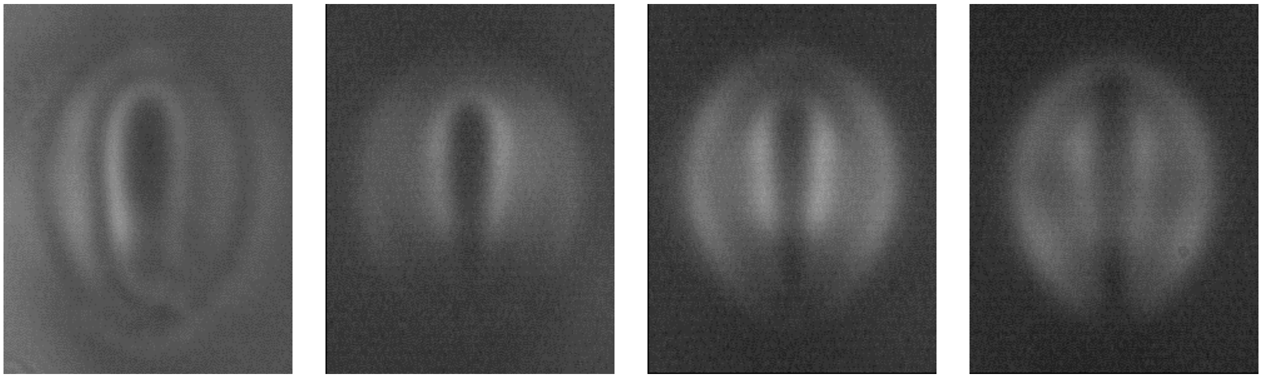

(a) 0.25 mm/s (b) 0.5 mm/s (c) 1 mm/s (d) 2 mm/s

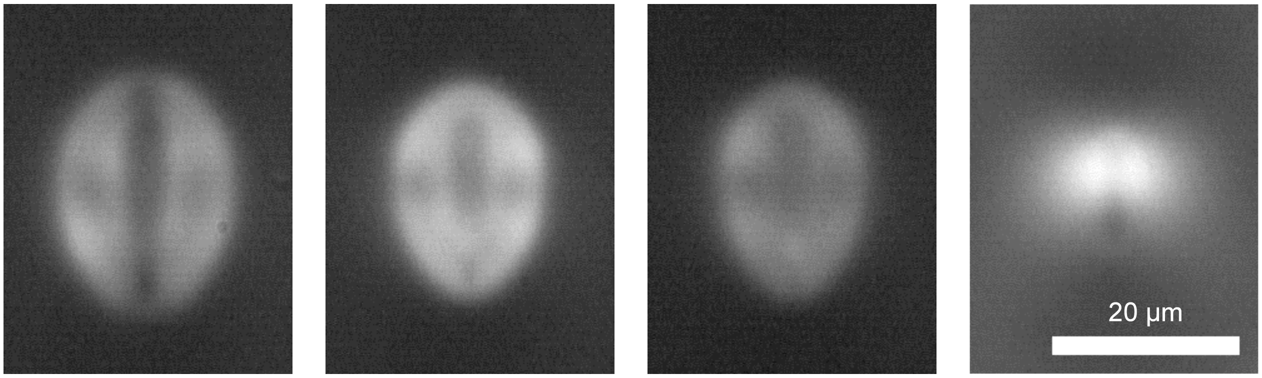

(e) 4 mm/s (f) 8 mm/s (g) 16 mm/s (h) 50 mm/s

Figure 5.1 Resulting material modification for various translation speeds of the sample at an average lasing power of 300 mW and using an objective with a NA of 0.65.

5.1.2 Power

While the translation speed has an effect on the shape of the material modification, the lasing power is found to mainly impact the size of the modified region. Figure 5.2 shows the end-face of waveguides written at different powers for both the low-speed and high-speed regime. As expected, there is a critical minimum power for which nonlinear absorption and thus material modification become significant. The material's behaviour at low power is a first indication that most material modification result from heat accumulation. Indeed, heat accumulates and then dissipates uniformly resulting in a more rounded shapes. At lower power, for example 150 mW as in Figure 5.2, where the pulse energy is too low for heat to accumulate between pulses, the material modification is limited to a thin line, most likely the shape of the focal spot when using an objective with a NA of 0.65 and considering the defocusing caused by the air-glass interface (see Chapter 1).

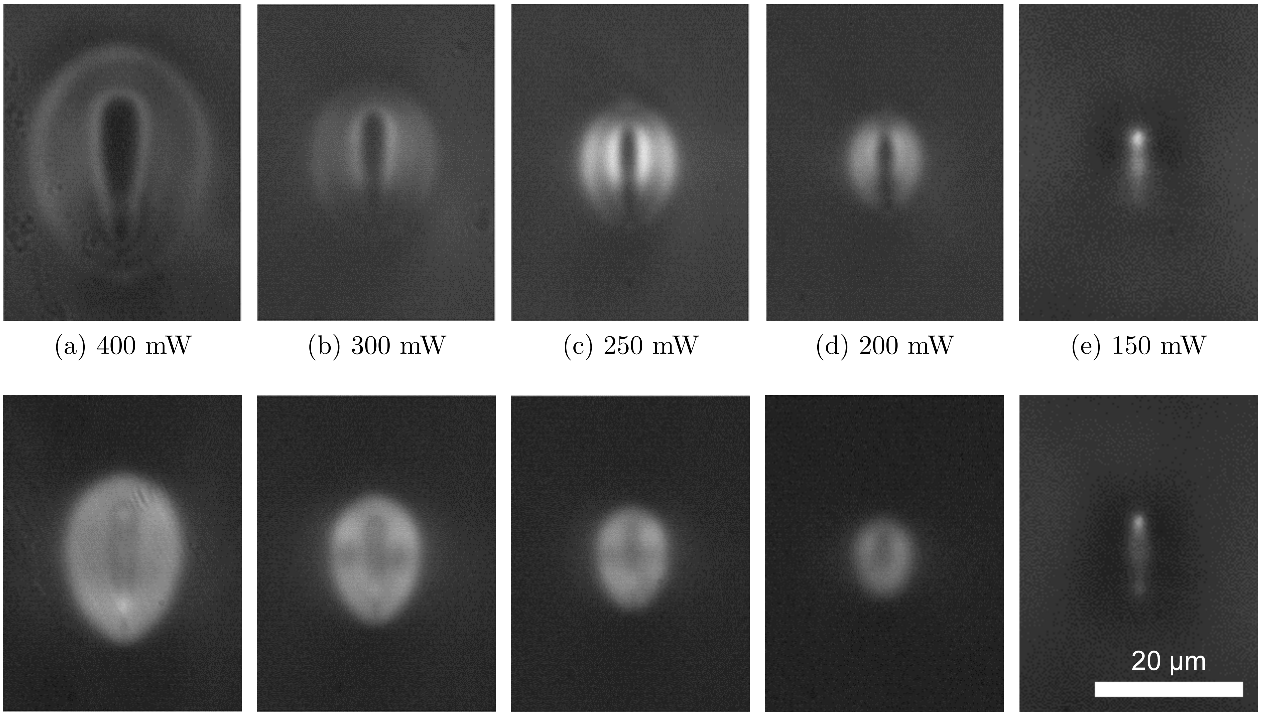

(a) 400 mW (b) 300 mW (c) 250 mW (d) 200 mW (e) 150 mW

(f) 400 mW (g) 300 mW (h) 250 mW (i) 200 mW (j) 150 mW

Figure 5.2 Resulting material modification for various average laser powers using a focusing objective with a NA of 0.65 and sample translation speeds of (a)-(e) 0.5 mm/s and (f)-(j) 10 mm/s.

5.1.3 Repetition rate

As previous tests on lasing power seemed to indicate that heat accumulation plays an important role in obtaining an interesting refractive index change profile, a test was devised to evaluate the impact of the temporal spacing between laser pulses. The laser's repetition rate was adjusted along with the sample's translation speed to change the spacing between pulses only. As illustrated in Figures 5.3(a) and (b), as the repetition rate is halved, the exposition time is doubled by halving the translation speed. The total deposited energy or fluence is identical both cases. Figure 5.3(c) and (d) qualitatively illustrate the possible effect of the pulses' temporal spacing on the temperature profile at a point in the material. If heat cannot dissipate completely between pulses, it accumulates. The 606 kHz repetition rate of the laser means the temporal spacing between pulses is of 1.65 µs, right around typical timescales for thermal diffusion and resolidication to occur. Figure 5.4 shows the resulting material modification for pulse spacings up to almost 10 µs, all with identical total fluence or deposited energy. As expected, the heat accumulation plays a central role in the obtained material modification. At larger pulse separation, the modified region is limited to a line. It is not sufficient to talk of fluence for a given set of parameter. The temporal profile of energy deposition is of importance. Although it was not possible to test due to equipment limitations, a repetition rate higher than 606 kHz could be useful in achieving heat accumulation at lower power and faster translation speed.

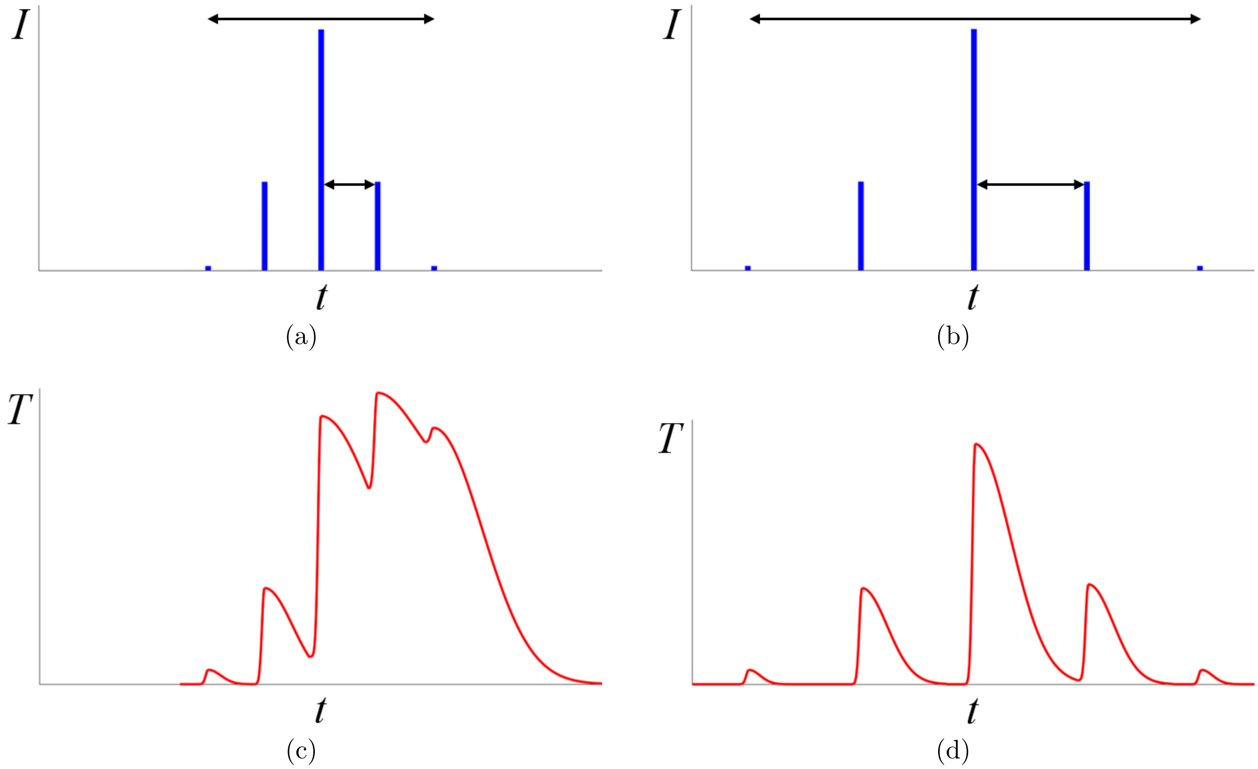

(a) (b)

(c) (d)

Figure 5.3 (a)-(b) The laser's repetition rate is adjusted along with the sample's translation speed to change only the temporal spacing between pulses. (c)-(d) Qualitative illustration of the effect of pulse spacing on the temperature profile of a point in the material and thus on the heat accumulation effect.

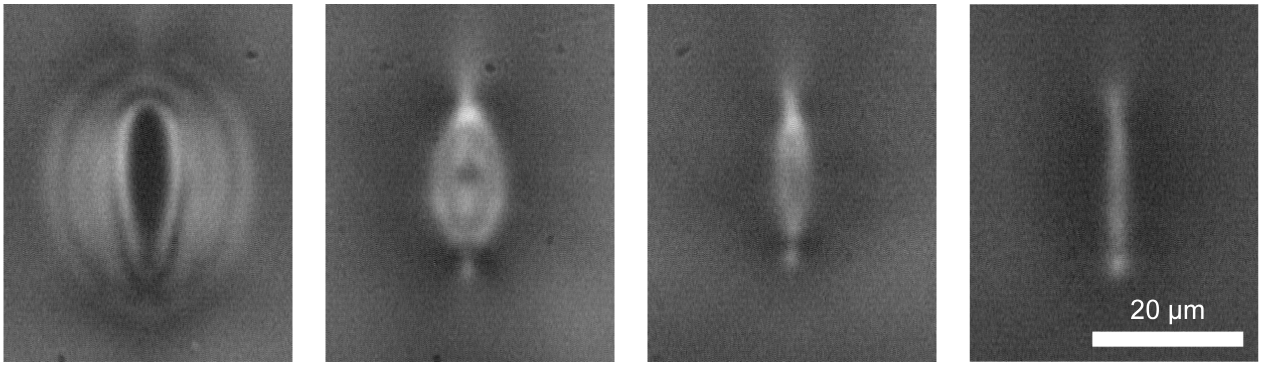

(a) 1.65 µs (b) 3.30 µs (c) 4.95 µs (d) 9.90 µs

Figure 5.4 Resulting material modification for different temporal pulse spacings. Pulse energy is identical in all cases (0.66 µJ). Total deposited energy is also identical in all cases.

5.1.4 Focusing objective

Previously described tests hint strongly at a much elongated focal spot, in part due to the naturaly elongated focal spot when using an objective with a NA of 0.65, but mostly due to the air-glass interface the beam must cross. Beam shaping methods can be used to change the shape of the focal spot. They usually rely on the use of cylindrical lenses, a slit or a spatial light modulator to produce an elliptical beam whose a focal spot is effectively stretched tranversly to the beam's propagation axis. [46–49] Such methods are thus incompatible with attempts at writing smaller waveguides. Objectives with a higher NA can be used to produce a tighter focal spot instead. However, the high numerical aperture accentuates the defocusing effect caused by the interface. Therefore, an objective with a NA of 1.25 made for use with immersion oil was trialed. The immersion oil removes the air-glass interface completely. The large droplet placed between the objective and the sample is dragged by the objective without further complication as the sample is translated at speeds up to 300 mm/s. Figure 5.5 shows the resulting material modification in both reflection and transmission microscopy for multiple sample translation speeds. The material modification is very similar to what was presented previously with the 0.65 NA objective but the overall shape is now much more circular. The material's reponse to exposition is also similar in that guiding occurs between an upper and lower bound for the translation speed. At low speed, the very high fluence does not result in a positive index change and thus in guiding whereas for high speeds, the exposition is too low for a considerable refractive index change to occur (see next section for quantitative study).

The much tighter focal spot resulting from the use of a high NA objective allows for writing at lower power. The waveguides of Figure 5.5 were produced using an average lasing power of only 200 mW (vs. 300 mW for those of Figure 5.1). The higher fluence (from a tighter focal spot) also allows for faster translation speeds of the sample as shown by the strong guiding of the sample written at 56 mm/s whereas such speeds resulted in no considerable refractive index change for the lower NA objective.

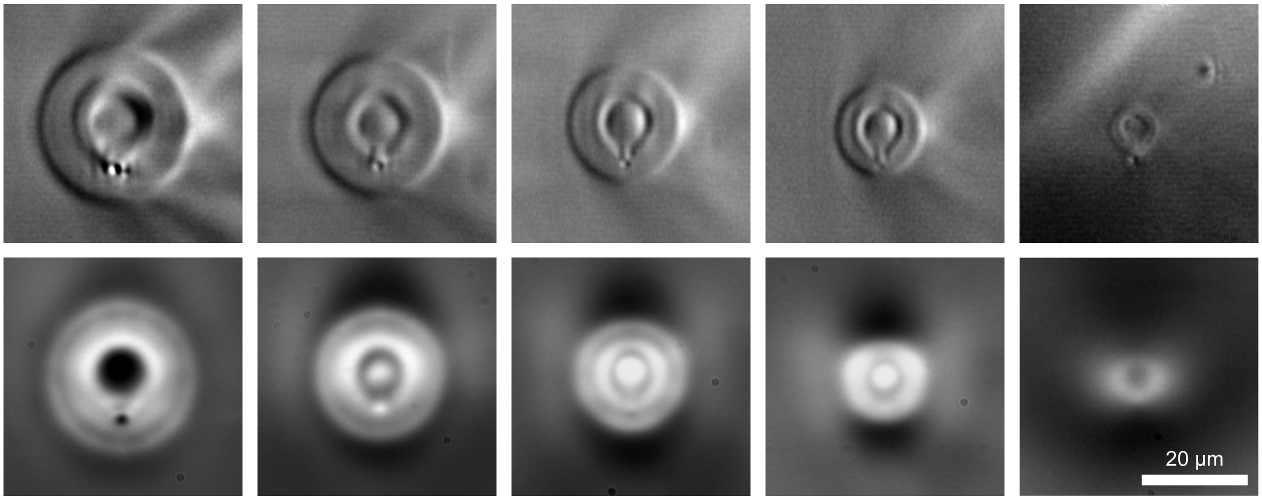

(f) 0.75 mm/s (g) 2.5 mm/s (h) 16 mm/s (i) 56 mm/s (j) 256 mm/s

Figure 5.5 Reflection microscopy (top) and near-field (bottom) of the waveguides written using an objective with a NA of 1.25 and an average power of 200 mW for various translation speeds.

5.2 Optimized waveguide

The refractive index measurement system was used to determine the ideal translation speed of the sample to produce a waveguide. Figure 5.6 shows the measured refractive index change of the waveguides of Figure 5.5 (and others) along a cross-section going through the center of the waveguides. As expected from the near-field images of the low-speed waveguides (Figure 5.5(a) and (b)), the refractive index change resulting from a low speed exposition (up to 1 mm/s) is negative at the center. At higher speeds, the central region is of increasing refractive index change while the surrounding ring is of decreasing refractive index, allowing the central region to behave as a waveguide. The optimal translation speed (for this set of parameters) is found to be 16 mm/s. For high speed exposition (> 16 mm/s), the surrounding ring's refractive index further reduces, but so does the central region and at a faster rate, producing weaker waveguides.

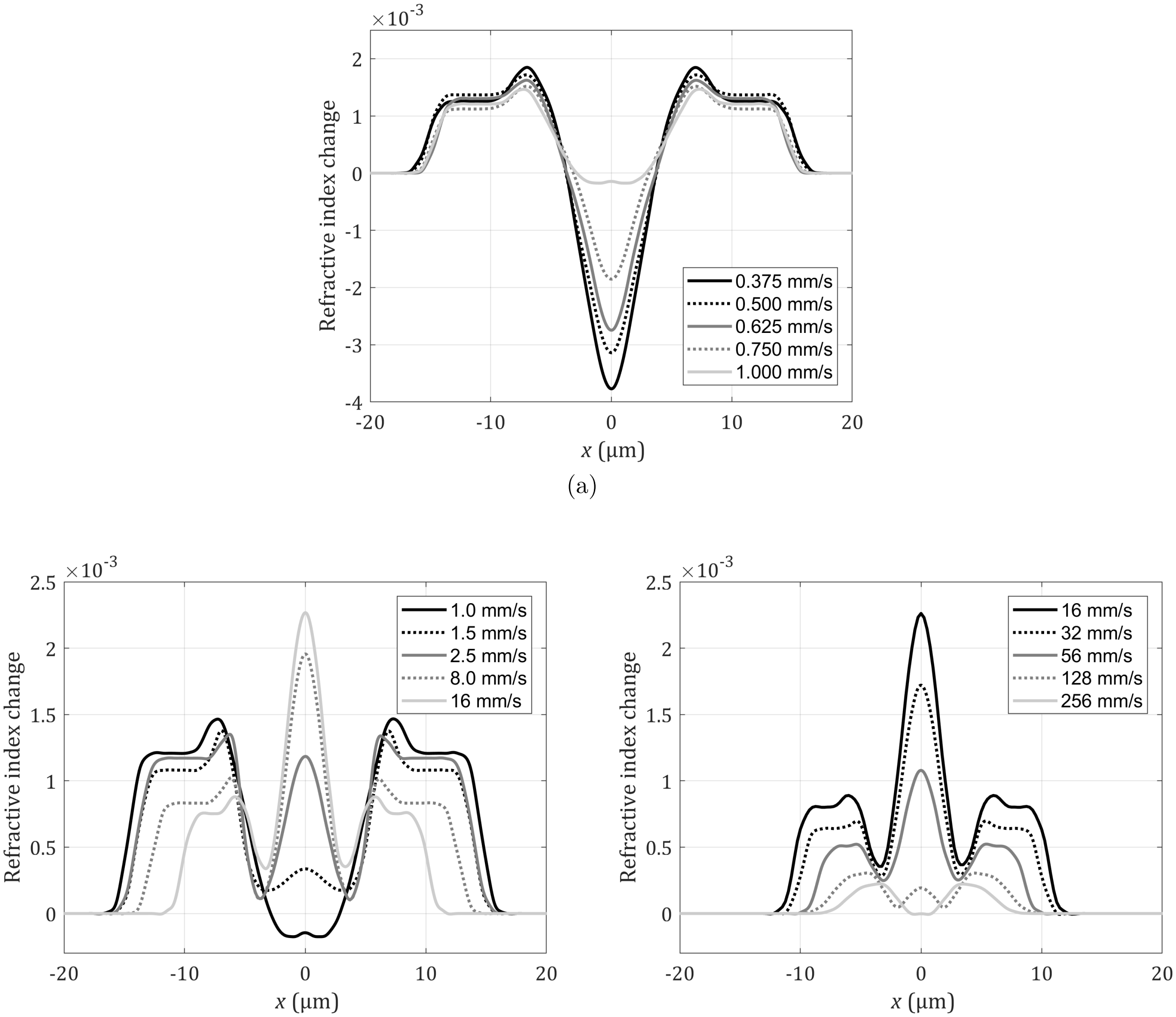

(a)

(b)

(c)

Figure 5.6 (a) Refractive index profile of waveguides produced by low speed exposition. (b) Transition from the low speed exposition regime to the optimal translation speed of 16 mm/s. (c) Transition from the optimal translation speed to the high speed exposition regime.

5.3 Gratings

Direct laser writing can also be used to fabricate gratings by inscribing many "waveguides" side by side. Although waveguides such as those presented thus far can be used as part of gratings (such as depicted in Figure 5.7(a)), their round shape is not optimal. For this reason, a completely different approach regarding experimental parameters was taken to produce linear regions of modified refractive index. The three parameters of crucial importance regarding the aspect ratio of the modified region were thus adjusted. First, an objective with a lower NA of 0.65 was used in conjunction with a glass of high refractive index ($n = 1.8$) to intensify the defocussing effect of the air-glass interface, producing a much stretched focal spot. In addition, a lower repetition rate of 202 kHz was used to reduce the heat accumulation effect. As heat dissipates isotropically, it usually contributes in creating circular regions of modified refractive index (see Chapter 2 and section 5.1.3). Other parameters are comparable to what was previously described (average power of 400 mW, pulse length of 250 fs, wavelength of 515 nm and writing speed of 15 mm/s). The resulting material modification

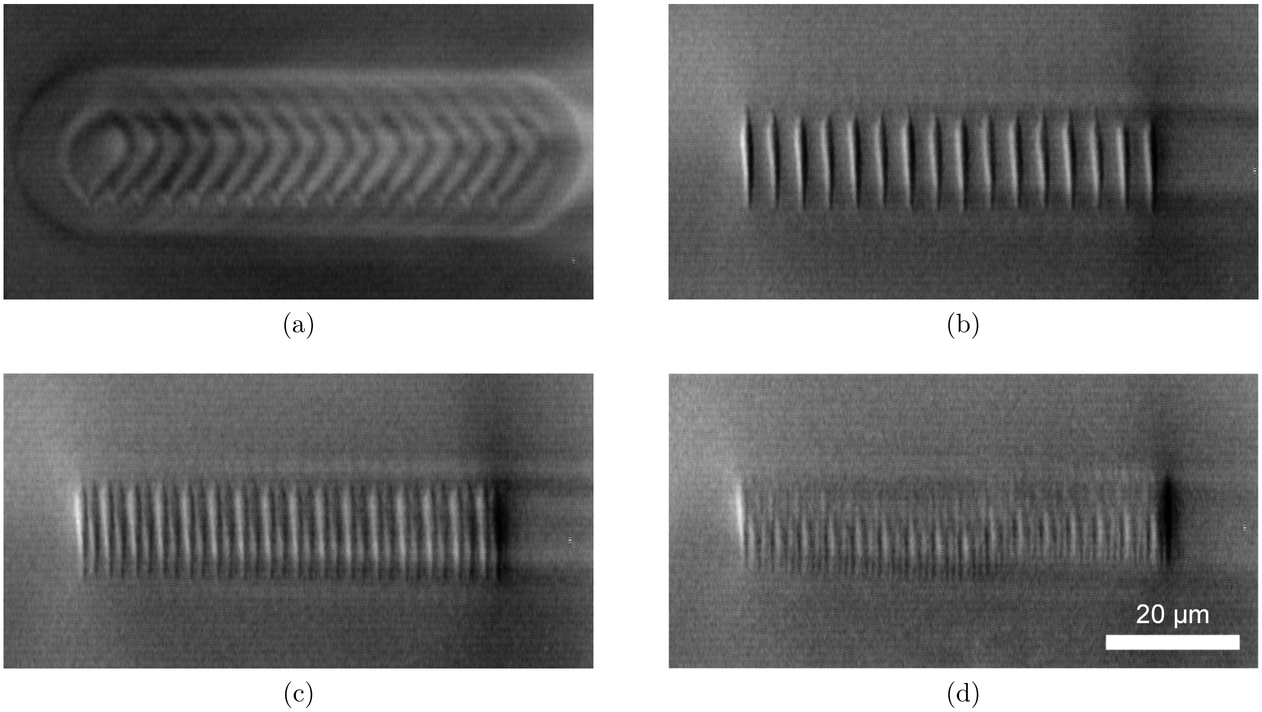

(a) (b)

(c) (d)

Figure 5.7 (a) 4 μm period grating written using standard parameters for waveguides. (b) 4 μm period grating written using parameters optimized for gratings. (c) 2 μm period grating. (d) 1 μm period grating.

is shown in Figure 5.7(b) as part of a grating with a period of 4 μm. Gratings with smaller periods of 2 and 1 μm are shown in Figure 5.7(c) and (d) respectively.

The refractive index measurement system was used to quantify the refractive index modulation in those gratings. For the 4 μm period grating, each track is completely separated from the next and is well resolved in phase imaging. The refractive index modulation reaches $3.2 \cdot 10^{-3}$ for this particular case (each track producing a $-3.2 \cdot 10^{-3}$ refractive index change). For the 2 μm period grating, there is a slight overlap between tracks, meaning the refractive index change does not go back to 0 between some tracks. This is indicated on the refractive index measurement shown in Figure 5.8 as the index modulation reaches $2.4 \cdot 10^{-3}$ in this case. For the 1 μm period grating, the overlap between tracks is considerable and the refractive index modulation is thus of only $0.8 \cdot 10^{-3}$.

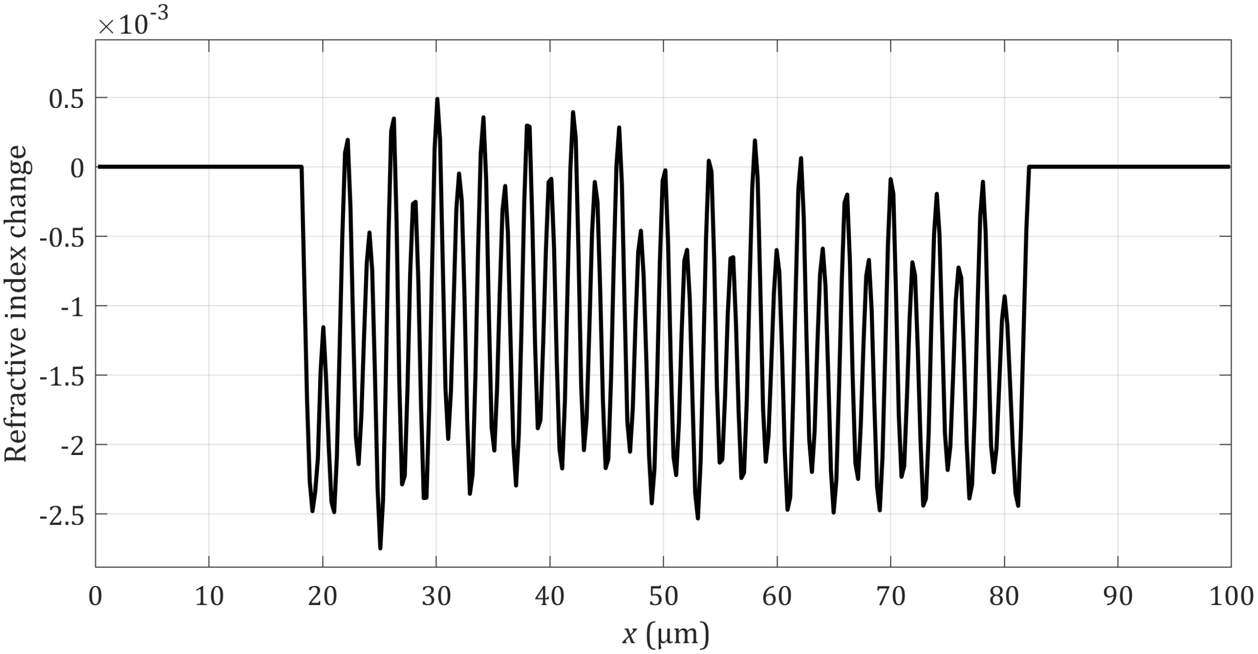

Figure 5.8 Refractive index change of the 2 μm period grating reconstructed using the genetic algorithm presented in Chapter 4.

CHAPTER 6 GENERAL DISCUSSION

In this thesis, a system for the measurement of the refractive profile of optical fibers and laser induced material modifications including waveguides and gratings was presented. A Mach-Zehnder interferometer along with phase shifting interferometry algorithms were used to obtain the phase image of light propagating transversely through the optical fiber or waveguide at a rate of up to over 100 frames per second with sub-micron resolution.

Different techniques to recover the refractive index profile from the measured phase shift were presented: the inverse Abel transform applicable to axially symmetric optical fibers and waveguides, tomographic imaging for axially asymmetric optical fibers and a novel genetic algorithm based reconstruction method for axially asymmetric waveguides written directly in glass. The precision of the reconstruction process was shown to be between $\pm 1 \cdot 10^{-4}$ and $\pm 3 \cdot 10^{-4}$ RIU depending on the method used and sample studied. The method was also shown to require very little sample preparation for measuring optical fibers and to not require any sample preparation in the case of laser written waveguides.

The subject of direct laser writing in Corning's Gorilla toughened glass was also covered in this thesis. A systematic study of the role of many experimental parameters in laser writing and the advancements in producing interesting waveguides resulting from the study were presented. Almost prefectly circular and polarization insensitive waveguides were produced in toughened glass. The refractive index profiling system was also shown to be useful in the optimization process of the most important parameter in laser writing, the writing speed.

Finally, the fabrication of gratings with periods as short as 1 μm and refractive index modulation as high as $3.2 \cdot 10^{-3}$ RIU was presented. The use of the refractive index profiling system to measure the refractive index modulation of the laser written gratings was also presented.

CHAPTER 7 CONCLUSION AND RECOMMANDATIONS

Despite the great results obtained from the use of the refractive index profiling system, some areas could be improved. First, the phase imaging resolution of 0.92 μm could be slightly improved by the use of objectives with higher magnification. Although not essential for the measurement of laser written waveguide and most optical fibers, a better resolution could allow for the measurement of microstructured fibers with sub-micron features and gratings of shorter periods than currently possible. This would however require the use of a camera with a sensor of a larger area.

The phase imaging could also be improved by the use of a light source of lower coherence to remove speckle and undesirable fringe patterns. Furthermore, although the use of a fibered interferometer is cost effective, a more traditional setup would be less sensitive and lead to an improvement in phase image quality. A lower noise in the phase image would allow for measurements of samples with less averaging along their propagation axis. This would in turn allow for the reconstruction of the 3D refractive index profile which could be useful in the case of couplers.

Finally, an important limit of the system resides in the recontruction of refractive index profiles using the genetic algorithm based optimization method. As stated in Chapter 4, it is hard to distinguish features at the same lateral position if they are of similar widths. To overcome this, it could be interesting to obtain the phase shift along a slightly different direction by a few degrees and thus be able to run the optimization process for two different projections, removing the uncertainty induced by the two problematic features.

REFERENCES

[1] M. Ams, G. Marshall, P. Dekker, J. Piper, and M. Withford, “Ultrafast laser written active devices,” *Laser & Photonics Reviews*, vol. 3, no. 6, pp. 535–544, 2009.

[2] T. T. Fernandez, S. M. Eaton, G. D. Valle, R. M. Vazquez, M. Irannejad, G. Jose, A. Jha, G. Cerullo, R. Osellame, and P. Laporta, “Femtosecond laser written optical waveguide amplifier in phospho-tellurite glass,” *Opt. Express*, vol. 18, no. 19, pp. 20 289–20 297, Sep 2010.

[3] V. Maselli, J. R. Grenier, S. Ho, and P. R. Herman, “Femtosecond laser written optofluidic sensor: Bragg grating waveguide evanescent probing of microfluidic channel,” *Opt. Express*, vol. 17, no. 14, pp. 11 719–11 729, Jul 2009.

[4] J. Lapointe, M. Gagné, M.-J. Li, and R. Kashyap, “Making smart phones smarter with photonics,” *Opt. Express*, vol. 22, no. 13, pp. 15 473–15 483, Jun 2014.

[5] K. K. Lee, A. Mariampillai, M. Haque, B. A. Standish, V. X. Yang, and P. R. Herman, “Temperature-compensated fiber-optic 3D shape sensor based on femtosecond laser direct-written Bragg grating waveguides,” *Opt. Express*, vol. 21, no. 20, pp. 24 076–24 086, Oct 2013.

[6] G. D. Marshall, A. Politi, J. C. F. Matthews, P. Dekker, M. Ams, M. J. Withford, and J. L. O’Brien, “Laser written waveguide photonic quantum circuits,” *Opt. Express*, vol. 17, no. 15, pp. 12 546–12 554, Jul 2009.

[7] M. R. Vázquez, V. Bharadwaj, B. Sotillo, S.-Z. A. Lo, R. Ramponi, N. I. Zheludev, G. Lanzani, S. M. Eaton, and C. Soci, “Optical NP problem solver on laser-written waveguide platform,” *Opt. Express*, vol. 26, no. 2, pp. 702–710, Jan 2018.

[8] J. Lapointe, F. Parent, E. S. de Lima Filho, S. Loranger, and R. Kashyap, “Toward the integration of optical sensors in smartphone screens using femtosecond laser writing,” *Opt. Lett.*, vol. 40, no. 23, pp. 5654–5657, Dec 2015.

[9] K. M. Davis, K. Miura, N. Sugimoto, and K. Hirao, “Writing waveguides in glass with a femtosecond laser,” *Opt. Lett.*, vol. 21, no. 21, pp. 1729–1731, Nov 1996.

[10] L. V. Kedlysh, “Concerning the theory of impact ionization in semiconductors,” *J. Exptl. Theoret. Phys.*, vol. 21, no. 6, pp. 1692–1707, Dec 1965.

[11] J. Schwider, R. Burow, K.-E. Elssner, J. Grzanna, R. Spolaczyk, and K. Merkel, “Digital wave-front measuring interferometry: some systematic error sources,” *Appl. Opt.*, vol. 22, no. 21, pp. 3421–3432, Nov 1983.

[12] J. Schmit and K. Creath, “Extended averaging technique for derivation of error-compensating algorithms in phase-shifting interferometry,” *Appl. Opt.*, vol. 34, no. 19, pp. 3610–3619, Jul 1995.

[13] G. Stoilov and T. Dragostinov, “Phase-stepping interferometry: Five-frame algorithm with an arbitrary step,” *Optics and Lasers in Engineering*, vol. 28, no. 1, pp. 61–69, 1997.

[14] M. R. Teague, “Deterministic phase retrieval: a green’s function solution,” *J. Opt. Soc. Am.*, vol. 73, no. 11, pp. 1434–1441, Nov 1983.

[15] T. E. Gureyev, A. Roberts, and K. A. Nugent, “Phase retrieval with the transport-of-intensity equation: matrix solution with use of Zernike polynomials,” *J. Opt. Soc. Am. A*, vol. 12, no. 9, pp. 1932–1941, Sep 1995.

[16] T. E. Gureyev and K. A. Nugent, “Phase retrieval with the transport-of-intensity equation. II. Orthogonal series solution for nonuniform illumination,” *J. Opt. Soc. Am. A*, vol. 13, no. 8, pp. 1670–1682, Aug 1996.

[17] C. Zuo, Q. Chen, and A. Asundi, “Boundary-artifact-free phase retrieval with the transport of intensity equation: fast solution with use of discrete cosine transform,” *Opt. Express*, vol. 22, no. 8, pp. 9220–9244, Apr 2014.

[18] W. J. Stewart, “A new technique for measuring the refractive index profiles of graded optical fibers,” *Technical Digest*, pp. 395–398, 1977.

[19] K. I. White, “Practical application of the refracted near-field technique for the measurement of optical fibre refractive index profiles,” *Optical and Quantum Electronics*, vol. 11, no. 2, pp. 185–196, Mar 1979.

[20] M. Young, “Optical fiber index profiles by the refracted-ray method (refracted near-field scanning),” *Appl. Opt.*, vol. 20, no. 19, pp. 3415–3422, Oct 1981.

[21] G. Pretzier, H. Jäger, T. Neger, H. Philipp, and J. Woisetschläger, “Comparison of different methods of abel inversion using computer simulated and experimental side-on data,” *Zeitschrift für Naturforschung A*, vol. 47, no. 9, pp. 955–970, Sep 1992.

[22] M. F. Kasim, J. Holloway, L. Ceurvorst, M. C. Levy, N. Ratan, J. Sadler, R. Bingham, P. N. Burrows, R. Trines, M. Wing, and P. Norreys, “Quantitative single shot and spatially resolved plasma wakefield diagnostics,” *Phys. Rev. ST Accel. Beams*, vol. 18, p. 081302, Aug 2015.

[23] H. Barrett and W. Swindell, “Analog reconstruction methods for transaxial tomography,” *Proceedings of the IEEE*, vol. 65, no. 1, pp. 89–107, 1 1977.

[24] M.-Y. Chiu, H. H. Barrett, and R. G. Simpson, “Three-dimensional reconstruction from planar projections,” *J. Opt. Soc. Am.*, vol. 70, no. 7, pp. 755–762, Jul 1980.

[25] K. M. Hanson and G. W. Wecksung, “Bayesian approach to limited-angle reconstruction in computed tomography,” *J. Opt. Soc. Am.*, vol. 73, no. 11, pp. 1501–1509, Nov 1983.

[26] A. Delaney and Y. Bresler, “Globally convergent edge-preserving regularized reconstruction: an application to limited-angle tomography,” *IEEE Transactions on Image Processing*, vol. 7, no. 2, pp. 204–221, Feb 1998.

[27] K. Minoshima, A. M. Kowalevicz, I. Hartl, E. P. Ippen, and J. G. Fujimoto, “Photonic device fabrication in glass by use of nonlinear materials processing with a femtosecond laser oscillator,” *Opt. Lett.*, vol. 26, no. 19, pp. 1516–1518, Oct 2001.

[28] A. Jesacher, P. S. Salter, and M. J. Booth, “Refractive index profiling of direct laser written waveguides: tomographic phase imaging,” *Opt. Mater. Express*, vol. 3, no. 9, pp. 1223–1232, Sep 2013.

[29] R. Osellame, N. Chiodo, V. Maselli, A. Yin, M. Zavelani-Rossi, G. Cerullo, P. Laporta, L. Aiello, S. D. Nicola, P. Ferraro, A. Finizio, and G. Pierattini, “Optical properties of waveguides written by a 26 MHz stretched cavity Ti:sapphire femtosecond oscillator,” *Opt. Express*, vol. 13, no. 2, pp. 612–620, Jan 2005.

[30] R. Göring, “Application of the refracted near-field technique to multimode planar and channel waveguides in glass,” *J. Opt. Commun.*, vol. 7, no. 3, pp. 82–85, Sep 1986.

[31] G. V. Steenberge, P. Geerinck, S. V. Put, J. Watté, H. Ottevaere, H. Thienpont, and P. V. Daele, “Laser cleaving of glass fibers and glass fiber arrays,” *J. Lightwave Technol.*, vol. 23, no. 2, p. 609, Feb 2005.

[32] M. J. Saunders and W. B. Gardner, “Nondestructive interferometric measurement of the delta and alpha of clad optical fibers,” *Appl. Opt.*, vol. 16, no. 9, pp. 2368–2371, Sep 1977.

[33] B. L. Bachim and T. K. Gaylord, "Microinterferometric optical phase tomography for measuring small, asymmetric refractive-index differences in the profiles of optical fibers and fiber devices," *Appl. Opt.*, vol. 44, no. 3, pp. 316–327, Jan 2005.

[34] B. L. Bachim, T. K. Gaylord, and S. C. Mettler, "Refractive-index profiling of azimuthally asymmetric optical fibers by microinterferometric optical phase tomography," *Opt. Lett.*, vol. 30, no. 10, pp. 1126–1128, May 2005.

[35] M. E. Marhic, P. S. Ho, and M. Epstein, "Nondestructive refractive-index profile measurements of clad optical fibers," *Applied Physics Letters*, vol. 26, no. 10, pp. 574–575, 1975.

[36] A. Roberts, E. Ampem-Lassen, A. Barty, K. A. Nugent, G. W. Baxter, N. M. Dragomir, and S. T. Huntington, "Refractive-index profiling of optical fibers with axial symmetry by use of quantitative phase microscopy," *Opt. Lett.*, vol. 27, no. 23, pp. 2061–2063, Dec 2002.

[37] E. Ampem-Lassen, S. T. Huntington, N. M. Dragomir, K. A. Nugent, and A. Roberts, "Refractive index profiling of axially symmetric optical fibers: a new technique," *Opt. Express*, vol. 13, no. 9, pp. 3277–3282, May 2005.

[38] W. Gorski and W. Osten, "Tomographic imaging of photonic crystal fibers," *Opt. Lett.*, vol. 32, no. 14, pp. 1977–1979, Jul 2007.

[39] Z. Liu, X. Dong, Q. Chen, C. Yin, Y. Xu, and Y. Zheng, "Nondestructive measurement of an optical fiber refractive-index profile by a transmitted-light differential interference contact microscope," *Appl. Opt.*, vol. 43, no. 7, pp. 1485–1492, Mar 2004.

[40] N. Dragomir, X. Goh, and A. Roberts, "Three-dimensional refractive index reconstruction with quantitative phase tomography," *Microscopy Research and Technique*, vol. 71, no. 1, pp. 5–10, 2008.

[41] E. Bélanger, J.-P. Bérubé, B. de Dorlodot, P. Marquet, and R. Vallée, "Comparative study of quantitative phase imaging techniques for refractometry of optical waveguides," *Opt. Express*, vol. 26, no. 13, pp. 17 498–17 510, Jun 2018.

[42] P. Kniazewski, T. Kozacki, and M. Kujawinska, "Inspection of axial stress and refractive index distribution in polarization-maintaining fiber with tomographic methods," *Optics and Lasers in Engineering*, vol. 47, no. 2, pp. 259–263, 2009, recent developments in Interferometry for Microsystems Metrology.

[43] I. H. Malitson, “Interspecimen comparison of the refractive index of fused silica,” *J. Opt. Soc. Am.*, vol. 55, no. 10, pp. 1205–1209, Oct 1965.

[44] Corning, “Corning single-mode optical fiber,” PI1036, 2002.

[45] Corning, “Corning Gorilla Glass 3 with NDR,” F 090315, 2015.

[46] R. Osellame, S. Taccheo, M. Marangoni, R. Ramponi, P. Laporta, D. Polli, S. D. Silvestri, and G. Cerullo, “Femtosecond writing of active optical waveguides with astigmatically shaped beams,” *J. Opt. Soc. Am. B*, vol. 20, no. 7, pp. 1559–1567, Jul 2003.

[47] M. Ams, G. D. Marshall, D. J. Spence, and M. J. Withford, “Slit beam shaping method for femtosecond laser direct-write fabrication of symmetric waveguides in bulk glasses,” *Opt. Express*, vol. 13, no. 15, pp. 5676–5681, Jul 2005.

[48] F. He, H. Xu, Y. Cheng, J. Ni, H. Xiong, Z. Xu, K. Sugioka, and K. Midorikawa, “Fabrication of microfluidic channels with a circular cross section using spatiotemporally focused femtosecond laser pulses,” *Opt. Lett.*, vol. 35, no. 7, pp. 1106–1108, Apr 2010.

[49] P. S. Salter, A. Jesacher, J. B. Spring, B. J. Metcalf, N. Thomas-Peter, R. D. Simmonds, N. K. Langford, I. A. Walmsley, and M. J. Booth, “Adaptive slit beam shaping for direct laser written waveguides,” *Opt. Lett.*, vol. 37, no. 4, pp. 470–472, Feb 2012.

APPENDIX A Graphical user interface of the refractive index profiling system

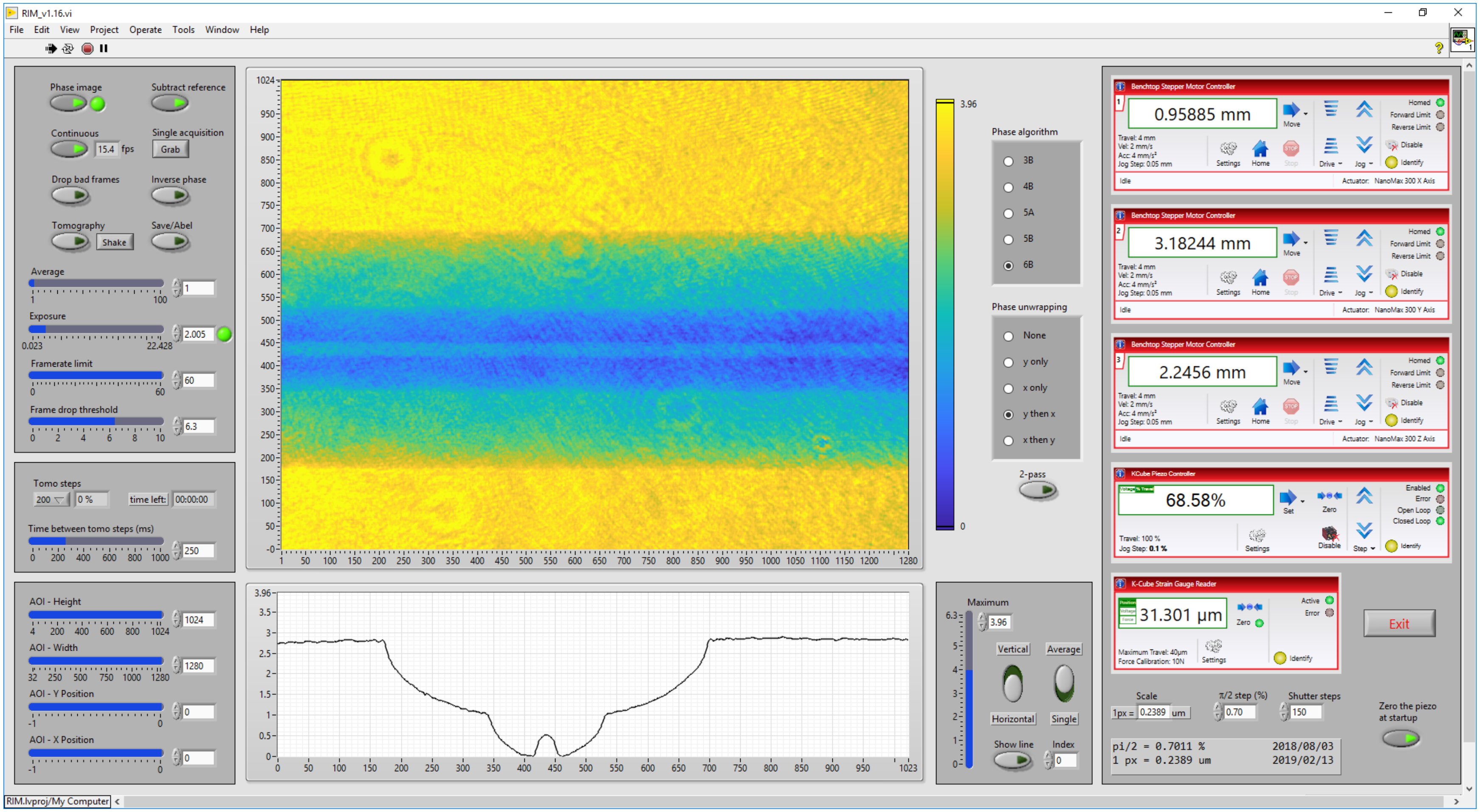

Continuous 15.4 fps

Average 1 (1–100)

Exposure 2.005 (0.023–22.428)

Framerate limit 60 (0–60)

Frame drop threshold 6.3 (0–10)

Tomo steps 200 0 % time left: 00:00:00

Time between tomo steps (ms) 250 (0–1000)

AOI - Height 1024 (4–1024)

AOI - Width 1280 (32–1280)

AOI - Y Position 0 (-1–0)

AOI - X Position 0 (-1–0)

Phase algorithm:
- ○ 3B
- ○ 4B
- ○ 5A
- ○ 5B
- ● 6B

Phase unwrapping:
- ○ None
- ○ y only
- ○ x only
- ● y then x
- ○ x then y

Maximum 3.96

Index 0

Benchtop Stepper Motor Controller 1: 0.95885 mm
Travel: 4 mm
Vel: 2 mm/s
Acc: 4 mm/s²
Jog Step: 0.05 mm
Idle
Actuator: NanoMax 300 X Axis

Benchtop Stepper Motor Controller 2: 3.18244 mm
Travel: 4 mm
Vel: 2 mm/s
Acc: 4 mm/s²
Jog Step: 0.05 mm
Idle
Actuator: NanoMax 300 Y Axis

Benchtop Stepper Motor Controller 3: 2.2456 mm
Travel: 4 mm
Vel: 2 mm/s
Acc: 4 mm/s²
Jog Step: 0.05 mm
Idle
Actuator: NanoMax 300 Z Axis

KCube Piezo Controller: 68.58%
Travel: 100 %
Jog Step: **0.1 %**

K-Cube Strain Gauge Reader: 31.301 µm
Maximum Travel: 40µm
Force Calibration: 10N

Scale 1px = 0.2389 um

π/2 step (%) 0.70

Shutter steps 150

```
pi/2 = 0.7011 %          2018/08/03
1 px = 0.2389 um         2019/02/13
```